

ดีไฮเดรชัน และ ออกซิเดทีฟดีไฮโดรจีเนชันของเอทานอล บนตัวเร่งปฏิกิริยาที่มีองค์ประกอบของ

เอสปีเอ 15 ที่เตรียมโดยวิธีโซลเจลและไฮโดรเทอร์มอล



บทคัดย่อและแฟ้มข้อมูลฉบับเต็มของวิทยานิพนธ์ตั้งแต่ปีการศึกษา 2554 ที่ให้บริการในคลังปัญญาจุฬาฯ (CUIR)
เป็นแฟ้มข้อมูลของนิสิตเจ้าของวิทยานิพนธ์ ที่ส่งผ่านทางบัณฑิตวิทยาลัย

The abstract and full text of theses from the academic year 2011 in Chulalongkorn University Intellectual Repository (CUIR)
are the thesis authors' files submitted through the University Graduate School.

วิทยานิพนธ์นี้เป็นส่วนหนึ่งของการศึกษาตามหลักสูตรปริญญาวิทยาศาสตรดุษฎีบัณฑิต

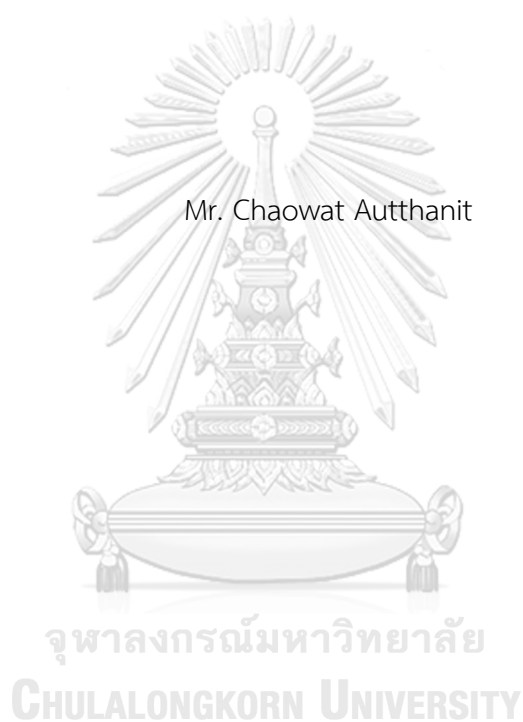
สาขาวิชาวิศวกรรมเคมี ภาควิชาวิศวกรรมเคมี

คณะวิศวกรรมศาสตร์ จุฬาลงกรณ์มหาวิทยาลัย

ปีการศึกษา 2560

ลิขสิทธิ์ของจุฬาลงกรณ์มหาวิทยาลัย

DEHYDRATION AND OXIDATIVE DEHYDROGENATION OF ETHANOL OVER
SBA-15 BASED CATALYSTS PREPARED BY SOL-GEL AND HYDROTHERMAL METHODS



A Dissertation Submitted in Partial Fulfillment of the Requirements
for the Degree of Doctor of Engineering Program in Chemical Engineering

Department of Chemical Engineering

Faculty of Engineering

Chulalongkorn University

Academic Year 2017

Copyright of Chulalongkorn University

Thesis Title	DEHYDRATION AND OXIDATIVE DEHYDROGENATION OF ETHANOL OVER SBA-15 BASED CATALYSTS PREPARED BY SOL-GEL AND HYDROTHERMAL METHODS
By	Mr. Chaowat Autthanit
Field of Study	Chemical Engineering
Thesis Advisor	Professor Bunjerd Jongsomjit, Ph.D.


Accepted by the Faculty of Engineering, Chulalongkorn University in Partial
Fulfillment of the Requirements for the Doctoral Degree

.....Dean of the Faculty of Engineering
(Associate Professor Supot Teachavorasinskun, Ph.D.)

THESIS COMMITTEE

.....Chairman
(Professor Muenduen Phisalaphong, Ph.D.)

.....Thesis Advisor
(Professor Bunjerd Jongsomjit, Ph.D.)

.....Examiner
(Chutimon Satirapathkut, D.Eng.)

.....Examiner
(Assistant Professor Suphot Phatanasri, D.Eng.)

.....External Examiner
(Sasiradee Jantasee, D.Eng.)

เชาวน์วัศ อรรถานินท์ : ดีไฮเดรชัน และ ออกซิเดทีฟดีไฮโดรจิเนชันของเอทานอล บนตัวเร่งปฏิกิริยาที่มีองค์ประกอบของเอสปีเอ 15 ที่เตรียมโดยวิธีโซลเจลและไฮโดรเทอร์มอล (DEHYDRATION AND OXIDATIVE DEHYDROGENATION OF ETHANOL OVER SBA-15 BASED CATALYSTS PREPARED BY SOL-GEL AND HYDROTHERMAL METHODS) อ.ที่ปรึกษาวิทยานิพนธ์หลัก: ศ. ดร. บรรเจิด จงสมจิตร, 151 หน้า.

งานวิจัยนี้มุ่งเน้นถึงการศึกษาคุณลักษณะและสมบัติการเร่งปฏิกิริยาของเซอร์โคเนียม (Zr) และโลหะผสมเซอร์โคเนียมและแลนทานัม (Zr-La) บนตัวรองรับชนิดเอสปีเอ 15 และตัวเร่งปฏิกิริยา วานเดียมออกไซด์บนตัวรองรับชนิดเอสปีเอ 15 ที่แตกต่างกัน ซึ่งจะถูกวิเคราะห์และมีความสัมพันธ์เกี่ยวข้องกัน โดยงานวิจัยนี้แบ่งการศึกษาออกเป็น 3 ส่วน เมื่อพิจารณาถึงการศึกษาในส่วนแรก เซอร์โคเนียม (Zr) และโลหะผสมเซอร์โคเนียมและแลนทานัม (Zr-La) บนตัวรองรับชนิดเอสปีเอ 15 ที่สังเคราะห์โดยวิธีโซลเจลและไฮโดรเทอร์มอลจะถูกเปรียบเทียบกัน ผลที่ได้พบว่าการเติม เซอร์โคเนียม (Zr) และโลหะผสมเซอร์โคเนียมและแลนทานัม (Zr-La) ส่งผลต่อสมบัติทางพื้นผิวของ เอสปีเอ 15 ที่เตรียมโดยทั้งสองวิธี ความเป็นกรดบนพื้นผิวบนเอสปีเอ 15 แสดงบริเวณตำแหน่งกัมมันต์ชนิดใหม่ โดยเฉพาะอย่างยิ่งชนิดของกรดบรอนสเตด งานวิจัยส่วนที่สองตัวเร่งปฏิกิริยาที่มี องค์ประกอบของเอสปีเอ 15 ทั้งหมดที่สังเคราะห์โดยทั้งสองวิธีถูกใช้เป็นการครั้งแรกสำหรับสำหรับ ปฏิกิริยาดีไฮเดรชันของเอทานอลไปเป็นเอทิลีน จากผลการทดลองพบว่าความสามารถในการเร่ง ปฏิกิริยาบนตัวรองรับชนิดเอสปีเอ 15 ในปฏิกิริยาดีไฮเดรชันของเอทานอลเกี่ยวข้องกับการ เปลี่ยนแปลงความเป็นกรดบนพื้นผิวที่เกิดจากการเติมเซอร์โคเนียม (Zr) และโลหะผสมเซอร์โคเนียม และแลนทานัม (Zr-La) งานวิจัยส่วนที่สามจึงได้นำตัวเร่งปฏิกิริยาเซอร์โคเนียม (Zr) และโลหะผสม เซอร์โคเนียมและแลนทานัม (Zr-La) บนตัวรองรับชนิดเอสปีเอ 15 นี้มาศึกษาต่อโดยปรับปรุงด้วย วานเดียมออกไซด์หรือวานเดียมสปีซีเพื่อใช้ในปฏิกิริยาดีไฮโดรจิเนชันและออกซิเดทีฟดีไฮโดรจิเนชันของเอทานอล เป็นที่น่าสังเกตว่าไอโซเลทมอนอเมอร์ริกวานเดียมสปีซี รวมถึงจำนวนของเบส อ่อนแสดงบทบาทสำคัญในปฏิกิริยาดีไฮโดรจิเนชันและออกซิเดทีฟดีไฮโดรจิเนชันของเอทานอลไป เป็นอะเซทิลดีไฮด์

ภาควิชา วิศวกรรมเคมี

ลายมือชื่อนิสิต

สาขาวิชา วิศวกรรมเคมี

ลายมือชื่อ อ.ที่ปรึกษาหลัก

ปีการศึกษา 2560

5771405221 : MAJOR CHEMICAL ENGINEERING

KEYWORDS: SBA-15 / SOL-GEL / HYDROTHERMAL / ETHYLENE / ACETALDEHYDE

CHAOWAT AUTTHANIT: DEHYDRATION AND OXIDATIVE DEHYDROGENATION OF ETHANOL OVER SBA-15 BASED CATALYSTS PREPARED BY SOL-GEL AND HYDROTHERMAL METHODS. ADVISOR: PROF. BUNJERD JONGSOMJIT, Ph.D., 151 pp.

In this present study, characteristics and catalytic properties of zirconium (Zr) and bimetal (Zr and La) containing in SBA-15 catalysts and different VO_x/SBA-15 catalysts were determined and well related. The study was divided into three parts. Regarding to the first part, zirconium (Zr) and bimetal (Zr and La) containing in SBA-15 synthesized by sol-gel and hydrothermal methods were compared. The results showed that the incorporation of Zr and bimetal (Zr and La) had an effect on the textural properties of both synthesized SBA-15 catalysts. Surface acidity in the SBA-15 suggests new active sites, especially Brønsted acid type. In the second part, all SBA-15 catalysts synthesized by both methods were first used as catalysts for the catalytic dehydration of ethanol to ethylene. The result shows that the performance of these SBA-15 supported catalysts in ethanol dehydration is also related with the alteration of surface acidity caused by the introduction of Zr and Zr-La. According to further modified of these catalysts, zirconium (Zr) and bimetal (Zr and La) containing in SBA-15 catalysts were selected to study in the third parts with vanadium oxide or VO_x species modification in order to be used in non-oxidative dehydrogenation and oxidative dehydrogenation of ethanol. It is worth noting that isolated monomeric VO_x species, as well as the amounts of weak basic sites essentially played important role in non-oxidative dehydrogenation and oxidative dehydrogenation of ethanol to acetaldehyde.

Department: Chemical Engineering Student's Signature

Field of Study: Chemical Engineering Advisor's Signature

Academic Year: 2017

ACKNOWLEDGEMENTS

Completion of this doctoral dissertation was possible with the support of several people. At the outset, I would like to express my sincere gratitude to my advisor Prof. Dr. Bunjerd Jongsomjit for the continuous support of my Ph.D study and related research, for his patience, motivation, and immense knowledge. As my supervisor, he has constantly forced me to remain focused on achieving my goal. His observations and comments helped me to establish the overall direction of the research and to move forward with investigation in depth. I could not have imagined having a better advisor and mentor for my Ph.D study.

Besides my advisor, I would like to thank the rest of my thesis committee: Prof. Dr. Muenduen Phisalaphong, as a chairman, Dr. Chutimon Satirapipathkul, Asst. Prof. Dr. Suphot Phatanasri and Dr. Sasiradee Jantasee as the members of the thesis committee for their valuable guidance and revision of my thesis.

I gratefully acknowledge the funding sources that made my Ph.D. work possible. I would like to thank the Grant for International Research Integration: Chula Research Scholar, Ratchadaphiseksomphot Endowment Fund and Grant for Research: Government Budget, Chulalongkorn University (2018) for providing scholarships to pursue doctoral studies.

Finally, I would like to thank my family for all their love and encouragement. For my father and mother who raised me with a love of science and supported me in all my pursuits. They are the most important people in my world and I dedicate this dissertation to them.

CONTENTS

	Page
THAI ABSTRACT	iv
ENGLISH ABSTRACT	v
ACKNOWLEDGEMENTS	vi
CONTENTS	vii
LIST OF TABLES	xii
LIST OF FIGURES	xiii
CHAPTER I INTRODUCTION.....	1
1.1 General introduction and rational	1
1.2 Research objectives	5
1.3 Research scopes	5
1.4 Research methodology	6
CHAPTER II.....	10
THEORY AND LITERATURE REVIEWS	10
2.1 Ethanol dehydration reaction.....	10
2.2 Ethanol dehydrogenation reaction.....	13
2.3 Oxidative dehydrogenation of ethanol.....	15
2.4 Mesoporous Santa Barbara Amorphous-15 (SBA-15)	17
2.4.1 Synthesis of SBA-15 mesoporous material.....	18
2.4.2 Preparation of SBA-15 material.....	20
2.4.2.1 The sol-gel method	20
2.4.2.2 The hydrothermal method	21
2.5 Supported Metal oxide catalyst.....	23

	Page
2.5.1 Zirconium oxide	23
2.5.2 Lanthanum oxide.....	24
2.5.3 Vanadium oxide	24
2.6 Literature Reviews.....	26
2.6.1 Catalysts in dehydration of alcohol.....	26
2.6.2 Catalysts in oxidative dehydrogenation of alcohol	30
CHAPTER III.....	34
EXPERIMENTAL	34
3.1 Catalyst preparation	34
3.1.1 Chemicals	34
3.1.2 Preparation of SBA-15.....	34
3.1.2.1 Preparation of SBA-15 by sol-gel method.....	34
3.1.2.2 Preparation of SBA-15 by hydrothermal method.....	35
3.1.2.3 Preparation of modified SBA-15 supported catalysts with vanadium oxide	36
3.2 Catalyst characterization.....	36
3.2.1 X-ray diffraction (XRD).....	36
3.2.2 N ₂ physisorption	37
3.2.3 Fourier transform infrared spectroscopy (FTIR)	37
3.2.4 Raman spectroscopy	37
3.2.5 Ultraviolet-visible spectroscopy (UV-Vis)	37
3.2.6 X-ray photoelectron spectroscopy (XPS).....	37
3.2.7 Scanning Electron Microscope (SEM) and Energy X-ray Spectroscopy (EDX).....	38

	Page
3.2.8 Transmission electron microscopy (TEM) and energy dispersive X-ray spectroscopy (EDX)	38
3.2.9 Temperature programmed desorption (NH ₃ -TPD).....	39
3.2.10 Carbon dioxide temperature-programmed desorption (CO ₂ -TPD).....	39
3.3 Reaction study in dehydration of ethanol.....	40
3.3.1 Chemicals and reagents	40
3.3.2 Reaction test.....	40
3.3.2.1 Dehydration of ethanol.....	40
3.3.2.2 Non-oxidative dehydrogenation and oxidative dehydrogenation of ethanol.....	41
CHAPTER IV RESULTS AND DISCUSSIONS.....	45
4.1 Characteristics of SBA-15, Zr/SBA-15 and bimetallic Zr-La/SBA-15 prepared by sol-gel and hydrothermal methods.....	45
4.1.1 X-ray diffraction pattern (XRD)	45
4.1.2 N ₂ physisorption	49
4.1.3 Fourier transform infrared spectroscopy (FT-IR).....	53
4.1.4 Raman spectroscopy.....	55
4.1.5 UV-visible spectroscopy (UV-vis).....	58
4.1.6 Scanning electron microscope and energy dispersive X-ray spectroscopy (SEM/EDX)	60
4.1.6 Transmission electron microscopy (TEM)	63
4.1.7 Temperature-programmed desorption of ammonia (NH ₃ -TPD).....	64
4.2 Ethanol dehydration reaction.....	67

4.3 Non-oxidative dehydrogenation and oxidative dehydrogenation of ethanol over different VO _x /SBA-15 catalysts	75
4.3.1 Characteristics of different VO _x /SBA-15 prepared by sol-gel and hydrothermal methods.....	76
4.3.1.1 X-ray diffraction pattern (XRD).....	76
4.3.1.2 N ₂ -physisorption.....	79
4.3.1.3 Fourier-transform infrared spectroscopy (FTIR).....	83
4.3.1.4 Raman spectroscopy.....	86
4.3.1.5 UV-visible spectroscopy (UV-vis)	88
4.3.1.6 X-ray photoelectron spectroscopy (XPS)	90
4.3.1.7 Scanning electron microscope and energy dispersive X-ray spectroscopy (SEM/EDX).....	95
4.3.1.8 Transmission electron microscopy (TEM) and energy dispersive X-ray spectroscopy (EDX)	97
4.3.1.9 Carbon dioxide Temperature-Programmed Desorption (CO ₂ -TPD).....	101
4.3.2 Catalytic properties	103
4.3.2.1 Non-oxidative dehydrogenation reaction	103
4.3.2.2 Oxidative dehydrogenation reaction	109
4.3.3 Characterization of spent catalysts after reaction	116
CHAPTER V CONCLUSION AND RECOMMENDATIONS	119
5.1 Conclusion	119
5.2 Recommendations	121
REFERENCES	123

	Page
APPENDIX.....	140
APPENDIX A.....	141
APPENDIX B.....	143
APPENDIX C.....	145
APPENDIX D.....	149
APPENDIX E.....	150
VITA.....	151



LIST OF TABLES

	Page
Table 3.1 The chemicals used in the catalysts preparation.....	34
Table 3.2 The chemicals and reagents were used in the reaction.....	40
Table 3.3 Operating conditions for gas chromatogaph.....	44
Table 4.1 Textural properties of the catalysts.....	53
Table 4.2 The amount of each element near the surface of catalyst granule obtained from EDX.....	62
Table 4.3 The surface acidity of all catalysts from NH ₃ -TPD.....	67
Table 4.4 Product yield obtained from ethanol dehydration at 400°C.....	75
Table 4.5 Textural properties of all different VO _x /SBA-15 catalysts.....	83
Table 4.6 The surface basicity of all catalysts from CO ₂ -TPD.....	103
Table 4.7 Relative percentage of elements distribution in spent catalysts obtained from non-oxidative dehydrogenation and oxidative dehydrogenation reaction.....	118
Table B.1 The amount of each element near the surface of different VO _x /SBA-15 catalysts granule obtained from EDX by SEM.....	127
Table B.2 The amount of each element near the surface of different VO _x /SBA-15 catalysts granule obtained from EDX by TEM.....	128

LIST OF FIGURES

	Page
Figure 2.1 Simplified reaction mechanism of ethanol conversion over mixed oxide catalyst.....	12
Figure 2.2 Reaction mechanisms of ethanol catalytic dehydration to olefin under different reaction conditions.....	12
Figure 2.3 A proposed reaction mechanism oxidative dehydrogenation reaction of ethanol to acetaldehyde over the surface vanadium oxide.....	16
Figure 2.4 The representation of SBA-15 before calcination.....	19
Figure 2.5 The representation of SBA-15 after calcination.....	19
Figure 2.6 General scheme of preparation by sol-gel method.....	21
Figure 2.7 Schematic diagram of a Teflon lined stainless steel autoclave for hydrothermal synthesis.....	22
Figure 2.8 Crystal structure of monoclinic (a), tetragonal (b) and cubic zirconia (c)....	23
Figure 2.9 Representation of impregnation of a support with an aqueous solution of NH_4VO_3 followed by calcination in air.....	22
Figure 3.1 Flow diagram of ethanol dehydration systems.....	41
Figure 3.2 Flow diagram of oxidative dehydrogenation systems.....	42
Figure 4.1 XRD patterns of all catalysts obtained from the sol-gel method at low-angle regions.....	47

Figure 4.2 XRD patterns of all catalysts obtained from the sol-gel method at high-angle regions.....	48
Figure 4.3 XRD patterns of all catalysts obtained from the hydrothermal method at low-angle regions.....	48
Figure 4.4 XRD patterns of all catalysts obtained from the hydrothermal method at high-angle regions.....	49
Figure 4.5 Nitrogen adsorption/desorption isotherms of all catalysts synthesized by sol-gel method.....	51
Figure 4.6 Nitrogen adsorption/desorption isotherms of all catalysts synthesized by hydrothermal method.....	51
Figure 4.7 BJH pore size distribution of all catalysts obtained by sol-gel method...	52
Figure 4.8 BJH pore size distribution of all catalysts obtained by hydrothermal method.....	52
Figure 4.9 FTIR spectra of all catalysts obtained by sol-gel method.....	54
Figure 4.10 FTIR spectra of all catalysts obtained by hydrothermal method.....	55
Figure 4.11 Raman spectra of all catalysts obtained by sol-gel method.....	57
Figure 4.12 Raman spectra of all catalysts obtained by hydrothermal method.....	57
Figure 4.13 UV-Vis diffuse reflectance spectra of all catalysts obtained by sol-gel method.....	59

Figure 4.14 UV-Vis diffuse reflectance spectra of all catalysts obtained by hydrothermal method.....	59
Figure 4.15 SEM images of all catalysts obtained by sol-gel and hydrothermal methods.....	61
Figure 4.16 The typical EDX mapping of Zr-La/SBA-15-SG (a) and Zr-La/SBA-15-HT (b) catalysts.....	61
Figure 4.17 TEM images of all catalysts obtained by sol-gel and hydrothermal methods.....	64
Figure 4.18 NH ₃ -TPD profiles of all catalysts obtained by sol-gel method.....	66
Figure 4.19 NH ₃ -TPD profiles of all catalysts obtained by hydrothermal method.....	66
Figure 4.20 The conversion of ethanol over SBA-15 synthesized by sol-gel method.....	68
Figure 4.21 The conversion of ethanol over SBA-15 synthesized by hydrothermal method.....	68
Figure 4.22 The selectivity of products over SBA-15 synthesized by sol-gel method.....	70
Figure 4.23 The selectivity of products over SBA-15 synthesized by hydrothermal method.....	71
Figure 4.24 Yield of ethylene product over SBA-15 synthesized by sol-gel method.....	74
Figure 4.25 Yield of ethylene product over SBA-15 synthesized by hydrothermal method.....	74

Figure 4.26 XRD patterns of all catalysts obtained from the sol-gel method at low-angle regions.....	77
Figure 4.27 XRD patterns of all catalysts obtained from the sol-gel method at high-angle regions.....	78
Figure 4.28 XRD patterns of all catalysts obtained from the hydrothermal method at low-angle regions.....	78
Figure 4.29 XRD patterns of all catalysts obtained from the hydrothermal method at high-angle regions.....	79
Figure 4.30 Nitrogen adsorption/desorption isotherms of all catalysts synthesized by sol-gel method.....	81
Figure 4.31 Nitrogen adsorption/desorption isotherms of all catalysts synthesized by hydrothermal method.....	81
Figure 4.32 BJH pore size distribution of all catalysts obtained by sol-gel method.....	82
Figure 4.33 BJH pore size distribution of all catalysts obtained by hydrothermal method.....	82
Figure 4.34 FTIR spectra of all catalysts obtained by sol-gel method.....	85
Figure 4.35 FTIR spectra of all catalysts obtained by hydrothermal method.....	85
Figure 4.36 Raman spectra of all catalysts obtained by sol-gel method.....	87
Figure 4.37 Raman spectra of all catalysts obtained by hydrothermal method.....	87
Figure 4.38 UV-Vis diffuse reflectance spectra of all catalysts obtained by sol-gel method.....	89

Figure 4.39 UV-Vis diffuse reflectance spectra of all catalysts obtained by hydrothermal method.....	89
Figure 4.40 Full XPS spectrum of all catalysts obtained by sol-gel method.....	92
Figure 4.41 Full XPS spectrum of all catalysts obtained by hydrothermal method.....	92
Figure 4.42 XPS spectra for O 1s and V 2p spectra of all catalysts obtained by sol-gel method.....	93
Figure 4.43 XPS spectra for O 1s and V 2p spectra of all catalysts obtained by hydrothermal method.....	93
Figure 4.44 XPS spectra for Zr 3d spectra of all catalysts obtained by sol-gel method.....	94
Figure 4.45 XPS spectra for Zr 3d spectra of all catalysts obtained by hydrothermal method.....	94
Figure 4.46 SEM images of all catalysts obtained by sol-gel and hydrothermal methods.....	96
Figure 4.47 The typical EDX mapping of V-Zr-La/SBA-15-SG (left) and V-Zr-La/SBA-15-HT (right) catalysts.....	96
Figure 4.48 TEM micrographs of all catalysts obtained by sol-gel and Hydrothermal methods.....	99
Figure 4.49 TEM micrographs of nanoscale V-Zr-La/SBA-15 (-SG (Figure 4.49a) and -HT (Figure 4.49b)) catalysts with electron diffraction mode.....	99

Figure 4.50 The typical TEM-EDX elemental mapping and EDX of the plotted area of V-Zr-La/SBA-15-HT catalyst.....	100
Figure 4.51 CO ₂ -TPD profiles of all prepared catalysts.....	102
Figure 4.52 Conversion (a) and selectivity (b) of different VOx/SBA-15 catalysts (SG) in non-oxidative dehydrogenation.....	106
Figure 4.53 Conversion (a) and selectivity (b) of different VOx/SBA-15 catalysts (HT) in non-oxidative dehydrogenation.....	106
Figure 4.54 Yield of acetaldehyde product obtained from non-oxidative dehydrogenation reaction over different VOx/SBA-15 catalysts synthesized by sol-gel (a) and hydrothermal (b) method.....	108
Figure 4.55 Conversion (a) and selectivity (b) of different VOx/SBA-15 catalysts (SG) in oxidative dehydrogenation.....	113
Figure 4.56 Conversion (a) and selectivity (b) of different VOx/SBA-15 catalysts (HT) in oxidative dehydrogenation.....	114
Figure 4.57 Yield of acetaldehyde product obtained from oxidative dehydrogenation reaction over different VOx/SBA-15 catalysts synthesized by sol-gel (a) and hydrothermal (b) method.....	108
Figure 4.58 SEM images of fresh catalyst (a) and spent catalyst of V-Zr-La/SBA-15-HT from non-oxidative dehydrogenation (b) and oxidative dehydrogenation (c) reaction respectively.....	117
Figure C.1 The calibration curve of ethanol.....	130

Figure C.2 The calibration curve of ethylene.....	130
Figure C.3 The calibration curve of diethyl ether.....	131
Figure C.4 The calibration curve of acetaldehyde.....	131
Figure C.5 The calibration curve of carbon monoxide (CO).....	132
Figure C.6 The calibration curve of carbon dioxide (CO ₂).....	132



CHAPTER I

INTRODUCTION

1.1 General introduction and rational

In recent times, biomass utilization has been receiving increasing attention due to the need to reduce greenhouse gases and concerns about the dependence on petroleum feedstocks for energy supply. Much is expected from a partial shift to biomass-derived ethanol to reduce carbon dioxide emissions [1, 2]. Recently, considerable developments have been reported in the use of ethanol and ethanol based oxygenates as alternative motor vehicle fuels, fuel additives [3] or as a feedstock to produce hydrogen [4, 5]. On the other hand, there is also growing interest in converting ethanol to ethylene and acetaldehyde because these are important starting chemicals for the chemicals industry [6]. The ethanol dehydration provides many advantages such as lower operating temperature and green manufacturing of ethylene. Hence, the development of dehydration performance has been widely studied in both industry and academia [7-10]. Dehydration of ethanol to ethylene is preferably carried out over solid acids such as alumina, zeolite, silica, silica–alumina and mixed metal oxide (such as titanium oxides, cobalt oxides, chromium oxide and silver salt of tungstophosphoric acid) [11-15]. For commercial dehydrogenation to acetaldehyde supported copper and palladium or basic oxides such as magnesium oxide are employed [16-18]. On the other hand, the oxidative dehydrogenation (ODH) reactions are also an attractive alternative to classical dehydrogenations. In oxidative dehydrogenation reactions, the abstracted hydrogen is oxidized, releasing heat of reaction, and the conversion becomes significant at a much lower reaction temperature. However, one of the main points in catalyst

optimization is to minimize the consecutive reactions [19]. All of reaction processes occur also over some transition metal oxides such as ZnO, ZrO₂, V₂O₅, Fe₂O₃ and Mn₂O₃ and the selectivity depends on the surface acid-base properties of the oxide [14, 20].

In general, mesoporous silicas have been reported to partake in this reaction due to the existence of Si–O–Si or Si–O[−] entities [21, 22]. Ordered mesoporous silicas have attracted widespread interest in many frontier areas of science and technology due to their potential applications in various fields. Compared with the microporous zeolites, which present severe mass transfer limitations when large reactant molecules are involved, especially in liquid-phase systems for the synthesis of fine chemicals [23, 24]. Many reviews have summarized the catalytic applications of mesoporous silica [25, 26] or mesoporous zeolite [27] as catalyst supports. There are many strategies for the design and synthesis of mesoporous catalysts special characteristic features like exceptionally high surface area, uniform and well-defined pores of nanoscale dimensions, which can be adjusted over a large range (2 - 20 nm) [28]. The high internal surface area of typically 400-900 m²/g makes SBA-15 a well suited material for various applications. Not only because of its larger pores, but also thermal, mechanical and chemical resistance properties that makes it a preferable choice to other types of catalysts [29]. However, pure mesoporous molecular sieves have no intrinsic catalytic activity due to the absence of heteroatom activity sites. It is necessary to replace part of the silicon of the structure onto the internal surface of the pores heteroatoms such as Ti, V, Al, Mo, Cr, Fe, into the framework by impregnation of active components or immobilization of active species with pre-determined structure, which are able to make the solids catalytically active with specific properties [30, 31]. Indeed, transition-metal incorporated mesoporous silicas are of great interest because these metal functionalized materials may find use in catalysis, such as acid catalysis and base catalysis [32].

In particular, zirconium incorporated mesoporous silicas are particularly interesting because of the important applications of Zr-based materials in a wide variety of areas in heterocatalysis. It is important to introduce an effective method to synthesize metal (M–O–Si) containing SBA-15. However, little attention has been paid to the synthesis and application of the SBA-15 materials containing bimetallic heteroatoms, which can introduce new catalytic sites into mesoporous materials. It is well known that bimetal (Zr and La) incorporated SBA-15 mesoporous materials with a desirable ordered two-dimensional hexagonal structure, which can create new active sites, were synthesized by a direct hydrothermal method under a self-generated acidic condition in the absence of hydrochloric acid [33]. The improved catalyst activity has been suggested to be due to surface modification and changes of the interaction between metal and support. Thus, zirconium and bimetal (Zr and La) containing mesoporous silicas (SBA-15) were used as catalysts for ethanol dehydration, which is alternative way for improvement of the catalytic performance. Each type of solid catalyst has a different structure and properties such as hydrothermal method, sol-gel technique, solid state route [34, 35], and microwave-hydrothermal process [36]. The sol-gel method has been proposed as the traditional method, but the precipitated powders obtained are amorphous in nature and further heat treatment is required for crystallization. Hydrothermal method is an alternative route for one-step synthesis of mesoporous silicas nanoparticles. Particle morphology, crystalline phase, and surface chemistry of the products can be controlled by regulating precursor composition, reaction temperature, pressure, solvent property, and aging time [37, 38]. The conventional sol-gel and one-step hydrothermal methods are commonly used for synthesis of SBA-15.

Vanadium oxide based catalysts have been tested in a large variety of oxidation reactions, such as oxidation of methanol, methane and olefins, the

oxidation and ammoxidation of aromatic hydrocarbons and the selective catalytic reduction of NO_x [39, 40]. For instance, V/SBA-15 catalysts showed good catalytic activity and selectivity in oxidative dehydrogenation (ODH) reactions, due to high concentration of isolated or low polymeric VO_x species and enhances the strength of basic sites at the surface [41, 42]. It is interesting for being used as a catalyst for non-oxidative dehydrogenation and oxidative dehydrogenation of ethanol to acetaldehyde. Furthermore, the catalyst was modified by adding vanadium into surface catalysts (V/SBA-15, V-Zr/SBA-15 and V-Zr-La/SBA-15) that can improve catalytic performance and surface properties.

The aim of the present research is to develop the zirconium and bimetal (Zr and La) containing mesoporous silicas (SBA-15) for ethanol dehydration via sol-gel method to create a mesostructured form. However, the overall process of this method requiring a long time period over 40 h [43, 44] and high temperature treatment, which may generate gaseous pollutants (such as CO_2 and NO_x) [27] and may partially destroyed the ordered structure of the mesoporous material. For this reason, we used an alternative method called the one-step hydrothermal method without addition of hydrochloric acid for environmentally friendly and making new active sites. In addition, vanadium-containing catalysts were also investigated for non-oxidative dehydrogenation and oxidative dehydrogenation of ethanol to acetaldehyde. The former catalyzes the formation of ethylene from ethanol selectively, while the latter produces both ethylene and acetaldehyde from ethanol. The catalysts were characterized using various techniques.

1.2 Research objectives

1.) To investigate and compare the characteristics, catalytic properties and catalytic performance of SBA-15, Zr/SBA-15 and Zr-La/SBA-15 catalysts obtained from the sol-gel and hydrothermal methods for ethanol dehydration reaction.

2.) To measure yield and productivity using vanadium-containing SBA-15 catalysts (V/SBA-15, V-Zr/SBA-15 and V-Zr-La/SBA-15) for dehydrogenation and oxidative dehydrogenation of ethanol to acetaldehyde.

1.3 Research scopes

1.) Using SBA-15, Zr/SBA-15 and Zr-La/SBA-15 catalysts obtained from the sol-gel and hydrothermal method over the ethanol dehydration.

2.) Testing product distribution in ethanol dehydration over SBA-15 based solid acid catalysts at 1 atm and 200 to 400 °C.

3.) Investigation of modified SBA-15 supported catalysts with vanadium oxide.

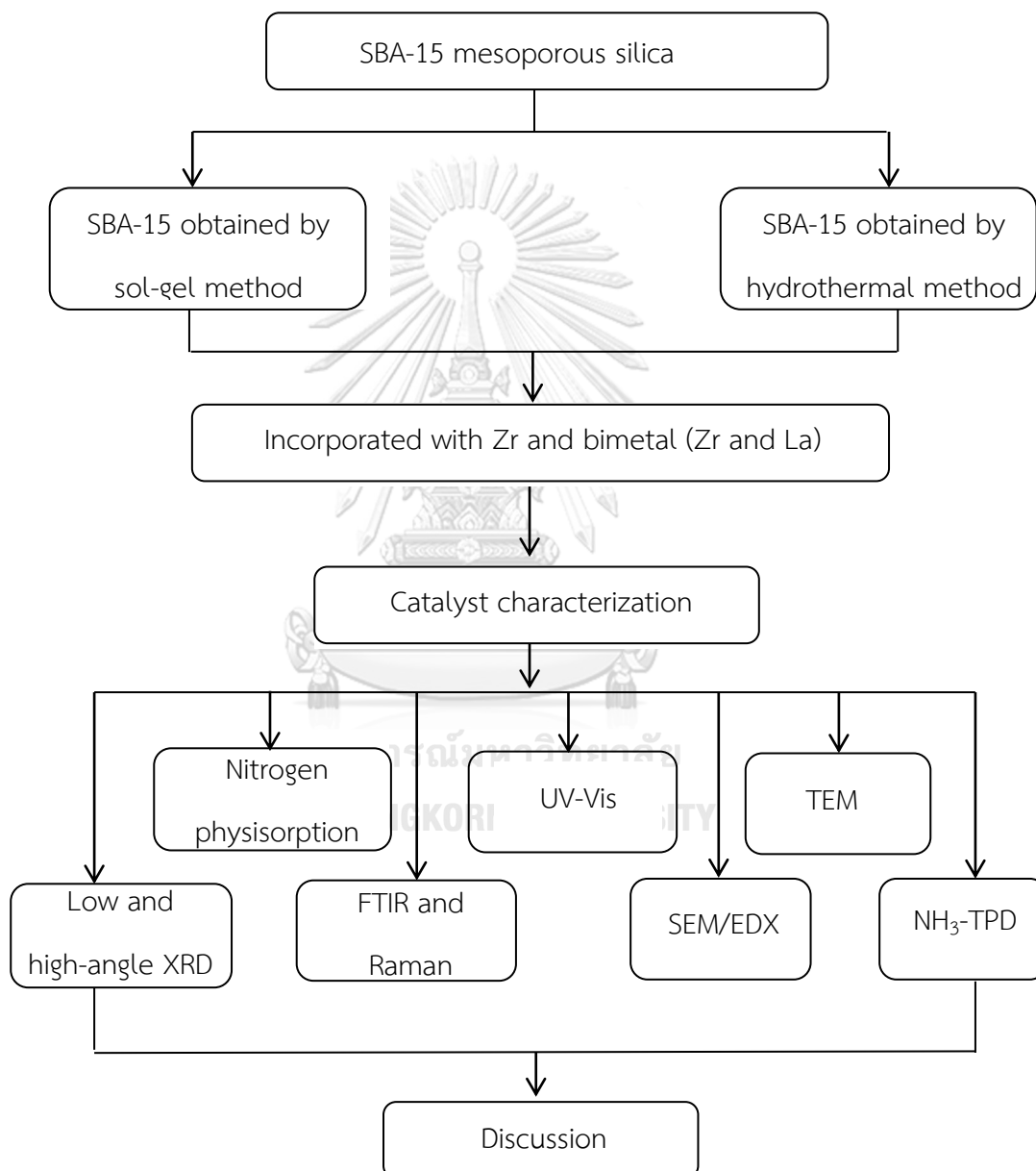
4.) Testing catalytic activity of vanadium-containing SBA-15 catalysts over the ethanol dehydrogenation and oxidative dehydrogenation at 1 atm and 200 to 400 °C.

5.) The structural and surface properties of all catalysts were characterized by low and high-angle XRD, nitrogen physisorption, FTIR, Raman, UV-Vis, SEM/EDX, TEM, NH₃-TPD and CO₂-TPD techniques.

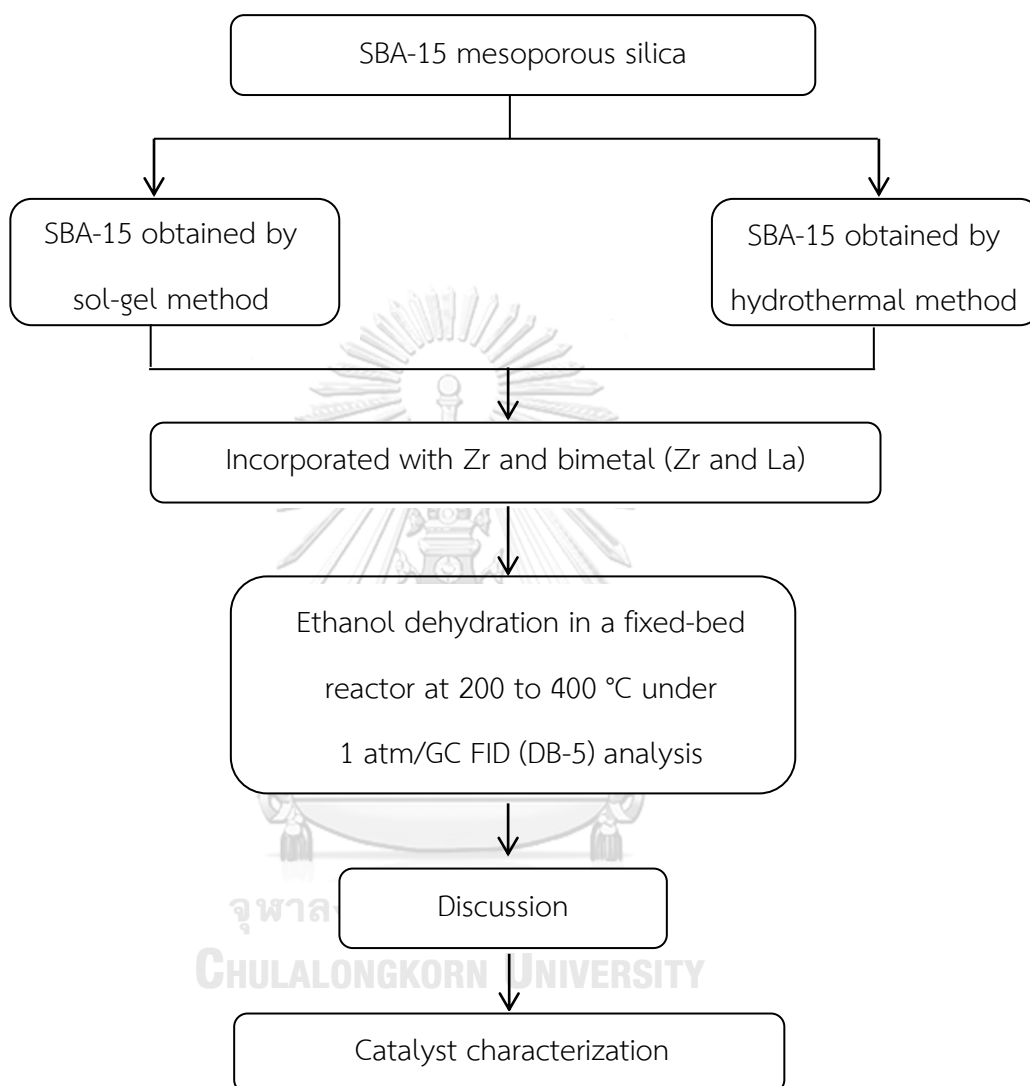
1.4 Research methodology

Research methodology is below;

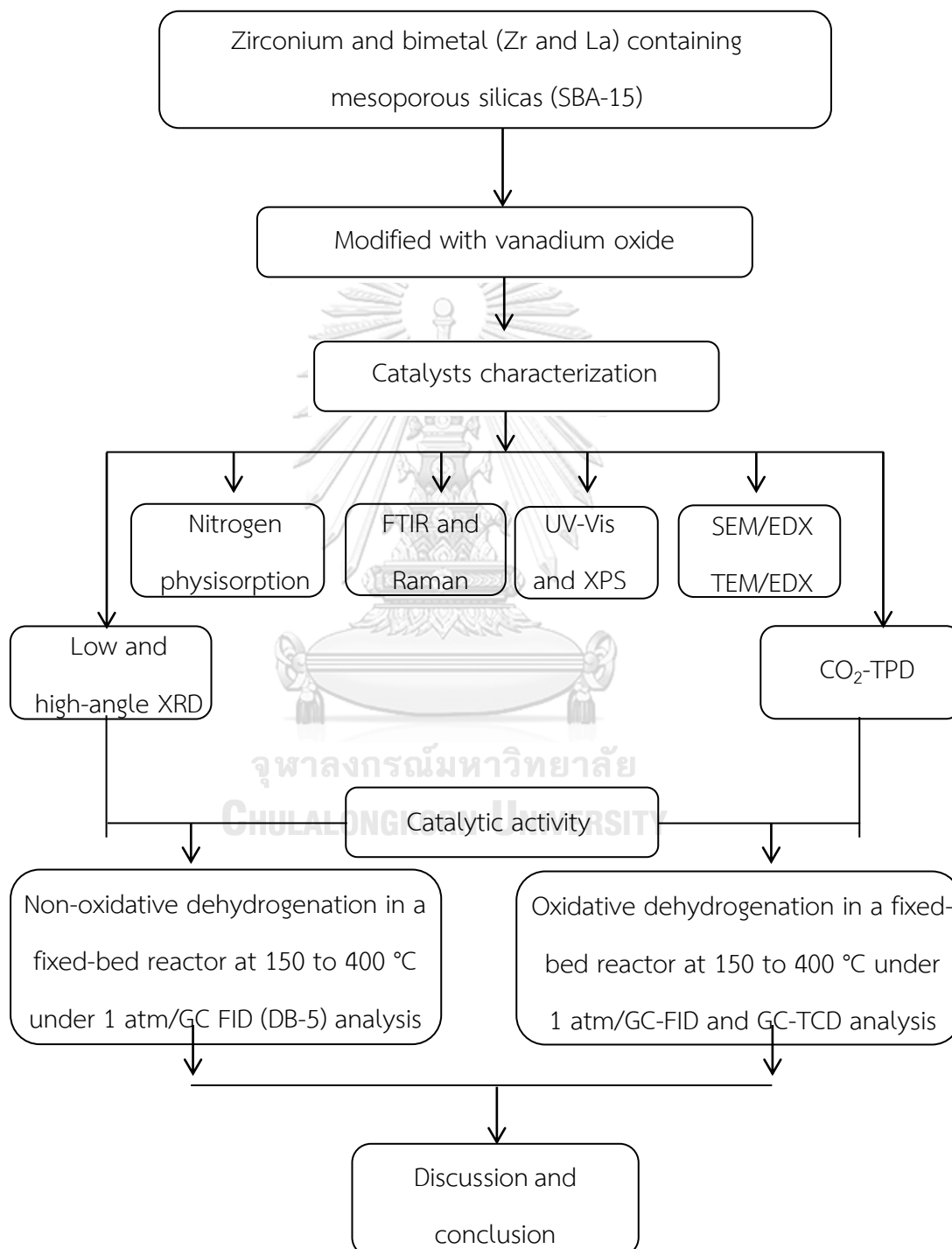
Part I: Comparative study of catalytic activity of SBA-15 supported catalysts.



Part II: Investigation of the catalytic activity and product selectivity for ethanol dehydration.



Part III: Investigation of modified SBA-15 supported catalysts with vanadium oxide for non-oxidative dehydrogenation and oxidative dehydrogenation.



As mentioned above, it explains about the motivation of research, research scopes, and research methodology. Henceforth, the content of thesis is arranged as follows:

Chapter 2 contains basic knowledge of ethanol dehydration reaction, non-oxidative dehydrogenation and oxidative dehydrogenation of ethanol and the catalysts used in these reactions.

Chapter 3 describes the experimental procedure for catalysts preparation, procedures for reaction testing, and instrument for characterization.

Chapter 4 Results and discussions

Chapter 5 Conclusion and recommendations



CHAPTER II

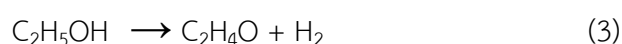
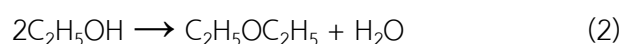
THEORY AND LITERATURE REVIEWS

The dehydration and oxidative dehydrogenation of alcohols on metal oxide containing mesoporous silicas (SBA-15) catalysts have been studied. Generally, alkene is yielded by the dehydration (ether is produced at a relatively low temperature) on solid acid catalysts, while aldehyde and ketone is yielded by the dehydrogenation on basic catalysts. The basic knowledge of ethanol dehydration and the oxidative dehydrogenation reaction and the solid acid-base catalysts used in this reaction follows in Chapter 2.

2.1 Ethanol dehydration reaction

Ethanol consists of hydroxyl group in molecule. It can be dehydrated by using solid acid catalysts. In the catalytic dehydration of ethanol to form ethylene, an acid catalyst first protonates the hydroxyl group, which leaves as a water molecule. The conjugate base of the catalyst then deprotonates the methyl group, and the hydrocarbon rearranges into ethylene or diethyl ether. In addition to the main product of ethylene and the main byproduct of ether, the reaction of ethanol dehydration may also generate a small amount of byproducts such as acetaldehyde, hydrocarbons (methane, ethane, propylene) and etc. The reaction is endothermic, and because of this, the optimal reaction temperature is fairly high, ranging from 180 °C to 500 °C. Maintaining the reaction temperature constitutes much of the energy cost in industrial application of the reaction, since competing reactions into diethyl ether or acetaldehyde are favored outside of the temperature range and so decrease

ethylene yield [45, 46]. Among the secondary intermediates potentially obtainable by converting ethanol, ethylene and diethyl ether (DEE) can be obtained by catalytic dehydration using a solid acid catalyst upon reactions as follows [47];



The first reaction (1) has already been applied at the industrial level in the 1960s using aluminas as the catalysts [48]. The second reaction (2) occurs on the same catalysts under low temperature at moderate ethanol conversion, allowing very high selectivity and significant yields (>70%). In addition, acetaldehyde can be obtained by dehydrogenation of ethanol as seen in the third reaction (3).

The simplified reaction mechanism of ethanol catalytic conversion over mixed oxides is presented in **Figure 2.1**. Ethylene is formed by catalytic dehydration of ethanol which requires one ethanol molecule to generate carbocation during the reaction. In the First, the proton from acid catalyst protonates the hydroxyl group of ethanol molecule to remove the water molecule. Then, the conjugate base of the catalyst then deprotonates the methyl group, and the hydrocarbon rearranges into ethylene [45]. This reaction requires strong acid site or Brønsted acid site [49-51], and redox reaction leading to dehydrogenation rather than dehydration. This is an easy reaction occurring typically in very mild conditions and the rate limiting step of the reaction is thus water desorption to regenerate the active site.

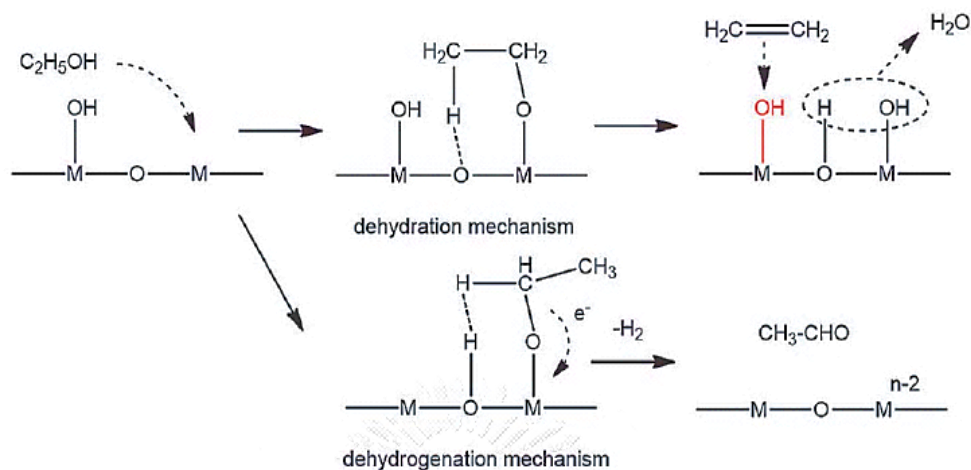


Figure 2.1 Simplified reaction mechanism of ethanol conversion over mixed oxide catalysts [52].

There are mainly three kinds of reaction mechanisms of ethanol catalytic dehydration to olefin under different reaction conditions, namely, E1, E2, and E1cB mechanism, where A and B are the acidic and basic centers of the catalyst, respectively (Figure 2.2).

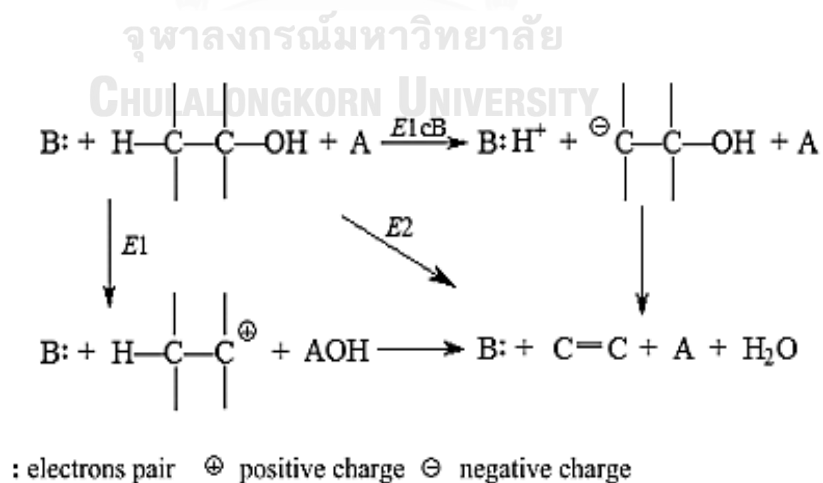


Figure 2.2 Reaction mechanisms of ethanol catalytic dehydration to olefin under different reaction conditions [50].

The reactions of E1, E2, and E1cB are elimination reactions, and the three are competitive reactions. The E1 reaction is a single-molecule elimination reaction, and it first generates a carbonation intermediate, which is the rate controlling step and is a first-order reaction, then quickly loses β -hydrogen to generate olefin. The E2 reaction is a bimolecular elimination reaction, and the reaction is finished in one step; the reaction rate is influenced by the concentration of the two compounds, which is a second order reaction. E1cB reaction is a single-molecule conjugate base elimination reaction; in the reaction process, the nucleophilic center first captures β -hydrogen of the reactant to generate carbanion (conjugate base), and then the hydroxyl of the conjugate base leaves to generate olefin, which is the first step reaction and should be an equilibrium reaction with a quicker rate. The second step is the rate-limiting step in the overall reaction with a slower rate, influenced only by the concentration of one kind of molecule. In addition, the carbocations in the E1 reaction will not generate ethanol, the E2 reaction is not reversible, and the carbanion of the E1cB reaction can generate ethanol. The reaction mechanism of ethanol dehydration process is influenced by such factors as ethanol, catalyst type, and so on.

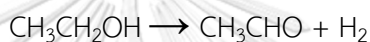


2.2 Ethanol dehydrogenation reaction

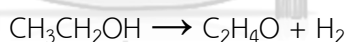
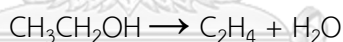
Ethanol dehydrogenation has been studied on several copper-supported catalysts, such as CuO/ZnO/Al₂O₃, Cu/ZnO, Cu/Cr₂O₃, etc. Extensive research from ethanol dehydrogenation has already been performed in 1951. The catalyst was also able to maintain its activity after periodic reactivation. The deposition of copper on a suitable support enhances its lifetime and activity due to a higher metal dispersion. In addition, if a supported copper catalyst is promoted with oxides of zinc, cerium, thorium and zirconium, a stable activity in a fixed bed reactor catalyst could be

achieved. The energy for bond breaking in an ethanol molecule ranks in the following increasing order: O-H > -CH₂- > C-C > -CH₃. Therefore, it can be foreseen in a first approximation that a sequence of elementary processes for activating ethanol occurs at increasing temperature, whatever be the catalyst.

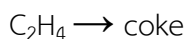
During dehydrogenation, nucleophile addition of basic catalysts cause hydrogen removing from the alcohol reactant. The easiest step is the formation of surface adsorbed ethoxy species, CH₃CH₂O_{ads}, from the OH group dehydrogenation. Then the ethoxy intermediates further dehydrogenate to produce acetaldehyde. Both steps can be lumped as:



Several side reactions, catalytic or not, might be considered as well, like ethanol dehydration to ethylene and diethyl ether, which might be favored on acidic supports:



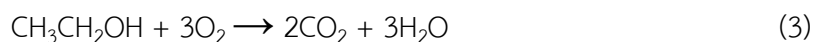
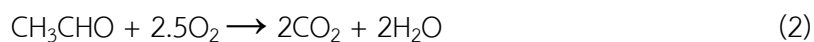
Coke formation from ethylene oligomerization/condensation:



Both, the dehydrogenation to the acetaldehyde and dehydration to ethylene occur depending on the nature of the support. In general, a high surface basicity will favor dehydrogenation rather than dehydration. Acidic supports induced ethanol dehydration to produce ethylene, which was a precursor of coke formation.

2.3 Oxidative dehydrogenation of ethanol

Oxidation catalysts belong to a wider class of materials having redox or oxidoreductive type characteristics. Presence of a transition metal as the principal active component (V, Mo, Cu, Fe, Pd, Pt, Rh, Ag). Often in these cases, a second element is also present which can be transition or post transition (for example, P, Sb or Bi), which contributes to establishing the reactive characteristics of the catalyst. Selective oxidation of ethanol results in the formation of acetaldehyde, 1,1-diethoxyethane, acetic acid, and ethyl acetate. Currently, 75 % of acetic acid is formed via methanol carbonylation utilizing fossil resources and 25 % by classical fermentation [53]. Gold catalysts were found to be active and selective in the synthesis of both acetic acid and ethyl ester in the presence of oxygen [54, 55]. Moreover, the use of gold catalysts allowed for the use of less severe reaction conditions compared to those needed for other catalysts active in the gas-phase such as supported V_2O_5 (175–200 °C, 270 kPa) [6, 56]. The reaction products analyzed with GC–MS and GC methods were CO_2 , H_2O , acetaldehyde (CH_3CHO), and ethanol which was unreacted and remained in the system after reaction. The equations for three possible chemical pathways are listed as follows [57]:



It is important to note that the product composition depends on the reaction conditions employed as well as the nature of the catalysts, including the metal particle size and the composition of the support. The acetaldehyde formation was consistent with the following proposal regarding the reaction mechanism. As a first step, ethanol is adsorbed on the vanadium oxide surface to form activated

intermediate species (vanadium peroxy) that can withdraw the α -hydrogen from ethanol, thereby favoring the formation of acetaldehyde (**Figure 2.3**). Consequently, aldehyde is oxidized to acetic acid, while CH_3CHO can also undergo C–C bond cleavage to produce CO_2 . The selectivity was influenced by the ethanol concentration. At ethanol concentration lower than 60 wt. %, the major product was acetic acid, whereas when the concentration exceeded 60 wt. %, the selectivity shifted towards ethyl acetate [55].

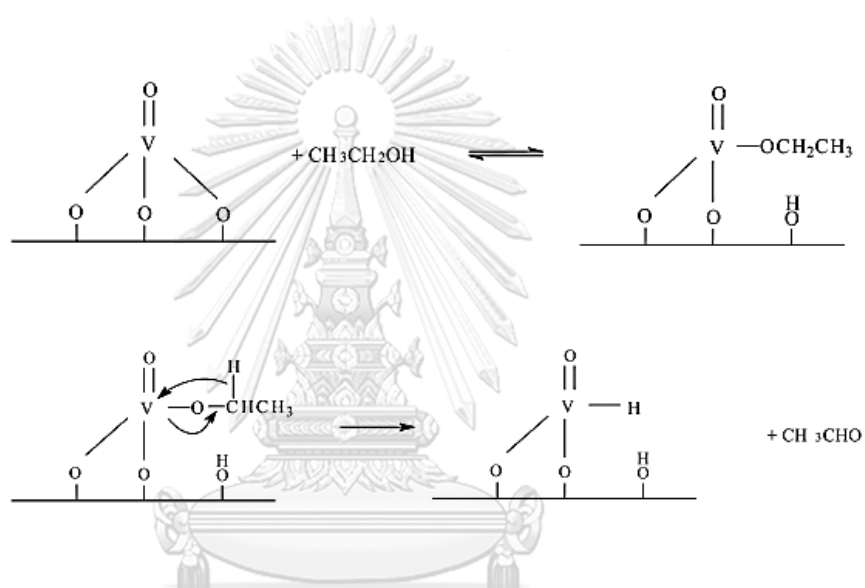


Figure 2.3 A proposed reaction mechanism oxidative dehydrogenation reaction of ethanol to acetaldehyde over the surface vanadium oxide [58].

However, the oxidative dehydrogenation route seemingly offers the advantages of potentially higher conversion achievable at a lower reaction temperature. Savings in heating costs can be made if the dehydrogenation reaction is made exothermic by the introduction of oxygen. Also, for a catalytic oxidative dehydrogenation process, deactivation would be reduced since coke formed on the catalyst should be removed by oxygen. Unfortunately, there are selectivity problems with the oxidative dehydrogenation reaction. In the presence of oxygen, other

oxidation reactions including partial oxidation of aldehyde (R-CHO) compounds to other products such as acetic acid and combustion to carbon oxides (CO and CO₂) can occur, reducing selectivity. The total oxidation of the alcohol to CO and CO₂ are highly undesirable. Also, despite the favourable thermodynamic data at room temperature, reaction temperatures above 400°C are required to achieve acceptable reaction rates. Higher reaction temperatures may also improve the selectivity of the reaction. No commercial plants for the oxidative dehydrogenation of ethanol are known to be currently operational, but pilot and demonstration units have been built and operated [57].

2.4 Mesoporous Santa Barbara Amorphous-15 (SBA-15)

Ordered mesoporous silicas have attracted widespread interest in many frontier areas of science and technology due to their potential applications in various fields, such as adsorption, sensors, photonics, drug delivery, catalysis, and etc. [59]. During the last two decades, various mesoporous structures have been synthesized, which can be roughly classified into three categories based on the pore types: nearly spherical cage, cylindrical channel and bi-continuous channel [60]. Mesoporous materials are more preferred for their highly ordered mesostructure, apart from high surface area, which allows diffusion and adsorption of larger molecules for wide applications than that of microstructure which only limits to separation and fine chemical catalysis [61]. Moreover, microporous material has selective thermal stability based on size and shape of cage or channel within lattice of selected organic moieties during synthesis, which restricts its potentiality to limited applications [62]. Typical compounds of mesoporous material include silica, alumina, carbon and transition metal oxides.

Mesoporous silica was first discovered in 1990 by Yanagisawa et al. [63]. In 1998, a prominent research which produces hexagonal array of pores namely as Santa Barbara Amorphous no 15 (SBA-15) with larger pore size from 4.6-30 nm was a research gambit in mesoporous material development by Zhao et al. [44]. Many reviews have summarized the catalytic applications of SBA-15 mesoporous silica as catalyst supports. There are many strategies for the design and synthesis of mesoporous catalysts, owing to the uniform pore size, extremely high surface area, high degree of structural ordering, larger pore size, thicker pore walls, ease of synthesis, and higher hydrothermal/thermal stability in comparison to MCM-41, MCM-48, and HMS mesoporous materials [64].

2.4.1 Synthesis of SBA-15 mesoporous material

Typical synthesis of SBA-15 requires triblock copolymer, typically non-ionic triblock copolymers structure directing agent. Poly(ethylene glycol)-block-poly(propylene glycol)-block-poly(ethylene glycol) or PEG-PPG-PEG (P-123) is normally used because of its mesostructure properties, inexpensive and biodegradability. A chemical reaction is started when the silica source, such as tetramethyl orthosilicate (TMOS), tetraethyl orthosilicate (TEOS) and tetrapropyl orthosilicate (TPOS) are mixed with the solution.

According to Zhao et al. [44] the formation of ordered hexagonal SBA-15 with uniform pores up to 30 nm was synthesized using amphiphilic triblock copolymer in strong acidic media i.e., pH ~1. If pH is more than the isoelectric of silica i.e., at pH 2-6, no precipitation or formation of silica gel would occur. They suggested that the prehydrolyzed of TEOS at pH<3 would interact with template agent to form a mesophase under weak acidic condition [65]. Template removal is one of the crucial aspects in ordered mesoporous silica synthesis in which this procedure could modify the final properties of desired porous structure. The usual method of removing

template is calcination. The calcination of mesoporous structure SBA-15 at 500 °C would produce final properties of porous structure with interlattice d spacing of 74.5-320 angstroms between the (100) planes, pore volume fraction up to 0.85 and silica wall thickness of 31-64 angstroms [66]. Besides mesoporosity structure, SBA-15 was found to contain micropores which indicated the hierarchical template of material structure [67]. These microporous structures are generally disordered and provide interconnectivity between ordered mesopores [68].

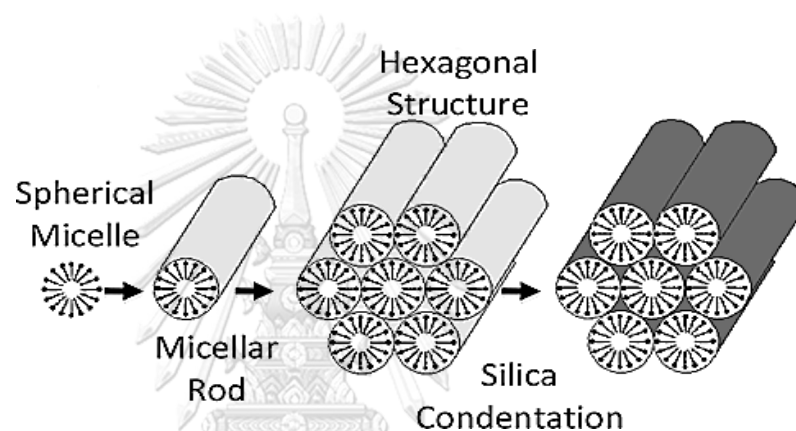


Figure 2.4 The representation of SBA-15 before calcination.

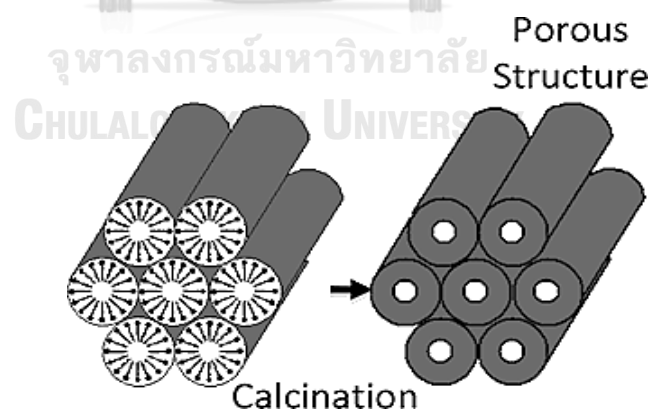


Figure 2.5 The representation of SBA-15 after calcination.

The proposed mechanisms for synthesis of SBA-15, the self-assembly route occurs through cooperative self-assembly, and the micellar rod cannot be formed before addition of the silica source. The micelles become elongated by the condensation of the silica source. The micellar rods arrange in a hexagonal pattern while the silica walls are built. The polymerization is simultaneous to the elongation and the silica precursor is polymerized on the PEG chains, and the water content in this area decreases to produce a change in the polarity resulting in a reduced curvature of the micelle (**Figure 2.4**) [28, 69]. The porous structures are not mesoporous because of the hexagonal arrangement of cylindrical aggregates. On the other hand, the PEG penetrates the pore walls, resulting in the microporous production after calcination as illustrated in **Figure 2.5** [69]. This process allows to remove the surfactants from SBA-15.

2.4.2 Preparation of SBA-15 material

Various synthetic pathways have been employed for the preparation of SBA-15 materials with different particle sizes and morphologies, such as hydrothermal method, sol-gel technique, solid state route [34, 35], and microwave-hydrothermal process [36].

2.4.2.1 The sol-gel method

The synthesis by sol-gel route permitted the formation of many oxides in various configurations (monolithic, thin films, fibers, powders). This great diversity is attractive in various technological fields like optic, electronic, biomaterials, photocatalysis etc [70]. The sol-gel method is based on the phase transformation of a sol obtained from metallic alkoxides or organometallic precursors. The sol is a liquid suspension of solid particles ranging in size from 1 nm to 1 micron. It can be

obtained by hydrolysis and partial condensation of precursors such as an inorganic salt or a metal alkoxide. The further condensation of sol particles into a three dimensional network produces a gel material (**Figure 2.6**). The solvent is removed by drying the gel and the next step is a proper heat treatment. Some of the advantages of the sol-gel method are its versatility and the possibility to obtain high purity materials, the provision of an easy way for the introduction of trace elements, allowance of the synthesis of special materials and energy savings by using low processing temperature [71].

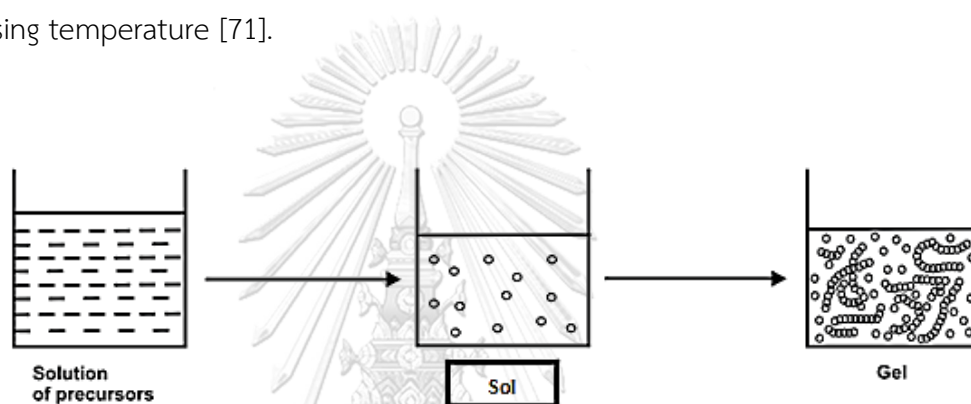


Figure 2.6 General scheme of preparation by sol-gel method.

2.4.2.2 The hydrothermal method

The method is based on the ability of water and aqueous solutions to dilute at high temperature (500 °C) and pressure (10-80 MPa, sometimes up to 300 MPa) substances practically insoluble under normal conditions: some oxides, silicates, sulphides. The main parameters of hydrothermal synthesis, which define both the processes kinetics and the properties of resulting products, are the initial pH of the medium, the duration and temperature of synthesis, and the pressure in the system. The synthesis is carried out in autoclaves which are sealed steel cylinders that can withstand high temperatures and pressure for a long time [72].

Water is one of the most important solvent present in nature in abundant amount and has remarkable properties as a reaction medium under hydrothermal conditions. Water shows different characteristics under hydrothermal conditions than that of standard conditions. One of the biggest advantages of using water is the environmental benefit and cheaper than other solvents, and it can act as a catalyst for the formation of desired materials by tuning the temperature and the pressure. It is nontoxic, nonflammable, noncarcinogenic, nonmutagenic, and thermodynamically stable. Another advantage is that water is very volatile, so it can be removed from the product very easily.

Advantages of the hydrothermal synthesis method include the ability to synthesize crystals of substances which are unstable near the melting point, and the ability to synthesize large crystals of high quality. Disadvantages are the high cost of equipment and the inability to monitor crystals in the process of their growth. There is also a group of solvothermal synthesis methods, relational to hydrothermal methods; this group of methods is based on the use of organic solvents and supercritical media. The reaction is carried out in closed system using autoclaves, an apparatus shown in **Figure 2.7**.

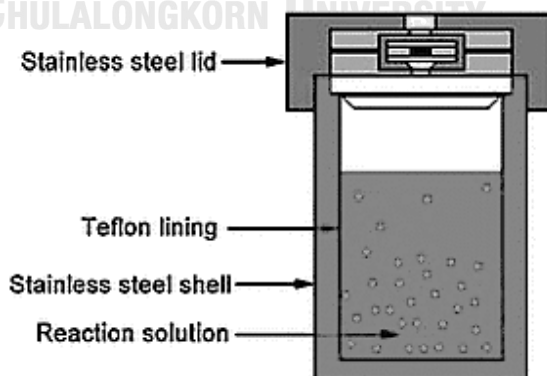


Figure 2.7 Schematic diagram of a Teflon lined stainless steel autoclave for hydrothermal synthesis [73].

2.5 Supported Metal oxide catalyst

2.5.1 Zirconium oxide

Zirconium oxide structure is polymorph (i.e. different arrangements of same atoms). The three different main variations are temperature dependent - monoclinic, tetragonal and cubic (**Figure 2.8**). They can reversibly transmute relatively easily and fast due to the martensitic phase change character, which is not diffusion independent [74].

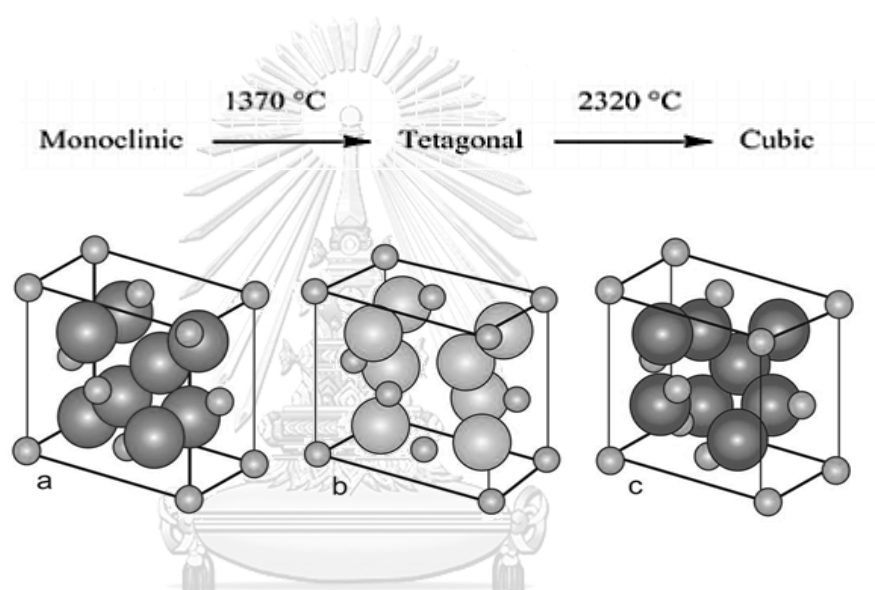


Figure 2.8 Crystal structure of monoclinic (a), tetragonal (b) and cubic zirconia (c) [75].

Zirconia is currently attracting considerable interest as support material in a variety of catalyst systems. In most of the cases, this interest can be ascribed to at least one of the following two properties of zirconia [76]:

(i) As a carrier, it gives rise to a unique kind of interaction between the active phase and support, this being manifested in both the catalytic activity and the selectivity pattern of the system

(ii) It is more chemically inert than the classical supports (e.g. Al₂O₃ and SiO₂).

For most industrial applications, supports must possess a high accessible specific surface area, good thermal and chemical stabilities, and high mechanical strength. We have previously shown that zirconia with a high specific surface area and a well-developed mesoporous texture can be made by means of gel-precipitation [77].

2.5.2 Lanthanum oxide

Lanthanum oxide is the oxide of the rare earth metal Lanthanum. It is produced by calcining lanthanum salts as lanthanum nitrate or lanthanum hydroxide at temperatures above 400 °C. The substance is used as a catalyst component in industrial settings and as a component in automotive catalytic converters. Lanthanum Oxide is a component of Fluid Catalytic Cracking (FCC) catalysts. The use of lanthanum oxide in FCC catalysts can increase the yield of gasoline by as much as 10 percent. Lanthanum oxide performs several critical roles in the FCC catalyst. It is used to prevent rapid deactivation of the catalyst and to isolate and remove heavy metals, and it assists in controlling the activity, coke selectivity, and olefin selectivity of the zeolite portion of the catalyst [78, 79].

2.5.3 Vanadium oxide

Vanadium is the most important metal used in metal oxide catalysis [80]. About 5% of the annual production of vanadium is used in catalysis, which is its most dominant non-metallurgical use. The catalysts containing vanadia, whether pure or mixed with other oxides have been used in many industrial processes, which yield valuable products. A vanadium catalyst can effectively activate peroxides and selectively oxidize substrates like bromides, sulfides and alkenes are possible. Vanadium catalysts have been shown to effectively transfer oxygen atoms to a substrate that is synthetically useful for obtaining valuable oxidized molecules on a large scale reaction with a high degree of selectivity. Additionally, vanadium catalysts

are efficient catalysts for olefin polymerization. Vanadium oxides can be applied in the emissions standards for vehicles and the desulfurization of crude oil. Moreover, the use of ecological oxidants like hydrogen and alkyl hydroperoxide significantly increases the potential application of vanadium catalysts at an industrial level. Apart from the industrial perspective, the systems containing vanadia are also a rich source of fundamental problems closely related to the theory of catalysis on oxides [81]. Some essential concepts in this domain, like the mechanism of heterogeneous oxidation, were formulated based on vanadia systems.

Impregnation is the most simple and widely used preparation technique for making supported vanadium oxide catalysts. Both wet impregnation and incipient wetness impregnation techniques are usually used for the preparation of vanadia catalysts. The impregnation process is followed by drying and then calcination in air at high temperatures during which the vanadium oxide compound is chemically anchored onto the support oxide surface as shown in **Figure 2.9**.

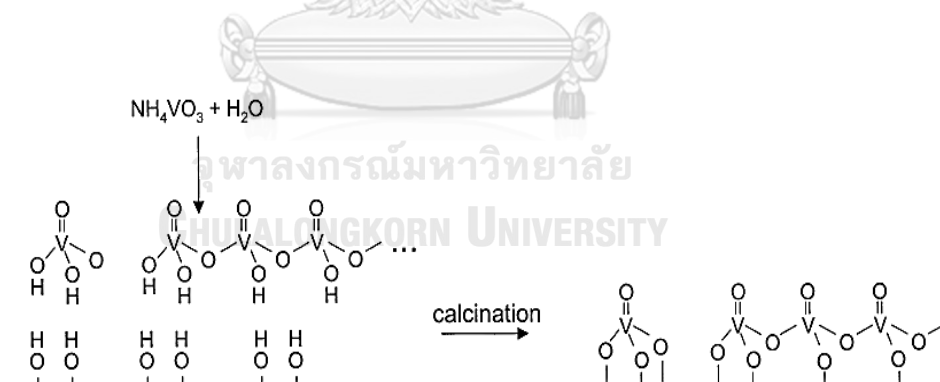


Figure 2.9 Representation of impregnation of a support with an aqueous solution of NH_4VO_3 followed by calcination in air [80].

2.6 Literature Reviews

The most heterogeneous catalysts are solids that react with substrates in a liquid or gaseous reaction mixture. Diverse mechanisms for reactions on surfaces are well known, depending on how the adsorption step takes place. Many industrial catalysts are metals and the simple single crystals provide an introduction to the more atomic metal structures used in industrial catalysts.

This chapter reviewed the works on the catalysts for catalytic dehydration and oxidative dehydrogenation reaction of alcohol that is also of great interest in the field of heterogeneous catalysis while it has been used for many catalytic applications.

2.6.1 Catalysts in dehydration of alcohol

In general, the most crucial factor influencing the catalytic activities for dehydration of ethanol to ethylene appears to be the acidity. Many researchers have investigated to improve and develop the catalyst for many years. Over solid acid catalysts, reaction temperature and contact time play an important role in favoring one or the other dehydration reaction [50].

Guan et al. (2007) [82] reported the application of Fe/SBA-15 catalysts prepared by a direct hydrothermal method for the conversion of ethanol to ethylene. They will show that isolated Fe species embedded in the framework of SBA-15 give this mesoporous material typical Brønsted acidic property, whereas stabilization of small iron oxide clusters confined in the mesopores have weak Lewis acidic and basic functionalities. The isolated Fe^{3+} species in the SBA-15 surface generate Brønsted acidity to dehydrate ethanol to ethylene, with maximum ethylene yields of 63% in the reaction without oxygen and 45% in the reaction with oxygen.

Salas et al. (2009) [83] investigated the surface acidity of the Zr-based mesoporous molecular sieves and found that $\text{SiO}_2/\text{ZrO}_2$ mesocomposites with worm-like pores could be obtained via a surfactant-templated or sol-gel method. The sample with low $\text{SiO}_2/\text{ZrO}_2$ molar ratio presents more Brønsted acid sites. Because the pure mesoporous molecular sieves lacks Brønsted acid sites, therefore, the incorporation of zirconium ions into the framework of the mesoporous molecular sieves is responsible for the formation of these Brønsted acid sites.

Sheng et al. (2011) [84] pointed out that La incorporated SBA-15 material by direct synthesis and post synthesis using two different lanthanum sources. The lanthanum nitrate is a suitable lanthanum source, which can match the hydrolysis rate of silicon precursor and composite materials possess larger specific surface area and uniform mesopore size distribution. The presence of anions in the synthesis mixture of mesoporous material is found to have a remarkable influence on their final structure and, hence, can be an important factor in the design of these materials.

Liu et al. (2014) [33] suggested that the bimetal (Zr and La) incorporated SBA-15 mesoporous materials (ZLS) with a desirable ordered two-dimensional hexagonal structure, which can create new active sites, were synthesized by a direct hydrothermal method under a self-generated acidic condition in the absence of hydrochloric acid. The loading of Zr and La species had negligible effect on the original porous structures of the supports and Zr and La oxide nanoparticles were uniformly dispersed in the supports.

Zhan et al. (2010) [85] studied the effect of catalytic dehydration of ethanol into over HZSM-5, phosphorous modified HZSM-5 and lanthanum-phosphorous modified HZSM-5 in the low temperature range from 473 K to 573 K. The result showed that the addition of lanthanum into the HZSM-5 by wet impregnation, the activity of catalyst increased, but easily deactivated with increase of reaction

temperature. The 2%PHZSM-5 catalyst improved the catalytic performance and anti-coking ability for ethanol dehydration to ethylene at low temperature. The synergistic interaction between the lanthanum and phosphorus, especially for 0.5%La-2%PHZSM-5 which could be regeneration some of the Brønsted acid sites. The TG/DTG analysis confirmed that the introduction of lanthanum into phosphorus modified HZSM-5 restricted the coke formation that could lead to deactivation of catalysts and enhanced the catalysts stability

Nguyen et al. (2015) [86] reported on the use of lanthanum phosphate catalysts for the dehydration of not only ethanol, but also other light alcohols such as 1 and 2-butanol. These catalysts are highly efficient, and have been patented for such dehydration reactions. The experimental results demonstrated the choice of method of preparation has a significant impact on catalytic performance. Although the shape of the particles does not appear to play an important role, their porosity has been shown to influence the catalysts stability. Some of the results obtained in this study confirm those already observed with other dehydration catalysts, namely that pore sizes of 10 nm or more are needed to slow down the deactivation. The $\text{LaPO}_4\text{-M1}$ (Synthesis of a lanthanum gelatinous hydrous oxide slurry and digestion in an aqueous solution of phosphoric acid) and M3 (Precipitation developed for this study) catalysts exhibited the highest catalytic activity for ethanol dehydration, and had comparable selectivities. The other catalysts were markedly less active and selective. Under the chosen catalytic reaction conditions, 100% conversion efficiency was achieved with $\text{LaPO}_4\text{-M1}$ at 460 °C.

Wannaborworn et al. (2015) [87] investigated the catalytic performance for ethanol dehydration over alumina catalysts prepared by solvothermal and sol-gel methods. The results revealed that solvothermal-derived alumina showed the highest catalytic activity among other ones because it has the highest surface area and highest ratio of weak acid sites to strong acid sites. The textural and acidic

properties significantly affect catalytic dehydration.

Cecilia et al. (2015) [88] studied the vanadium and vanadium-phosphorous containing Zr-SBA-15 catalysts prepared by sol-gel followed by incipient wetness impregnation method for dehydration of glycerol to acrolein. The experimental results demonstrated that after the H_3PO_4 treatment, the total acidity increases when small amounts of the acid are employed, but it considerably diminishes for higher contents, which is due to the incorporation of phosphorous into the framework reduces their BET surface area. In addition, the treatment with phosphoric acid increases the Brønsted acid ratio with respect to the catalysts in absence of phosphorous. Although all catalysts are active in the glycerol dehydration and acrolein is the main product for all cases, acrolein yield improves after the treatment with H_3PO_4 in spite of the blockage of the pores, achieving a value of 42% after 2 h of reaction at 325 °C for 12V-P0.2-Zr/SBA-15 catalyst.

Cecilia et al. (2016) [89] investigated the tungsten oxide and tungsten oxide-phosphorous supported on a zirconium doped mesoporous SBA-15 silica prepared by sol-gel followed by incipient wetness impregnation method for dehydration of glycerol to acrolein. It showed that the incorporation of WO_3 to the $\text{SiO}_2/\text{ZrO}_2$ support increases the total acidity and the Brønsted acid sites proportion, improving the stability in glycerol dehydration. So, the 20W catalyst displays the highest glycerol conversion and acrolein yield values (97% and 41% after 2 h, and 90% and 38% after 8 h of TOS, respectively, at 325 °C) which may be related to the existence of WO_3 - ZrO_2 phases on catalyst surface. Although the H_3PO_4 treatment increases the total acidity, when small amounts of acid are utilized, enhancing acrolein yield at the beginning of reaction, the deactivation of 20W- P_y catalysts is much more pronounced due to the important reduction of specific surface area and total acidity, decreasing the number of available acid sites, mainly for 20W-P0.2-Zr/SBA-15 catalyst.

Similarly, other reports have studied WO_3 supported on ZrO_2 [90, 91] and the effect of doping with Si atoms a WO_3/ZrO_2 catalyst and they achieved high values of glycerol conversion and acrolein selectivity. In addition, mixed oxides of tungsten and niobium have been supported over different materials, demonstrating to be active catalysts for this reaction [92, 93].

2.6.2 Catalysts in oxidative dehydrogenation of alcohol

The oxidative dehydrogenation of alcohols to aldehydes and ketones by heterogeneously catalyzed routes still presents a great challenge in the fine chemical industry. Conventionally, the oxidation of alcohols is carried out by metal-based oxidants in stoichiometric amounts. And on the other hand, precious metal-based homogenous or heterogeneous systems, including gold, silver, and palladium have been used as efficient catalysts with molecular oxygen or organic oxidants as the sole oxidants to promote the selective oxidation of alcohols [94]. Hence, the most attractive route concerning large scale industrial application is the heterogeneous catalytic oxidation with molecular oxygen. Application of solid catalysts for the gas-phase oxidation of structurally simple and volatile alcohols has been thoroughly investigated [95].

Forzatti et al. (1997) [96] studied the behavior of vanadia-based catalysts in the oxidation of methanol. The "monolayer-type" oxide-supported vanadia catalysts, the activity in methanol oxidation follows the trend $\text{V}_2\text{O}_5\text{-TiO}_2$ (anatase) > $\text{V}_2\text{O}_5\text{-ZrO}_2$ > $\text{V}_2\text{O}_5\text{-CeO}_2$ > $\text{V}_2\text{O}_5\text{-Al}_2\text{O}_3$ > pure V_2O_5 , but the selectivity to formaldehyde follows nearly the inverse trend. When vanadium oxide is pure or is interacting with oxides of high-oxidation state and poorly electronegative elements, oxygen species are very covalently bonded and, consequently, poorly nucleophilic. This results in catalysts quite selective for formaldehyde. When, on the contrary, vanadium oxide is mixed

with or supported on metals in lower oxidation states with quite ionic VO-M bonds, selectivity to methyl formate can be higher.

Khodakov et al. (1999) [97] investigated the effect of support (Al_2O_3 , SiO_2 , HfO_2 , TiO_2 , and ZrO_2) on the structure and catalytic behavior of VO_x species over a wide range of VO_x surface densities. The results showed that the structure and dispersion of VO_x species depend on their surface density and on their interaction with a given support. Support surfaces predominantly covered with polyvanadate structures or small V_2O_5 clusters containing V-O-V or V=O linkages lead to high oxidative dehydrogenation rates and selectivities. The composition of the support influences the speciation of VO_x species into monovanadates, polyvanadates, and V_2O_5 clusters and thus the catalytic behavior of supported vanadia in oxidative dehydrogenation reactions.

Santacesaria et al. (2004) [98] investigated the oxidative dehydrogenation of ethanol to acetaldehyde on vanadium based catalysts prepared by grafting on titania-silica supports with different procedures. The results showed the grafting technique with high vanadium load, are less active but more selective than the corresponding catalysts prepared by impregnation. An attempt has been made in order to explain the increase of the observed selectivities on the basis of catalysts properties and adopted preparation procedures.

Tesser et al. (2004) [58] studied the oxidative dehydrogenation of ethanol to acetaldehyde prepared by grafting vanadyl triisopropoxide onto a silica support coated with TiO_2 . The kinetic behaviors of the catalysts were studied in the temperature range 100-180 °C, by changing the ethanol residence time, the molar ratio between the reagents, and the vanadium load. The results showed that this catalyst gives rise to high conversion of ethanol to acetaldehyde at very low temperature (130-180 °C), which represents a useful perspective in view of industrial applications. The high dispersion of the catalyst strongly improves the selectivity, and

the activity of vanadium load amount. Acetaldehyde is relatively stable on this catalyst, and this is the reason for the high selectivities observed. Together with acetaldehyde, small amounts of byproducts were obtained, such as acetic acid, acetals, and CO₂.

Guan et al. (2009) [99] reported a range of silica (SiO₂:Al, MCM-41, SBA-16, SBA-15 and SiO₂) supported gold nanoparticle catalysts had been synthesized on various silica supports. The particle size was varied between 1.7 and 15 nm by varying the support and the gold loading procedure. A strong influence of the gold particle size on the non-oxidative dehydrogenation and oxidative dehydrogenation of ethanol is noted. The gold nanoparticles of about 6 nm showed a much higher activity than smaller or larger particles. In the presence of oxygen, the rate for dehydrogenation was much higher and constant up to about 7 nm and then increases for larger particles because of the presence of an adsorbed oxygen species, but the selectivity became lower as combustion starts to contribute. The presence of molecular oxygen lowers the apparent activation energy.

Nakamura et al. (2014) [100] investigated the conversion of alcohols in a gas phase under N₂ flow at 573 K using V₂O₃ and MoO₂ oxides with low valence oxidation states. The experimental results found that the reaction of ethanol that equimolar amounts of ethane and acetaldehyde were formed as the main products over the oxides. Bi-products were small amounts of ethene and C₄ compounds. Reactions of other alcohols (methanol, 1-propanol and 2-propanol) over the V₂O₃ and MoO₂ catalysts also led to the equimolar formation of corresponding alkanes and aldehydes or ketone. The selectivity to ethane and acetaldehyde were almost independent of the reaction temperature in the range of 533–653 K and contact time in the range 0.0014–0.07 g/ml/min. A plausible reaction mechanism for the co-formation of ethane and acetaldehyde from ethanol is a hydrogen transfer reaction

between two ethanol molecules adsorbed on metal–O²⁻–metal sites of V₂O₃ and MoO₂ catalysts surface by formation of six-membered transition states.

Dutov et al. (2016) [101] studied the silver-modified cryptomelane-type crystalline and silica-supported OMS-2 catalysts (Ag/OMS-2 and Ag/OMS-2/SiO₂, respectively) prepared by impregnation, co-precipitation, and consecutive impregnation methods and tested in selective oxidation of ethanol to acetaldehyde. The results showed that co-precipitation provided the introduction of silver ions into the OMS-2 framework, while impregnation and consecutive impregnation resulted in localization of silver species on the external surface of the OMS-2 or silica supports. The modifications of OMS-2 and OMS-2/SiO₂ catalysts by silver were shown to improve the redox properties of the catalysts and increase the ethanol oxidation rate. However, selectivity to acetaldehyde decreased with increased reaction temperature due to intensification of total oxidation on the Ag–MnO_x sites. Interaction of silver species with manganese dioxide improved both the reducing and reoxidation abilities of the samples, resulting in higher activity of the silver-containing catalysts. In case of silica support for the Ag/OMS-2 composites allowed improving the selectivity toward acetaldehyde in an extended temperature range and, therefore, increasing the yield of acetaldehyde in comparison with the crystalline samples.

CHAPTER III

EXPERIMENTAL

This chapter explains about the research methodology including the catalyst preparation, the experimental for ethanol dehydration, non-oxidative dehydrogenation and oxidative dehydrogenation of ethanol and the characterization of catalysts, respectively.

3.1 Catalyst preparation

3.1.1 Chemicals

Table 3.1 The chemicals used in the catalysts preparation.

Chemical	Formula	Supplier
Tetraethyl orthosilicate (TEOS)	$\text{Si}(\text{OC}_2\text{H}_5)_4$	Aldrich
Zirconium (IV) n-propoxide solution	$\text{Zr}(\text{OCH}_2\text{CH}_2\text{CH}_3)_4$	Aldrich
Zirconyl chloride octahydrate	$\text{ZrOCl}_2 \cdot 8\text{H}_2\text{O}$	Merck
Lanthanum (III) nitrate hexahydrate	$\text{La}(\text{NO}_3)_3 \cdot 6\text{H}_2\text{O}$	Aldrich
Vanadyl acetylacetonate	$\text{OV}(\text{C}_5\text{H}_7\text{O}_2)_2$	Aldrich
Pluronic P-123	$(\text{C}_3\text{H}_6\text{O} \cdot \text{C}_2\text{H}_4\text{O})_x$	Aldrich
Hydrochloric acid (37.7%)	HCl	Aldrich
Ethanol (99.99%)	$\text{C}_2\text{H}_5\text{OH}$	Merck
Ultra high purity nitrogen gas (99.99%)	N_2	TIG

3.1.2 Preparation of SBA-15

3.1.2.1 Preparation of SBA-15 by sol-gel method

First, the mesoporous SBA-15 silica was synthesized following the reported procedure by Cecilia et al. [88]. For the incorporation of zirconium containing mesoporous silicas (SBA-15), the structure-directing agent P-123 was dissolved in a 1.7

M hydrochloric acid aqueous solution, under magnetic stirring at 40 °C. Subsequently, TEOS (silica source) and zirconium n-propoxide were added dropwise, with a Si/Zr molar ratio of 5. The final molar composition of the synthesis gel was P-123/SiO₂/ZrO₂/HCl/H₂O = 1/55/11/350/11,100. For bimetallic containing SBA-15, lanthanum (III) nitrate hexahydrate was added into above solution under similar procedure. The molar ratio of P-123/SiO₂/ZrO₂/La(NO₃)₃·6H₂O/HCl/H₂O = 1/55/11/11/350/11,100. The resulting suspension was stirred at 40 °C for 72 h. The obtained sample was recovered by filtration, rinsed with deionized water until the pH of filtrate was constant, dried at 60 °C, and finally calcined in air at 550 °C for 6 h with a heating rate of 1 °C min⁻¹. The SBA-15 catalyst was denoted as SBA-15-SG, where SG indicates the sol-gel-derived method.

3.1.2.2 Preparation of SBA-15 by hydrothermal method

All catalysts obtained by the hydrothermal method were performed according to the procedure of Liu et al. [33]. For the incorporation of zirconium containing SBA-15, 2 g of the structure-directing agent P-123, was dissolved in 100 g of deionized water under vigorous stirring at 35 °C for 2 h. Then, TEOS, zirconyl chloride octahydrate were added into above solution. The molar ratio of P-123/TEOS/H₂O/ZrOCl₂·8H₂O = 0.01/1/170/1. For bimetallic containing SBA-15, lanthanum (III) nitrate hexahydrate was added into above solution under similar procedure. The molar ratio of P-123/TEOS/H₂O/ZrOCl₂·8H₂O/La(NO₃)₃·6H₂O = 0.01/1/170/1/1. The mixed solution was continuously stirred for 20 h. Finally, the gel was transferred into a Teflon-lined autoclave and heated at 100 °C for 24 h. The white product was filtered, the remaining catalyst was rinsed with deionized water and absolute ethanol until the pH become neutral and dried at 60 °C for 24 h. The structure-directing agent was removed from the as-synthesized product through a solvent extraction procedure using HCl/EtOH solution (1 g of sample in 5 mL/ 150

mL) for 24 h. The catalyst was obtained after drying at 105 °C for 24 h. The SBA-15 catalyst was denoted as SBA-15-*HT*, where *HT* indicates the hydrothermal-derived methods.

3.1.2.3 Preparation of modified SBA-15 supported catalysts with vanadium oxide

Vanadium oxide or VO_x species were deposited onto all different SBA-15, Zr/SBA-15 and Zr-La/SBA-15 supports by the incipient wetness impregnation method by adding vanadyl acetylacetonate (C₁₀H₁₄O₅V) ethanolic solutions (nominal vanadium content of 2 wt%). The catalyst samples were dried overnight and calcined in air at 400°C for 4 h (heating rate of 2°C min⁻¹). The vanadium oxides supported on SBA-15 catalysts were denoted as V/SBA-15, V-Zr/SBA-15 and V-Zr-La/SBA-15 followed by SG or HT.

3.2 Catalyst characterization

All catalysts were characterized by several techniques as follows:

3.2.1 X-ray diffraction (XRD)

Low-angle X-ray powder diffraction (XRD) patterns were collected on Bruker AXS Model D8 Discover X-ray diffractometer, using nickel-filtered CuK α as monochromatic X-ray radiation and a VANTEC-1 detector. Diffraction data were recorded at an interval of 0.01671 in the 2 θ range of 0.5° - 10°. The interplanar distance (d_{100}) was obtained by the Bragg's law using the position of the first X-ray diffraction line. High-angle XRD patterns of the catalysts were measured over an angle 2 θ range of 10° - 80° having the resolution of 0.02° and a step time of 0.2 s using Bruker D8 Advance X-ray diffractometer with CuK α radiation ($\lambda = 1.54056 \text{ \AA}$).

3.2.2 N₂ physisorption

The surface area and average pore volume were determined by N₂-physisorption using Micromeritics ChemiSorb 2750 Pulse instrument. Measurement was performed at -196 °C and calculated according to the Brunauer-Emmet-Teller (BET) isotherm equation and a nitrogen molecule cross section of 16.2 Å. The pore size distributions were derived from the desorption profiles of the isotherms using the Barrett-Joyner-Halenda (BJH) method, based on the Kelvin equation [102].

3.2.3 Fourier transform infrared spectroscopy (FTIR)

The IR spectra were recorded using Nicolet 6700 FTIR spectrometer in the range of 400 to 4000 cm⁻¹ to identify specific structural characteristics of the chemical group from the vibration properties.

3.2.4 Raman spectroscopy

Raman spectroscopy were performed on a using a PE IR SPECTRUM ASCII PEDS 1.60 spectrometer with a 244 nm laser with experimental power of 3 W at a step length of 4 cm⁻¹ in the range between 200 and 1400 cm⁻¹.

3.2.5 Ultraviolet-visible spectroscopy (UV-Vis)

The UV-Vis spectra of the samples were collected on a Perkin Elmer Lambda-650. The powder sample was loaded into a quartz cell, and the spectra were collected over the wavelength of 200-600 nm with a step size at 1 nm reference to BaSO₄.

3.2.6 X-ray photoelectron spectroscopy (XPS)

X-ray photoelectron spectroscopy analysis was employed to obtain insights about the chemical state of metal oxide in the catalyst surface. For all elements, there is a characteristic of binding energy associated with each core atomic orbital.

XPS was acquired using the AMICUS spectrometer with AlK_{α} spectrometer (Thermo VG, USA) equipped with an AlK_{α} X-ray radiation (1486.6 eV) at voltage 15kV and current of 12 mA. The pressure in the analysis chamber was less than 10^{-5} Pa. Charge referencing was measured against adventitious carbon (C 1s at 284.8 eV).

3.2.7 Scanning Electron Microscope (SEM) and Energy X-ray Spectroscopy (EDX)

The morphology and elemental distribution of the catalysts were characterized by scanning electron microscope (SEM) equipped with an energy-dispersive X-ray spectroscope (EDX). SEM and EDX were used to investigate the morphology and elemental distribution of catalysts, respectively using Hitachi mode S-3400N. Micrographs were taken at the accelerating voltage of 30 kV and magnification ranging from 1000 to 10,000 and the resolution of 3 nm. The SEM was operated using the secondary scattering electron (SE) mode. The EDX was performed using Apollo X Silicon Drift Detector Series by EDAX. This technique provides the elemental chemical composition of a point or surface region, enabling identification of virtually any element present.

3.2.8 Transmission electron microscopy (TEM) and energy dispersive X-ray spectroscopy (EDX)

TEM images were acquired on a JEOL JEM-1010/2010 operated at 200 kV and equipped with a Gatan CCD camera for image acquisition. Typically, a small amount of catalyst was suspended in ethanol at room temperature, and dispersed with ultrasonic agitation over a carbon copper grid with holey carbon film. For EDX investigations the Apollo X Silicon Drift Detector (SDD) from EDAX was installed with light element performance down to Boron.

3.2.9 Temperature programmed desorption (NH₃-TPD)

The temperature-programmed desorption of ammonia (NH₃-TPD) was carried out to measure the total surface acidity of the catalysts. In this experiment, the catalyst (80 mg) was evacuated with helium at 550 °C, and then ammonia was adsorbed at 100 °C. Finally, the NH₃-TPD was performed by raising the temperature from 150 to 550 °C to desorb ammonia, under a helium flow of 40 mL min⁻¹, with a heating rate of 10 °C min⁻¹. The amount of ammonia in effluent was measured via the thermal conductivity detector (TCD) as a function of temperature [88].

3.2.10 Carbon dioxide temperature-programmed desorption (CO₂-TPD)

CO₂-TPD experiments were performed to determine the surface basicity of various samples using a Thermo Electron Corporation TPDRO 1100 series Catalytic Surfaces Analyzer with a TC detector. First, 0.10 g of the catalyst was pretreated at 500°C with flowing of helium (30 mL min⁻¹) for 1 h. Then, the catalyst was saturated with pure CO₂ at 40 °C for an hour. After saturation, the physisorbed CO₂ was desorbed in a He flow until a constant baseline level was attained. Then, the catalyst was heated from 40 to 500 °C with a heating rate of 10°C/min to desorb CO₂. The amounts of desorbed CO₂ were calculated by separate calibration factors that were obtained during each experiment. The calibration factors were obtained by pulsing 1 ml of the 10% CO₂/He directly to the MS using a 6-port valve. The CO₂ pulse profile was integrated and a calibration factor was calculated, equating areas to moles of CO₂ [103].

3.3 Reaction study in dehydration of ethanol

3.3.1 Chemicals and reagents

Table 3.2 The chemicals and reagents were used in the reaction.

Chemical	Formula	Supplier
Ethanol (99.99%)	C ₂ H ₅ OH	Merck
Ultra high purity nitrogen gas (99.99%)		TIG
High purity grade hydrogen (99.99%)		TIG
Synthetic air (99.99%)		TIG

3.3.2 Reaction test

3.3.2.1 Dehydration of ethanol

Activity and product distribution via gas-phase ethanol dehydration reaction of catalysts were determined using a fixed-bed reactor (I.D. = 7 mm and length = 0.33 m, made from a borosilicate glass tube) A glass reactor was placed into a temperature-programmed tubular furnace. The reaction system is shown in **Figure 3.1**. In the experiment, 0.01 g of packed quartz wool and 0.05 g of catalyst were loaded into the middle zone of reactor tube. Prior to testing, the catalyst was pretreated in nitrogen (50ml/min) at 200 °C for 1 h to remove any moisture on surface of catalyst. The liquid ethanol was vaporized in a flowing of nitrogen by controlled injection with a single syringe pump at a constant flow rate of ethanol 1.45 ml/h [i.e. the weight hourly space velocity (WHSV) = $22.9 \text{ (g}_{\text{ethanol}}\text{g}_{\text{cat-1}} \text{ h}^{-1})$]. The reaction was carried out at temperature ranging from 200 to 400 °C by feeding the vaporized ethanol into the reactor. The products were analyzed by a Shimadzu GC8A gas chromatograph with flame ionization detector (FID) using capillary column (DB-5) at 150 °C. To ensure the analysis of products, prior to the measurement, the calibration of GC was performed by calibrating the GC-FID with certified pure gas of

ethanol, ethylene, diethyl ether and acetaldehyde of the desired concentrations using an internal standard technique. Duplicate injections of each standard were made and the average value was used for the calibration graph of each reactant and products (**Appendix C**). Then, the ethanol conversion and the selectivity of ethylene, diethyl ether and acetaldehyde were calculated.

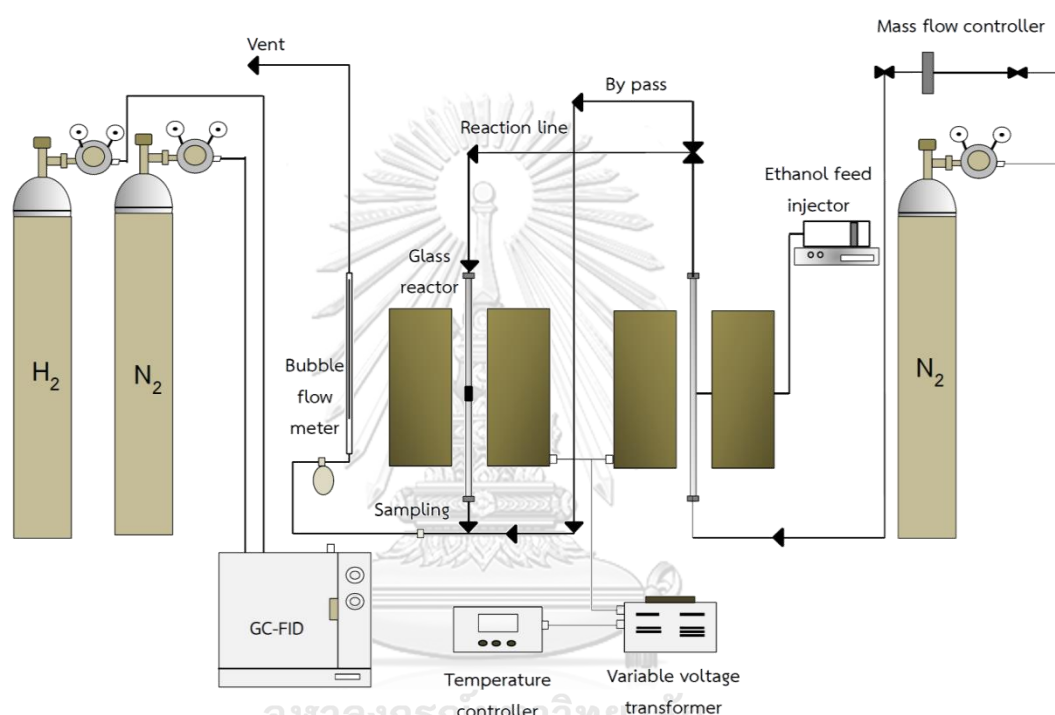


Figure 3.1 Flow diagram of ethanol dehydration systems.

3.3.2.2 Non-oxidative dehydrogenation and oxidative dehydrogenation of ethanol

The catalytic non-oxidative dehydrogenation of ethanol was carried out in a fixed-bed continuous down flow microreactor. The reaction temperature was measured with an interior placed thermocouple in direct contact with the catalyst bed. Typically, 0.05 g of catalyst was used. Prior to testing, the catalyst was pre-treated in nitrogen at 200°C (50 mL/min) for 1 h. The liquid ethanol was fed into the

vaporizer and ethanol flow rate was controlled by a single syringe pump at 1.45 ml/h [i.e. the weight hourly space velocity (WHSV) = $22.9 \text{ (g}_{\text{ethanol}}\text{g}_{\text{cat-1}} \text{ h}^{-1})$]. Catalytic reactions were performed at atmospheric pressure in the temperature range from 150 to 400°C.

For oxidative dehydrogenation reaction, the feed mixture consisted of ethanol/oxygen molar ratio of 2/1. Before introducing ethanol to react with catalysts in the reactor, oxygen (air) is required. So, the flow rate of N₂ carrier gas was decreased to 17.8 ml/min and air was introduced at the flow rate of 46 ml/min. Oxidative dehydrogenation of ethanol was performed at the temperature range between 150 to 400°C and atmospheric pressure. The product gas samples were analyzed by gas chromatograph (GC-FID and GC-TCD detector). The reaction test is shown in **Figure 3.2**. Conversion of ethanol and product selectivities were expressed as mol% on a carbon atom basis.

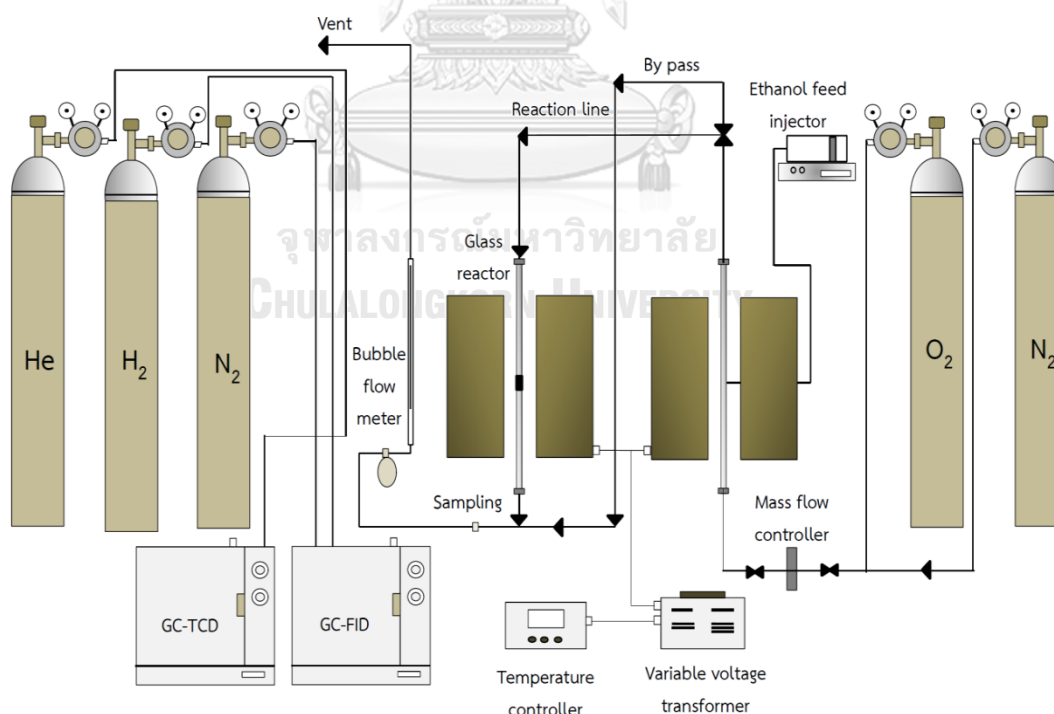


Figure 3.2 Flow diagram of oxidative dehydrogenation systems.

- 1.) Reactor: The reactor tube is made from glass tube (borosilicate type) with an inner diameter 7 mm and length = 0.33 m.
- 2.) Furnace and heating cable: The furnace is provided heat for the reactor. The temperature of the furnace is controlled by interoperability of variable voltage transformer and temperature controller. For heating cable, it is warped with the line at outlet of reactor. The heating cable is used to prevent the condensation of water dehydrated from reaction.
- 3.) Temperature controller: The temperature of furnace is established a set point at any temperatures in range between 200 °C to 400 °C by temperature controller which is connected to thermocouple attached to the reactor and a variable voltage transformer.
- 4.) Gas controlling system: Nitrogen is used to carrier ethanol vapor into the system. It is set with a pressure regulator, an on-off valve and mass flow controller are used to adjust the flow rate of carrier gas.
- 5.) Gas chromatography (GC): A Gas chromatography equipped (Shimadzu GC-14A) with flame ionization detector (FID) with DB-5 capillary column, which is used for separation of light hydrocarbon such as ethanol (C_2H_5OH), acetaldehyde (C_2H_4O), diethy ether ($C_2H_5O C_2H_5$), etc. A Shimadzu GC-8A (Molecular sieve 5A and Parapak Q) gas chromatography equipped with a thermal conductivity detector (TDC) is used for separation of carbon monoxide (CO), carbon dioxide (CO_2) and oxygen (O_2) in the feed and product streams. The operating conditions for each instrument are shown in the **Table 3.3**.

Table 3.3 Operating conditions for gas chromatograph

Gas chromatograph	SHIMADZU		SHIMADZU
	GC-8A		GC-14B
Detector	TCD	TCD	FID
Column	Molecular sieve	Parapak Q	DB5
Maximum temperature	5A	150 °C	350 °C
Carrier gas	350 °C	He (99.999%)	N ₂ (99.999%)
Carrier gas flow	He (99.999%)		
Column temperature	40 cc/min		
- Initial (°C)		80	40
- Final (°C)	80	80	40
Injector temperature (°C)	80	100	150
Detector temperature (°C)	100	-	150
Current (mA)	-	80	-
Analyzed gas	80 CO, O ₂ , N ₂	CO ₂ , C ₂ H ₄ , CH ₄	Ethanol, ethylene, acetaldehyde, diethyl ether

CHAPTER IV

RESULTS AND DISCUSSIONS

This chapter was aimed to investigate the effects of metal oxide (V, Zr and La) on SBA-15 catalysts obtained by sol-gel and hydrothermal methods for catalytic dehydration, non-oxidative dehydrogenation and oxidative dehydrogenation of ethanol to high-value added chemical products such as ethylene and acetaldehyde. The topic was divided into three sections. The first section illustrated the preparation and characterization of SBA-15, Zr/SBA-15 and bimetal zirconium and lanthanum (Zr and La) prepared by sol-gel and hydrothermal methods. The second section showed characteristics and catalytic activity of SBA-15 catalysts synthesized by sol-gel and hydrothermal methods through ethanol dehydration reaction. Later, the effect of different VO_x /SBA-15 catalysts for non-oxidative dehydrogenation and oxidative dehydrogenation of ethanol were discussed in third section.

4.1 Characteristics of SBA-15, Zr/SBA-15 and bimetallic Zr-La/SBA-15 prepared by sol-gel and hydrothermal methods

4.1.1 X-ray diffraction pattern (XRD)

X-ray diffraction was used to identify crystalline phases present in these catalysts. The XRD patterns at low-angle of all catalysts obtained by the sol-gel method are shown in **Figure 4.1**. The successful formation of well-ordered mesoporous silicas with two-dimensional hexagonal structure is confirmed by the presence of a basal (100) peak along with (110) and (200) reflections in the low-angle region after calcination of sample. Furthermore, we can note that, in the case after zirconium oxide loading, a shift of the XRD peaks toward high-angle region is evident

indicating an increase in the unit cell parameter [84]. The expansion of unit cell parameter may indicate the successful incorporation of metal oxide in the framework. Similar results were previously observed [104]. However, in case of Zr-La/SBA-15-SG catalyst, the intensity of the diffraction peaks (100), (110) and (200) decreased or disappeared. This is probably due to the incorporation of bimetallic or heteroatoms into the framework of SBA-15 causes a slight collapse of the hexagonal structure [105]. With regard to the XRD patterns in the high-angle region (**Figure 4.2**), only wide diffraction peaks of characteristic of amorphous SiO₂ were observed with 2θ around 21-25° (broad) [106]. However, no any diffraction peak of metal oxide crystalline phases can be observed due to metal oxide has no aggregates on the surface of the catalysts. The catalysts prepared by hydrothermal method, as can be seen in **Figure 4.3**, exhibit stronger peaks. The relative intensity of the (110) and (200) reflections disappear with compared to those prepared by sol-gel method. This may be due to extensive washing in the last step strongly reduces order of the pores. A possible explanation for this behavior could be that the template has a higher solubility in ethanol than in water, thus, ethanol leads to more efficient removal of the template as described by Ko and Bae [26, 107]. Besides, during extensive washing, the formation of blocked pores cannot be ruled out, which would offer a straightforward explanation for the significant reduction in surface area as well as the long range order in XRD [108]. This is in agreement with previous reports to claimed that the well-ordered pore structure (100) was retained, but the intensity of the diffraction peaks (200) decreased probably due to destruction of the ordered structure [109, 110]. For Zr/SBA-15-HT and Zr-La/SBA-15-HT, the characteristic of diffraction peak is attenuated and slight change in the intensity with a pore system lacking long-range order when catalysts are incorporated with Zr and bimetallic Zr-La, pointing out the collapse of the mesostructure of the SBA-15, which is similar to those of mesoporous SBA-15 silica synthesized with phosphoric acid [111] and

cationic surfactant in presence of organic salts [112]. **Figure 4.4** shows the high-angle XRD patterns of all catalysts. The XRD pattern of SBA-15 prepared by hydrothermal method was broad (amorphous SiO_2) because the sizes were very small. The result was similar as seen in **Figure 4.2**. Because there are no noticeable high-angle XRD patterns of these mesoporous silica materials, the pore walls are concluded to be amorphous in nature [113]. Thus, nitrogen sorption and XRD demonstrate that both sol-gel and hydrothermal methods have typical SBA-15 structures.

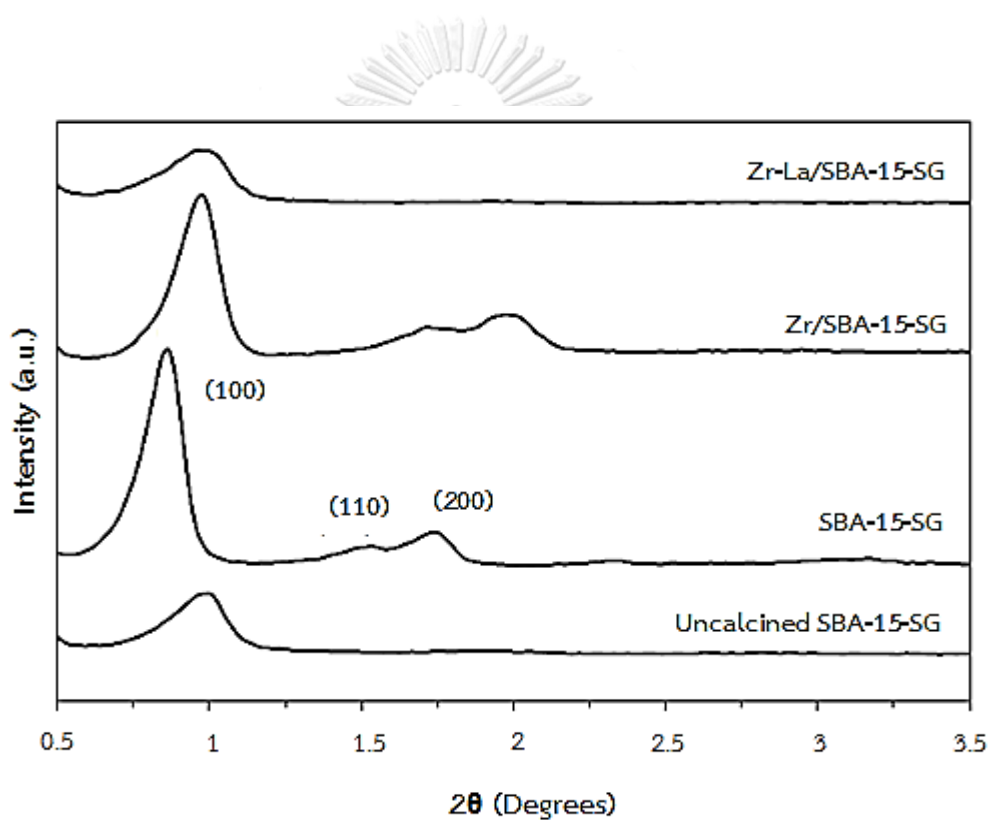


Figure 4.1 XRD patterns of all catalysts obtained from the sol-gel method at low-angle regions.

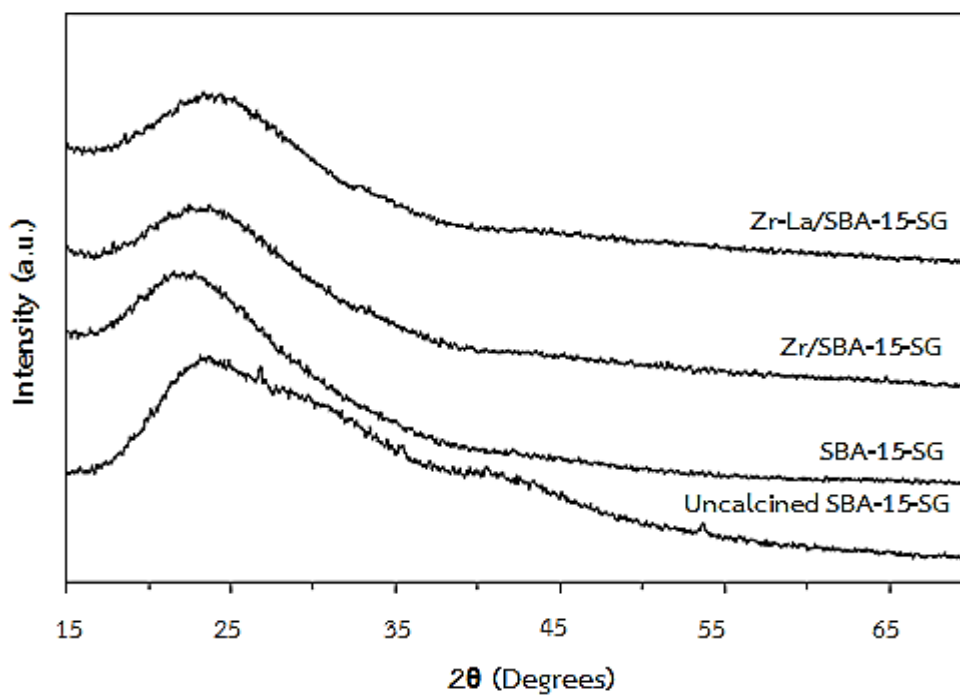


Figure 4.2 XRD patterns of all catalysts obtained from the sol-gel method at high-angle regions.

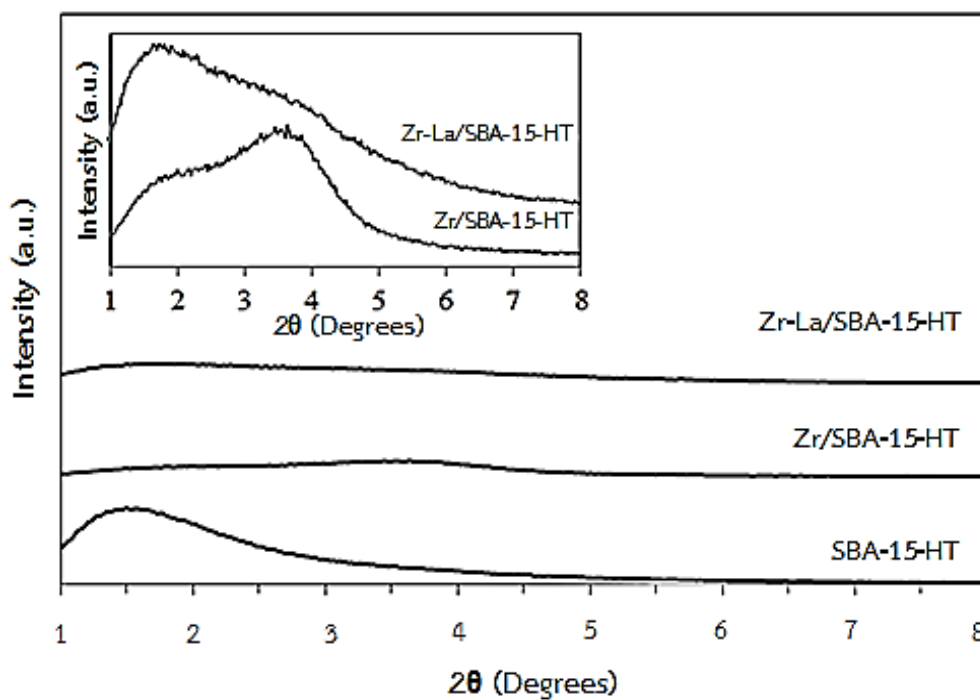


Figure 4.3 XRD patterns of all catalysts obtained from the hydrothermal method at low-angle regions.

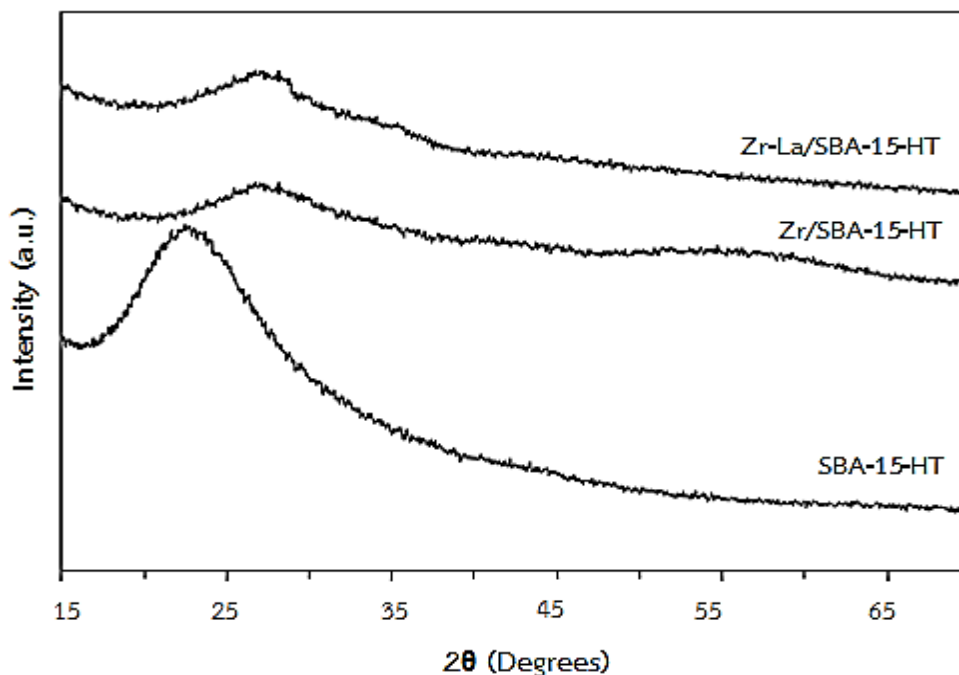


Figure 4.4 XRD patterns of all catalysts obtained from the hydrothermal method at high-angle regions.

4.1.2 N₂ physisorption

Figure 4.5-4.6 shows the nitrogen adsorption/desorption isotherms of SBA-15 catalysts prepared by sol-gel (a) and hydrothermal method (b). All catalysts exhibited type IV adsorption isotherms with a H1 hysteresis loop as defined by IUPAC classification, indicating that they are mesoporous materials. The isotherms for sol-gel method catalysts showed quite different pattern. Two inflection points and hysteresis loop moved toward lower pressure ($P/P_0 = 0.3$ to 0.7). Meanwhile, the isotherms for hydrothermal method catalysts, they presented hysteresis loop of type H1, occurring at higher relative pressure ($P/P_0 = 0.7$ to 0.9) corresponding to the capillary condensation of nitrogen. It indicates larger mesoporosity character of SBA-15, confirming that metal oxide can be located into the hexagonal framework of SBA-

15 and the mesoporous channels still remain. The textural properties of the catalysts are summarized in **Table 4.1**, in which the pore volume of SBA-15-SG, Zr/SBA-15-SG, and Zr-La/SBA-15-SG was 0.69, 0.70, and 0.72 cm³/g, respectively. The incorporation of Zr and bimetallic Zr-La into SBA-15 increases the surface area due to the Zr and La were located on the external surfaces suggesting that metal oxide were not incorporated into the channels of SBA-15 or found on the external surfaces, leading to an increase in surface area. Moreover, even when some of the pores are blocked, it suggests that the Zr and La prepared by sol-gel method were still well dispersed in the SBA-15. The result was confirmed by the high-angle diffraction peak of XRD as shown in **Figure 4.2**. This effect has also been observed for mesoporous Al-SSP doped with Mo [114]. For SBA-15 catalysts prepared by hydrothermal method, the pore volume of catalysts was higher than the sol-gel method. The incorporation of Zr and bimetallic Zr-La into SBA-15 decreases the surface area, mainly due to the blockage of the mesoporous framework. This is probably due to for catalysts synthesized by hydrothermal method, agglomeration of primary particles altered the porous shape [87], resulting in metal oxide easily incorporated into the channels of SBA-15.

The pore size distribution (PSD) calculated by BJH method is shown in **Figure 4.7-4.8**. All catalysts prepared by sol-gel method, they have a narrow pore size distribution with an average pore diameter around 3.4 - 4.5 nm, confirming that the pore size distribution is in the mesoporous range. For the catalysts prepared by hydrothermal method, the distribution was broad and diameter was large. The pore diameter decreased from 11.2 to 5.3 nm as the incorporation of Zr and bimetallic Zr-La into SBA-15. It can be seen that the calculated pore size distribution was in good agreement with N₂ adsorption/desorption isotherms as mentioned above.

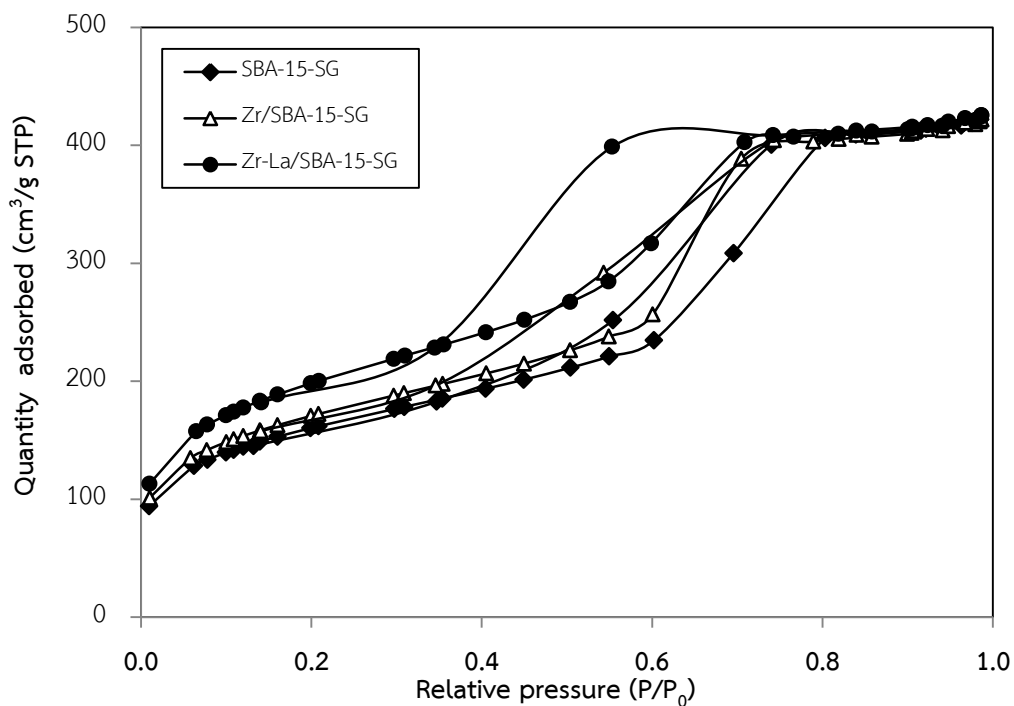


Figure 4.5 Nitrogen adsorption/desorption isotherms of all catalysts synthesized by sol-gel method.

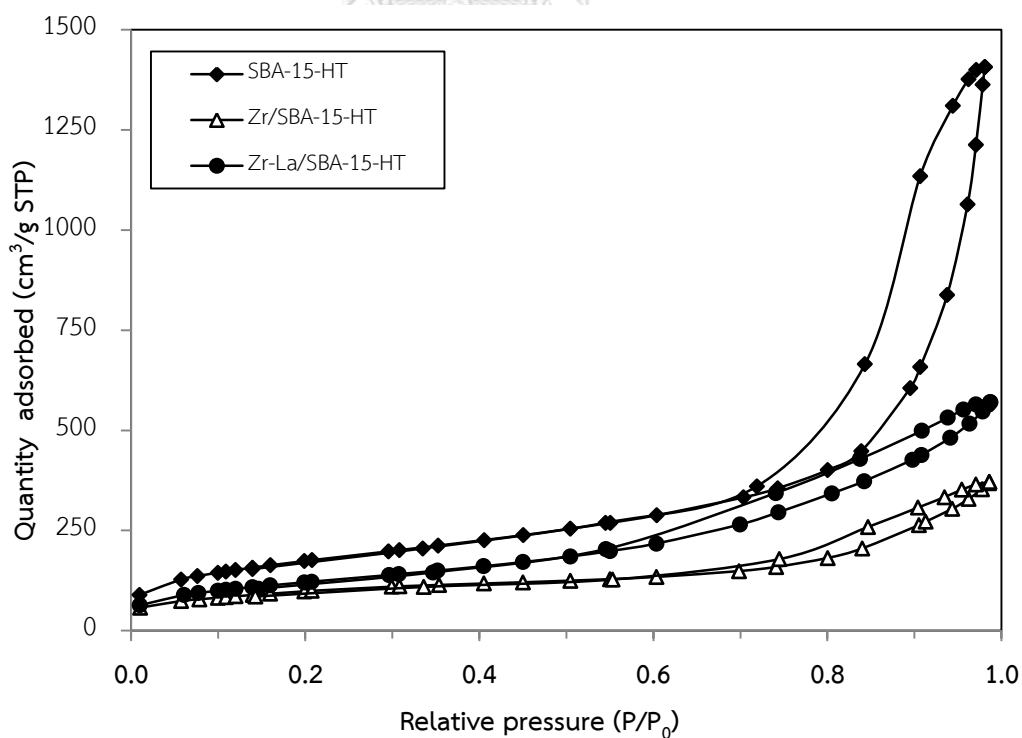


Figure 4.6 Nitrogen adsorption/desorption isotherms of all catalysts synthesized by hydrothermal method.

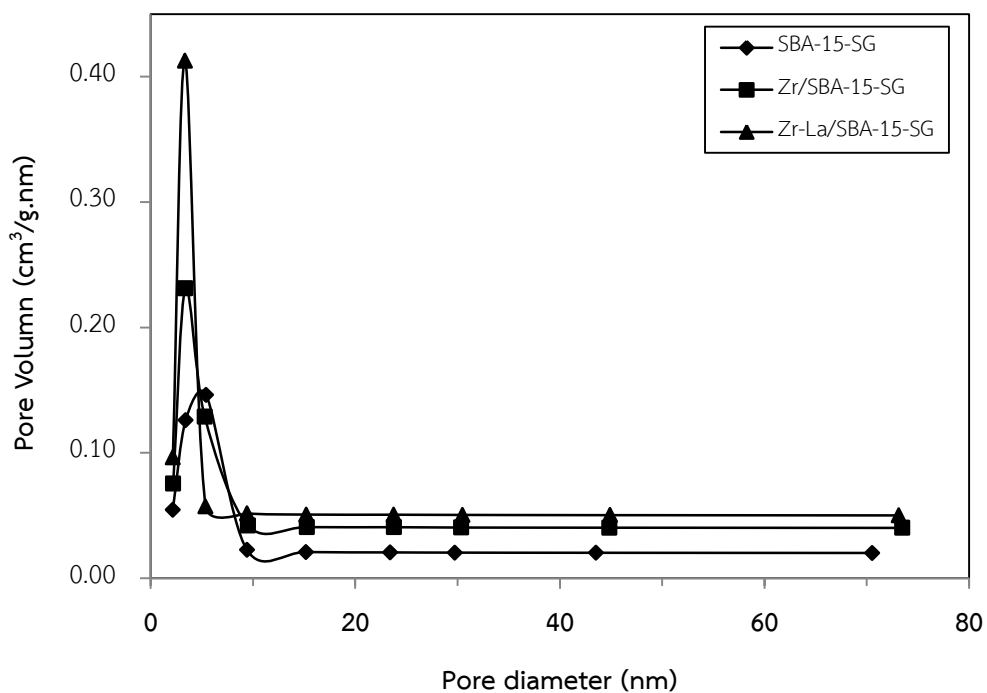


Figure 4.7 BJH pore size distribution of all catalysts obtained by sol-gel method.

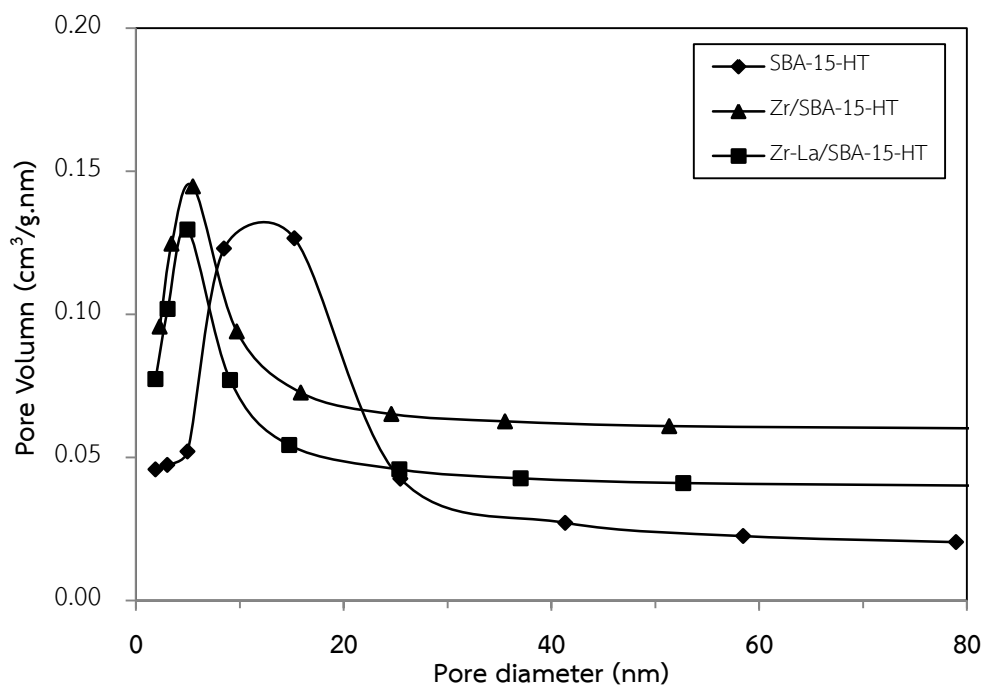


Figure 4.8 BJH pore size distribution of all catalysts obtained by hydrothermal method.

Table 4.1 Textural properties of the catalysts.

Catalysts	Surface area (m ² /g)	Average pore diameter (nm.)	Average pore volume (cm ³ /g)
SBA-15-SG	574.1	4.5	0.69
Zr/SBA-15-SG	611.2	4.1	0.70
Zr-La/SBA-15-SG	713.6	3.4	0.72
SBA-15-HT	638.3	11.2	2.20
Zr/SBA-15-HT	462.1	5.3	0.90
Zr-La/SBA-15-HT	445.1	6.0	0.89

4.1.3 Fourier transform infrared spectroscopy (FT-IR)

In order to further confirm the incorporation of zirconium and bimetallic zirconium-lanthanum ion into the framework, the catalysts prepared by sol-gel and hydrothermal methods were characterized with FTIR technique. The fundamental vibrations of the Zr–O–Si, Zr–La–O–Si and Si–O–Si bonds in the framework can be seen below 1,300 cm⁻¹. The bands at 808 and 1,054 cm⁻¹ are assigned to the bending (or symmetric stretching), and asymmetric stretching of the intertetrahedral oxygen atoms in SiO₂ of SBA-15, respectively [83]. As shown in **Figure 4.9**, the SBA-15 catalysts show absorption band at 3,398-3,412 cm⁻¹ assigned to the stretching vibration of OH groups for physisorbed water molecules on SBA-15 surface [115]. The OH bond vibrations due to the presence of the silanol group also show a peak at the same wavenumber. An OH deformation vibration was observed near 1,630 cm⁻¹ [116]. The absence of C–H vibrations at 2,850-3,000 cm⁻¹ indicates the efficient removal of the surfactant [117]. The FTIR studies of SBA-15 catalysts synthesized by sol-gel and hydrothermal methods confirm that there was no change in functional group after the incorporation of Zr and bimetallic Zr-La into SBA-15. For Zr/SBA-15-HT catalyst

(Figure 4.10), this band shifts toward the lower wavenumber at 872 cm^{-1} . The shift of this absorption band toward the lower wavenumber is considered as an indication of metal incorporating into the framework of silica tetrahedral [118, 119]. Therefore, it indicates that the small particle size of Zr by hydrothermal may be partly incorporated into the framework of SBA-15 excepting for the Zr-La/SBA-15-HT. The intensity of the bands around $1,624\text{ cm}^{-1}$ could be assigned to CH stretching vibration and asymmetric stretching vibration of the NCOO^- skeletal vibration with La addition, indicating that bimetallic Zr and La have been successfully grafted onto the wall of SBA-15 [119, 120] corresponding to the low and high angle XRD results.

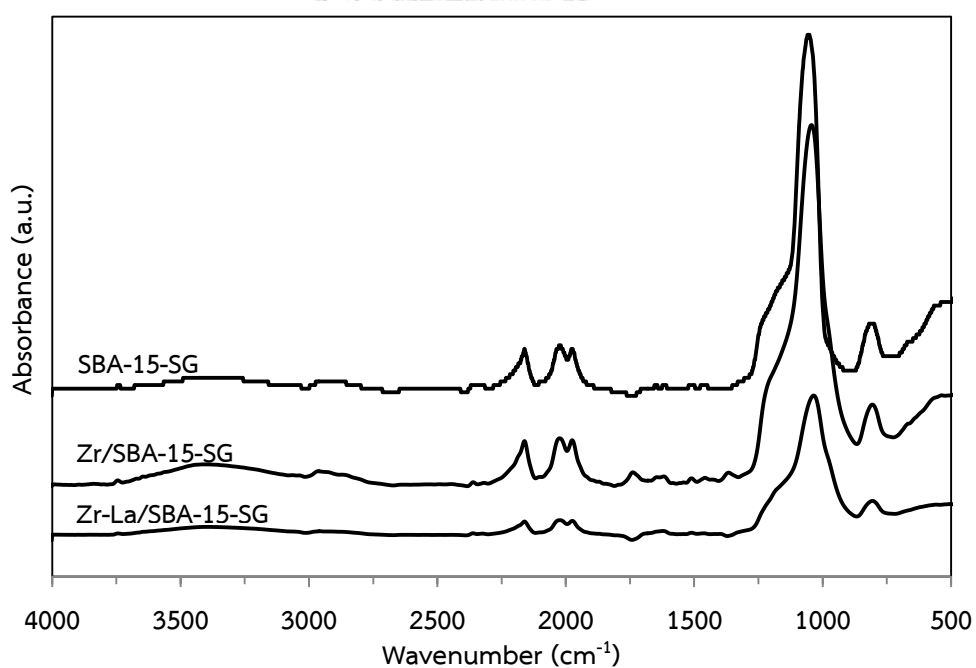


Figure 4.9 FTIR spectra of all catalysts obtained by sol-gel method.

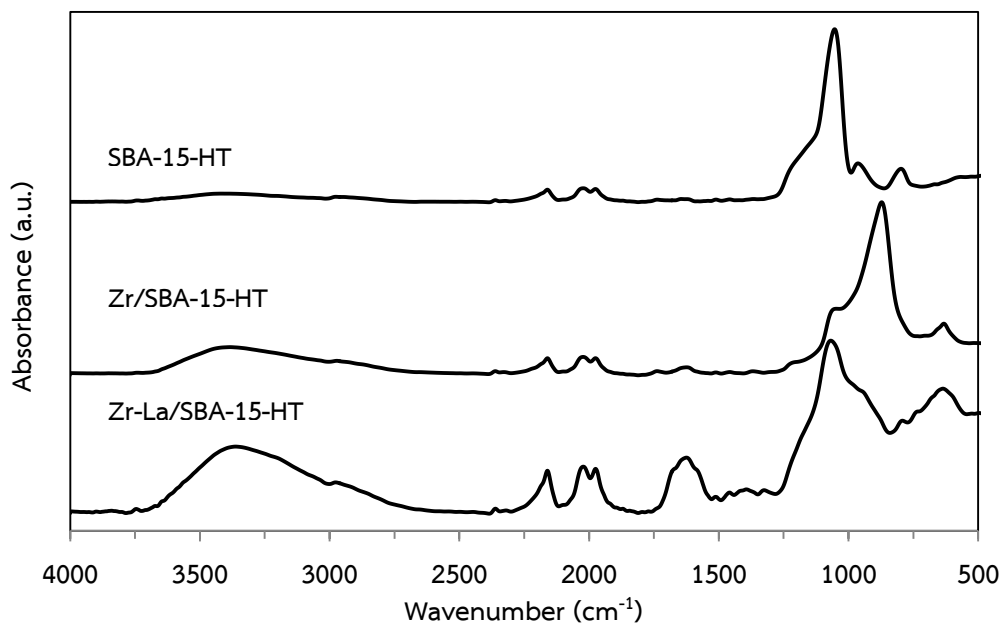


Figure 4.10 FTIR spectra of all catalysts obtained by hydrothermal method.

4.1.4 Raman spectroscopy

The Raman spectra of SBA-15 resemble those of published visible Raman spectra. As shown in **Figure 4.11**, the D1 and D2 bands at 248 and 386 cm^{-1} are assigned to symmetric O–Si–O motions of vibrationally isolated four-membered rings of SiO_4 tetrahedral and to breathing motions of three-membered rings of SiO_4 tetrahedral, respectively [121]. The combined feature at around 800 and 830 cm^{-1} is assigned to the transverse (TO) and longitudinal (LO) optical components of siloxane bridges network motions, respectively. In addition, the band at 976 cm^{-1} is assigned to the Si–OH stretching of free surface silanols [122]. For zirconium incorporated on SBA-15, no new peaks were observed indicating the monolayer coverage with no crystalline phase of zirconia species on the SBA-15. However, for Zr-La/SBA-15-SG catalyst, the intensity of the peaks corresponding to SBA-15 decreases dramatically

due to the metal oxide found on the external surfaces, as supported by the textural properties results in **Table 4.1**. For catalysts prepared by hydrothermal method (**Figure 4.12**), the main Raman bands of tri-cyclosiloxane rings, siloxane bridges, and surface silanol groups were still remained, indicating that the metal oxide incorporated into the channels of SBA-15. For SBA-15-HT showing a weak band, this is identified as the D1 band of cyclic tetrasiloxane rings. Similar SBA-15 peaks were reported by Chamack et al. [104]. The Raman band at 911 cm^{-1} for the Zr/SBA-15-HT catalyst is assigned to the Si–O–Zr linkages, indicating that some Zr species interact with Si–OH to form Si–O–Zr bond [123]. According to the report [124], the bands at 755 and $1,087\text{ cm}^{-1}$ may correspond to the intermediate phase of zirconia, and no Raman bands of tetragonal zirconia, monoclinic zirconia and zircon were observed. The results demonstrate that some Zr species on SBA-15 are amorphous zirconia, and are probably present as highly dispersed surface species [125]. For the Raman spectrum of Zr-La/SBA-15-HT, the band at 839 cm^{-1} is attributed to the perturbed silica vibrations for $\text{Si}(\text{O}^-)_x$ functionalities, suggesting the formation of La–O–Si bond. The band at $\sim 562\text{ cm}^{-1}$ is attributed to the lanthanum oxide overlaps with the Raman band of tri-cyclosiloxane rings [125]. Regarding the Raman characterization technique, it can be found that the metal oxide species can lead to partially M–OH species combine with Si–OH groups to form Si–O–M bond, which is in agreement with the results of FTIR spectroscopy.

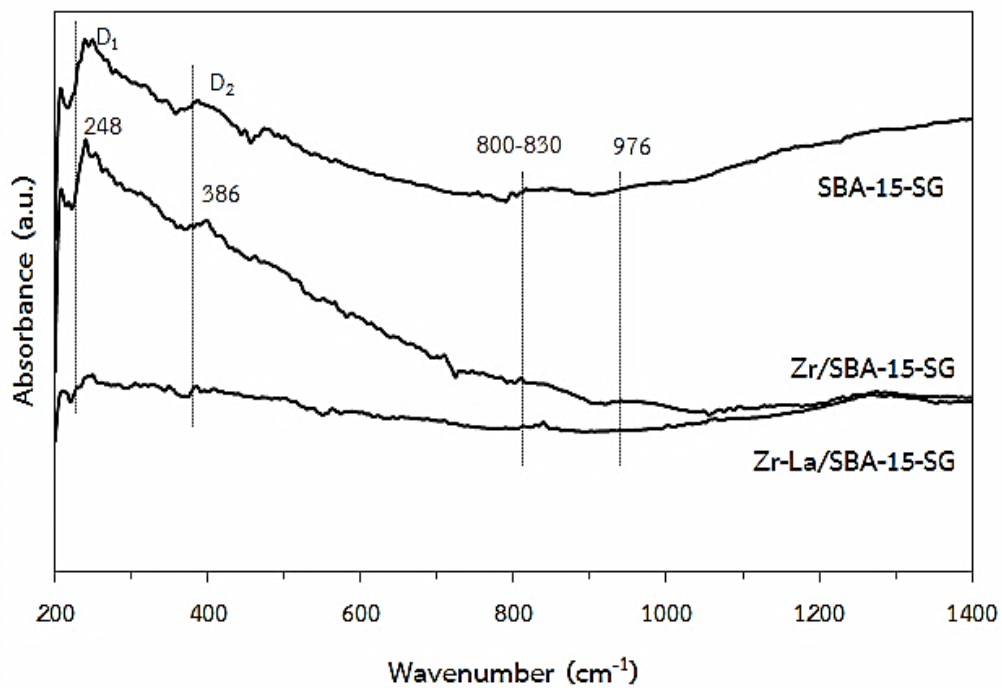


Figure 4.11 Raman spectra of all catalysts obtained by sol-gel method.

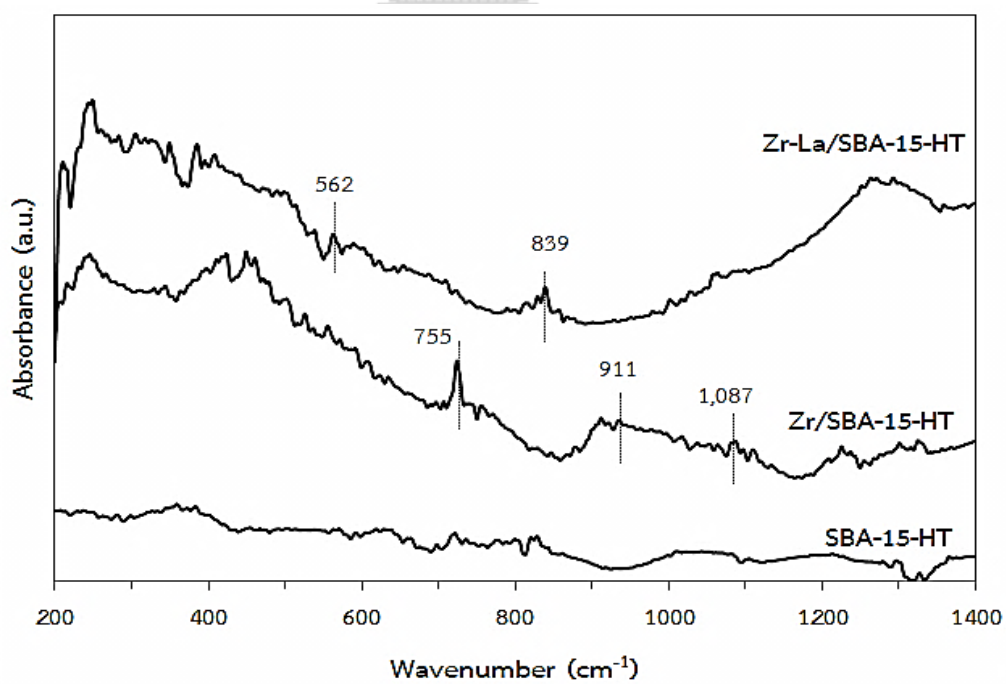


Figure 4.12 Raman spectra of all catalysts obtained by hydrothermal method.

4.1.5 UV-visible spectroscopy (UV-vis)

Diffuse reflectance spectroscopy is a well-known method to detect the framework and extraframework of the transition metal ions. **Figure 4.13-4.14** shows the UV-Vis absorption spectra of SBA-15 catalysts prepared by sol-gel and hydrothermal methods. No absorption band was observed on SBA-15 for both methods because SiO_2 is transparent in the test UV region [126, 127]. For Zr/SBA-15-SG, the absorption band was found to be around 230-248 nm. This is the characteristic of the ligand-to-metal charge transfer (LMCT) from O^{2-} to Zr^{4+} with an octahedral coordination state [128]. In the case of Zr-La/SBA-15-SG, a very sharp absorption band was detected at 250-260 nm for the mechanical mixture of SBA-15 and metal oxide, which is assigned to the electronic transition from 5d orbit to 4f orbit of La^{3+} species. This is not affected by the coordination of La^{3+} in the Zr-La/SBA-15-SG framework [118]. The emergence of absorption band shifts toward at 270 nm higher than previous report [83], which is owing to the presence of La^{3+} species in the tetracoordinated of SBA-15 framework. In contrast to SBA-15 catalysts prepared by hydrothermal method, it displayed distinct absorbance in the UV range. The absorbance intensity increased with incorporation of Zr and bimetallic Zr-La into SBA-15. In addition, previous studies also suggested that substantial blue shift in absorbance was observed on the incorporation of Zr and bimetallic Zr-La catalysts as compared with pure metal oxide [105].

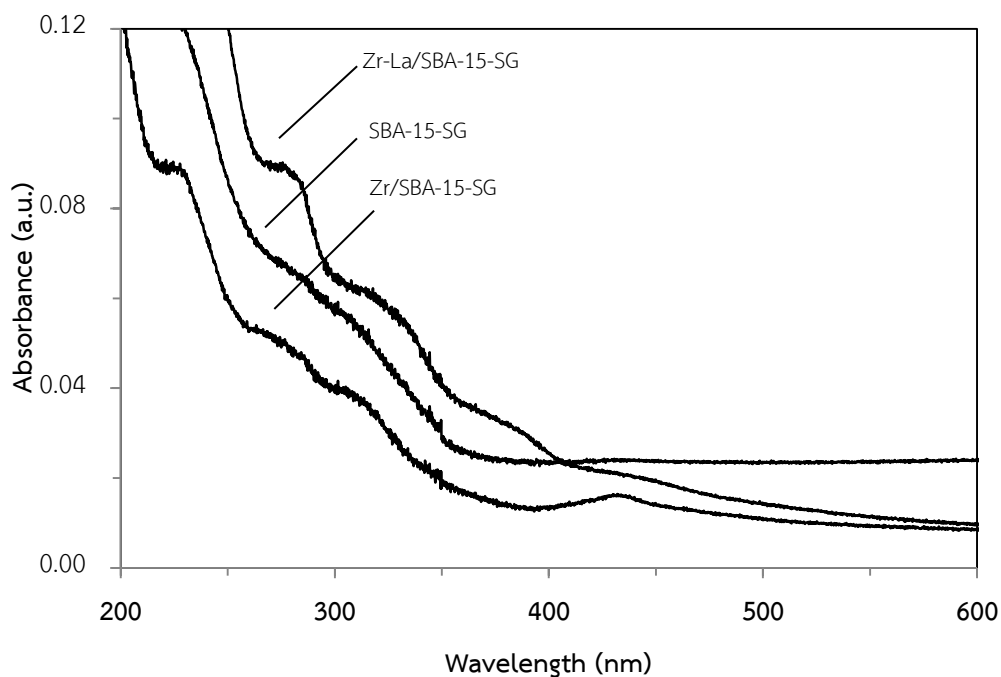


Figure 4.13 UV-Vis diffuse reflectance spectra of all catalysts obtained by sol-gel method.

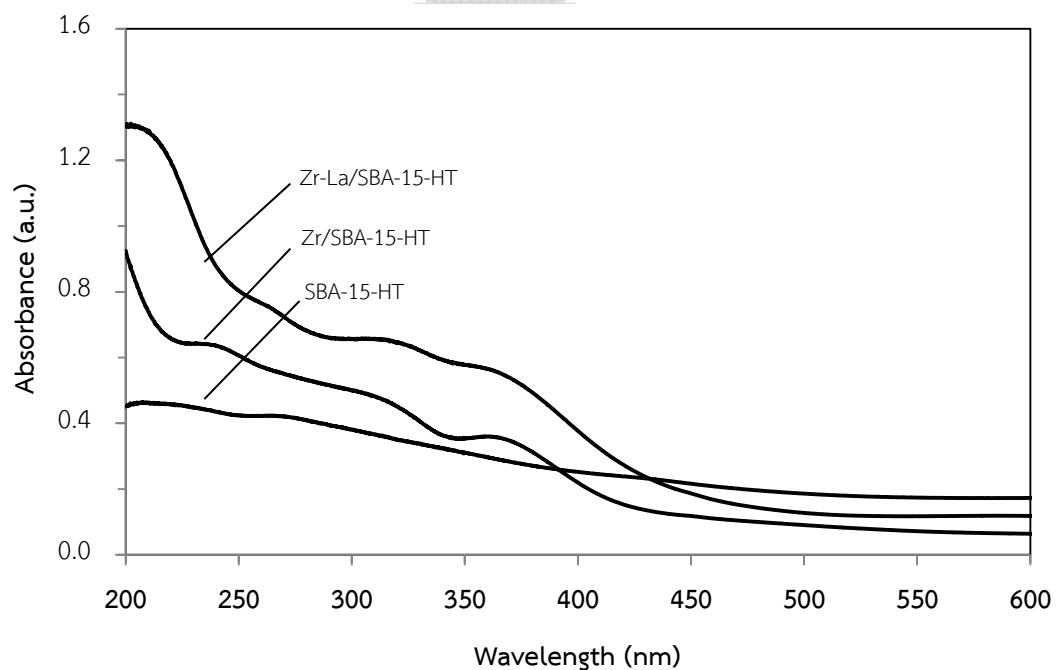


Figure 4.14 UV-Vis diffuse reflectance spectra of all catalysts obtained by hydrothermal method.

4.1.6 Scanning electron microscope and energy dispersive X-ray spectroscopy (SEM/EDX)

To examine the catalyst morphology, SEM technique was performed. The SEM micrographs of different catalysts are shown in **Figure 4.15**. The structure of SBA-15 synthesized by sol-gel method is fiber-like or elongated silica fibers with the hexagonal prismatic morphology of the particles, formed by aggregates of fibers or rods connected into ropelike macrostructures. Similar SEM images were reported by Kosuge et al. [129]. The long fibers are obtained using stirring, while the rod like particles of SBA-15 can be obtained in the absence of stirring. After incorporated the SBA-15 with Zr and bimetallic Zr-La, it can be seen that there was no significant change in the morphology of catalysts. For those catalysts synthesized by hydrothermal method, the particles of SBA-15 show worm-like morphology and aggregate together, which is similar to an earlier report [130]. After incorporated with Zr and bimetallic Zr-La, it shows spherical particles together with some small irregular shape particles, indicating poor long-range ordered structures [131].

The dispersive X-ray spectroscopy (EDX) was also performed to determine the elemental distribution in the SBA-15 catalysts prepared by sol-gel and hydrothermal methods. All elements in the catalysts such as Si, O, Zr and La can be detected using the EDX mapping mode. The typical EDX mapping of Zr-La/SBA-15-SG and Zr-La/SBA-15-HT catalysts is shown in **Figure 4.16(a)-(b)**. In this figure, the distribution of Si, Zr and La was observed. The density of Si was strongly observed because Si is the main components of SBA-15 catalysts. After incorporated with Zr and bimetallic Zr-La, the well distribution of metal oxide was evident. For Zr-La/SBA-15-HT catalyst, agglomeration of metal oxide particles was found mostly on outer surface. This result is in accordance with that obtained from XRD.

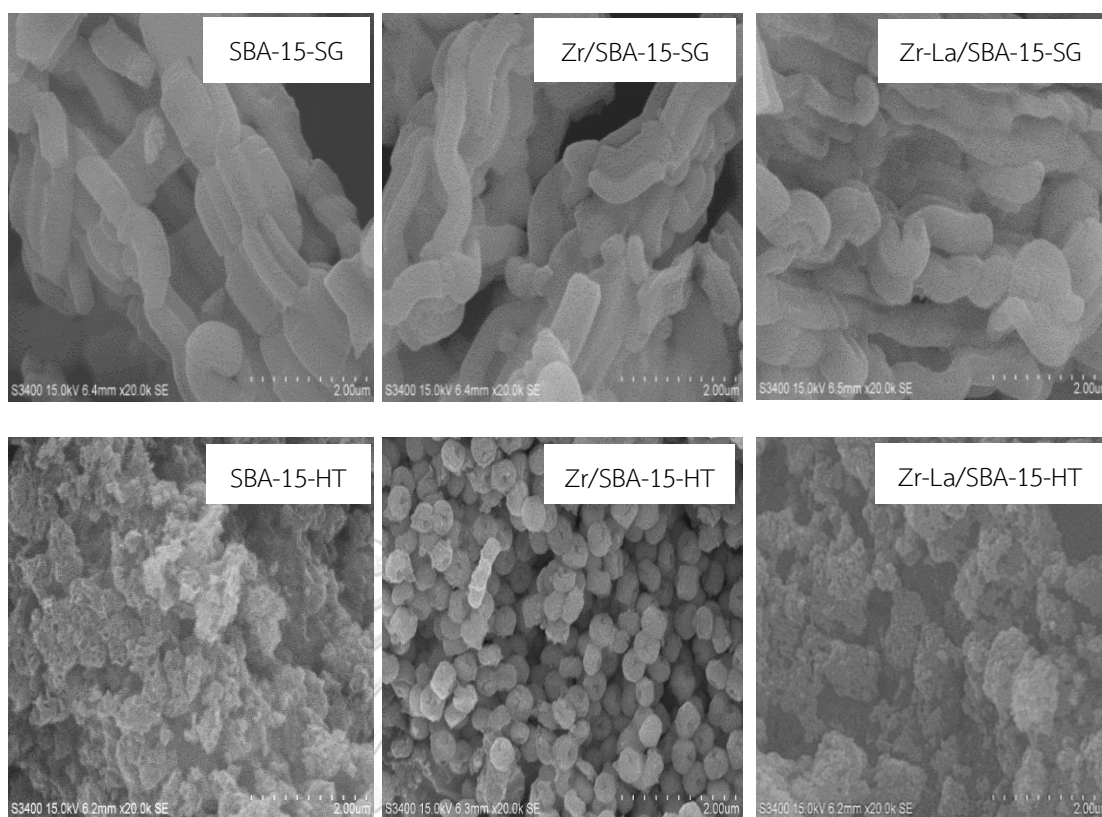


Figure 4.15 SEM images of all catalysts obtained by sol-gel and hydrothermal methods.

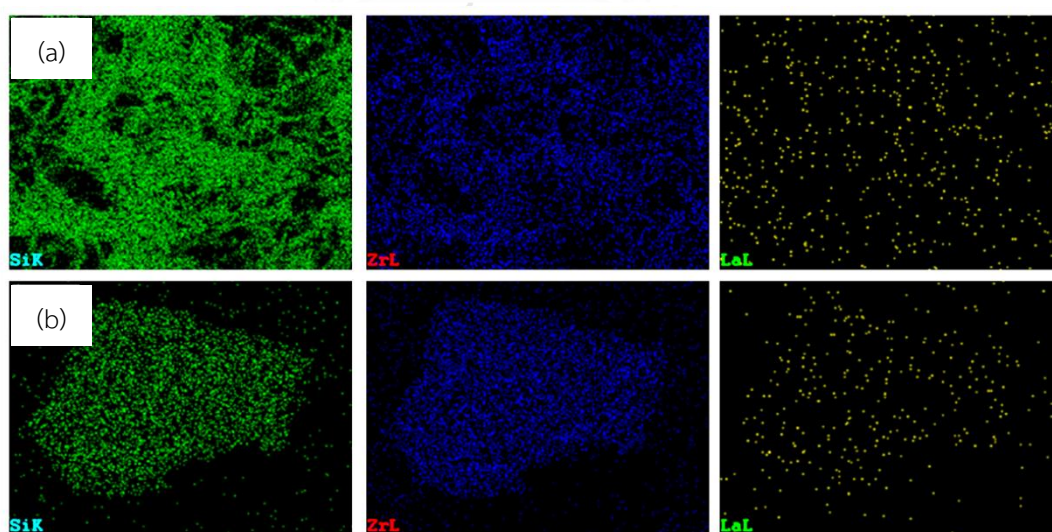


Figure 4.16 The typical EDX mapping of Zr-La/SBA-15-SG (a) and Zr-La/SBA-15-HT (b) catalysts.

The amount of each element near the surface of catalyst granule can be determined quantitatively. The results are summarized in **Table 4.2**. The key elements to be considered are Zr and bimetallic Zr-La. For both synthesized SBA-15 catalysts, the percentage of silica decreased due to conceal with metal oxide particle. For those catalysts synthesized by hydrothermal method, the percentage variation of metal oxide (especially Zr element) is higher than the percentage variation of catalysts synthesized by sol-gel method. Therefore, this result can be ascribed to amount of metal oxide loading to exceeding monolayer content, which may block the pore on surface or attach into the pore [132]. Thus, for the detected value of catalysts synthesized by hydrothermal method, metal oxide was easily incorporated into the channels of SBA-15. Moreover, the EDX has limit detection about 2-5 microns from the surface, which cannot detect deep metal oxide in the pore.

Table 4.2 The amount of each element near the surface of catalyst granule obtained from EDX

Catalysts	Amount of weight on surface (wt %)			
	Si	O	Zr	La
SBA-15-SG	50.2	49.8	0	0
Zr/SBA-15-SG	37.4	43.4	19.2	0
Zr-La/SBA-15-SG	37.7	41.3	19.3	1.7
SBA-15-HT	48.1	51.9	0	0
Zr/SBA-15-HT	13.0	35.6	51.4	0
Zr-La/SBA-15-HT	12.8	35.3	46.4	5.5

4.1.6 Transmission electron microscopy (TEM)

The morphological features of the catalysts prepared by sol-gel and hydrothermal methods were studied by TEM technique. As shown in **Figure 4.17**, the synthesized SBA-15 by sol-gel clearly indicated that the catalysts retained the uniform hexagonal mesostructured pores shape. The arrangement of these mesopores is rather ordered, showing a long-range ordering of the mesostructure. In the TEM image of Zr-La/SBA-15-SG, in the boundary region of the crystal study, the mesostructure is highly ordered. However, in the center area, the arrangement of pore system is rather disordered. This is in agreement with previous reports that the catalyst with high zirconium content $\text{Si/Zr} = 5$ may result in diminishing of the structural regularity of the solid [83], which is in a good agreement with the result of the low-angle XRD result. For the synthesized SBA-15 by hydrothermal method, the pore size of the catalysts was remarkably larger than that of the catalysts synthesized by sol-gel without well-ordered hexagonal mesopores, suggesting that the framework of hexagonal ordering was not preserved after the hydrothermal method. In addition, all catalysts cause broadening of the peaks and decrease the diffraction peak intensity (**Figure 4.3**), indicating the decrease of crystallinity, but not the collapse in the pore structure of the mesoporous [133]. It should be emphasized that the agglomeration of primary particles obtained from the hydrothermal method exhibited the porous shape, which is quite different from previous reports [84]. This phenomenon could be attributed to their distinguishable synthesis conditions. Conventional SBA-15 is prepared by sol-gel in strongly acidic media, while the catalysts prepared by hydrothermal method are synthesized in near neutral condition with high temperature and high pressure. The results were in agreement with those obtained by low-angle XRD and N_2 adsorption/desorption presented in **Table 4.1**.

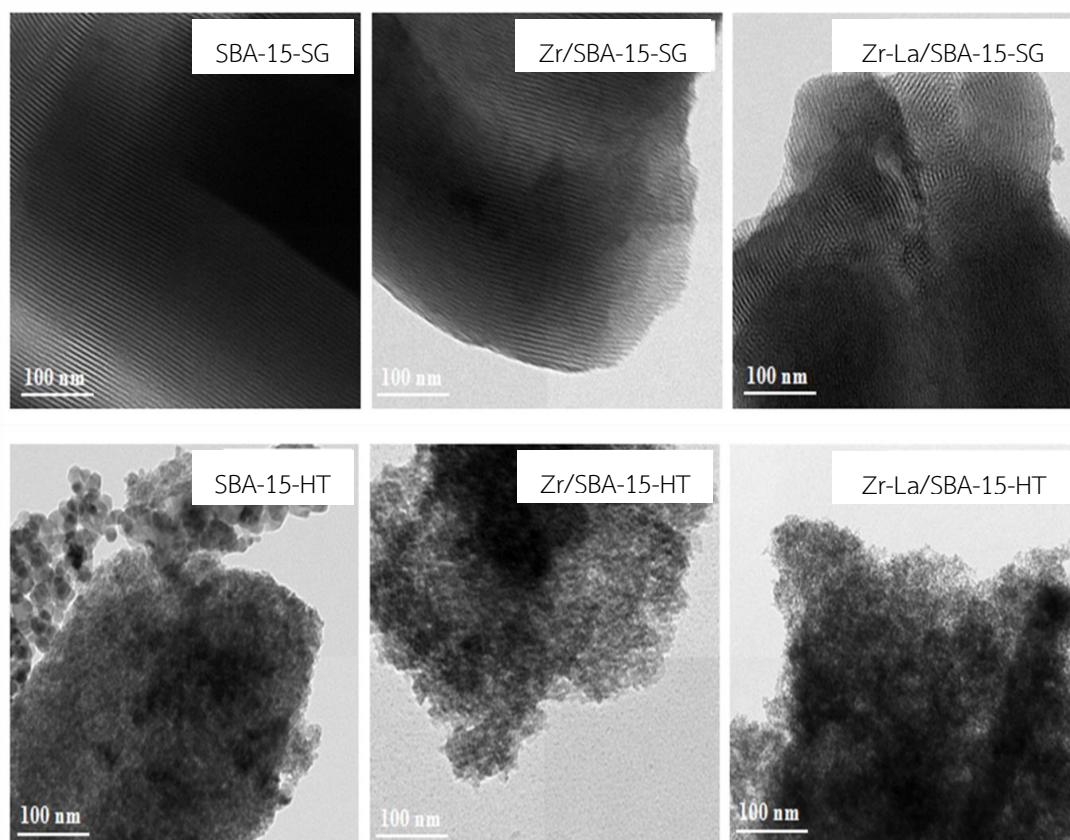


Figure 4.17 TEM micrographs of all catalysts obtained by sol-gel and hydrothermal methods.



4.1.7 Temperature-programmed desorption of ammonia (NH₃-TPD)

The surface acidity of the catalysts was measured by NH₃ temperature-programmed desorption (NH₃-TPD) between 100 to 550 °C. **Table 4.3** shows the number of acid site on catalysts calculated by integration of desorption areas of ammonia according to the Gauss curve fitting method, which are related to the acid sites on the catalysts. The TPD profiles (**Figure 4.18-4.19**) for all catalysts indicated two different types of acid site. The assignment of desorption peaks between 175 to 300 °C is weak acid sites and the desorption peaks occurred above 300 °C refer to medium-strong acid sites [88]. Although NH₃-TPD technique has some drawbacks [24],

it is fast, simple, and frequently employed method to evaluate the acidity. Firstly, the synthesized SBA-15-SG exhibits the lowest amount of weak acid site. The incorporation of Zr and bimetallic Zr-La into SBA-15 increases the weak and total acid sites. It can be observed that the Zr and bimetallic Zr-La can alter the acidity of SBA-15, demonstrating the suitable dispersion of the active phase. This can be attributed to the Zr^{4+} ions diameter (0.084 nm) and La^{3+} ions diameter (0.272 nm) is much larger than that of Si^{4+} ion (0.026 nm) when smaller Si^{4+} ions are replaced by larger Zr^{4+} and La^{3+} ions in the framework of the solid. The bond length of Zr–O–Si and Zr–La–O–Si clearly differs from the one of Si–O–Si [83, 134], which is corresponding to the Brønsted acid sites. It should be noted that the amount of weak acid site is probably more related to the Brønsted acid site, whereas Lewis acid site is more related to the strong acid site [135]. For SBA-15 catalysts prepared by hydrothermal method, an increase in the acidity was found when the catalyst is incorporated with Zr. However, the incorporation of bimetallic Zr-La into SBA-15 did not improve the total acidity (decreased from 1,773 to 1,114 $\mu\text{mole NH}_3/\text{g cat.}$), which could be described by the reduction of its surface area, blocking of NH_3 molecules in which the amount of acid sites decreases. It appears that the alteration of acidity of these materials can be useful to further apply for catalytic reactions, where acid sites are necessary such as alcohol dehydration or esterification. Therefore, the difference in catalytic behavior of SBA-15 (SG and HT) catalysts upon acidity is discussed further.

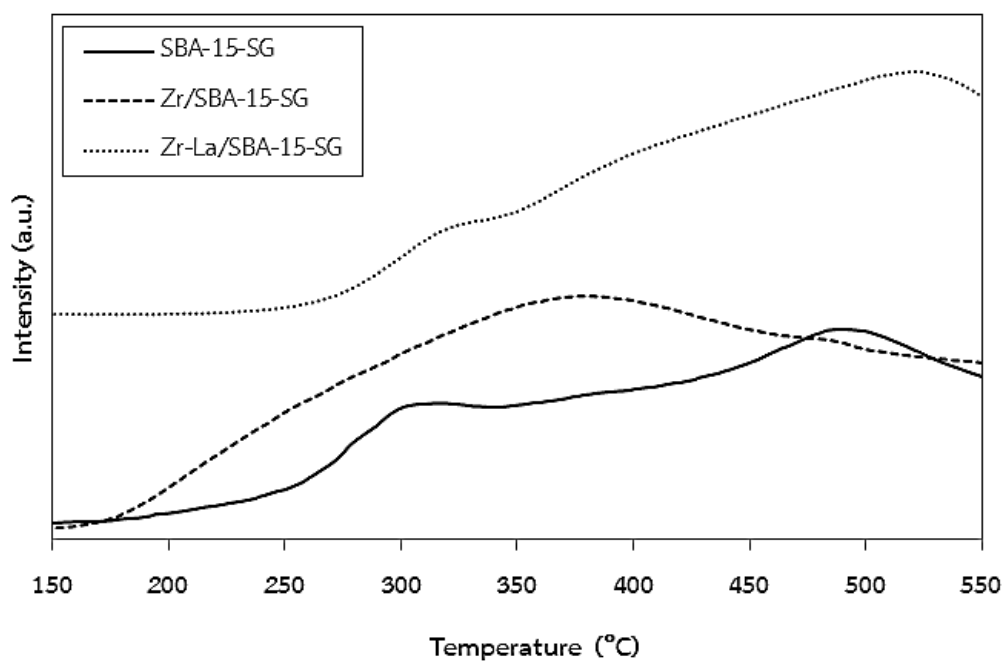


Figure 4.18 NH₃-TPD profiles of all catalysts obtained by sol-gel method.

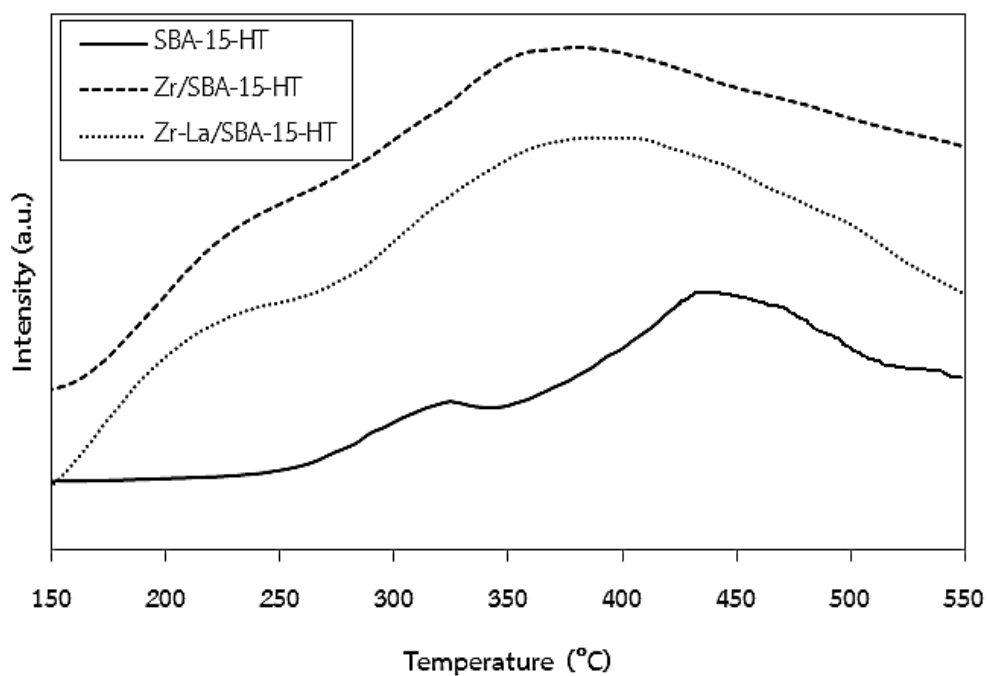


Figure 4.19 NH₃-TPD profiles of all catalysts obtained by hydrothermal method.

Table 4.3 The surface acidity of all catalysts from NH₃-TPD

Catalysts	Number of acid site ($\mu\text{moleNH}_3/\text{g cat.}$)		
	Weak acid sites	Medium-Strong acid sites	Total acid site
SBA-15-SG	31.3	470.4	501.7
Zr/SBA-15-SG	251.4	314.3	565.7
Zr-La/SBA-15-SG	324.1	412.1	736.2
SBA-15-HT	177.8	928.7	1,106.5
Zr/SBA-15-HT	830.9	942.1	1,773.0
Zr-La/SBA-15-HT	451.8	662.2	1,114.0

4.2 Ethanol dehydration reaction

In this section, zirconium and bimetal of zirconium and lanthanum (Zr-La) containing mesoporous silicas (SBA-15) synthesized by the sol-gel and hydrothermal methods, were used as catalysts for ethanol dehydration to explore an alternative way for improvement of the catalytic performance. All catalysts were tested in the gas phase catalytic dehydration of ethanol in the temperature ranging from 200 to 400°C. The reaction results were reported in terms of ethanol conversion, ethylene selectivity, and yield with respect to temperature profile.

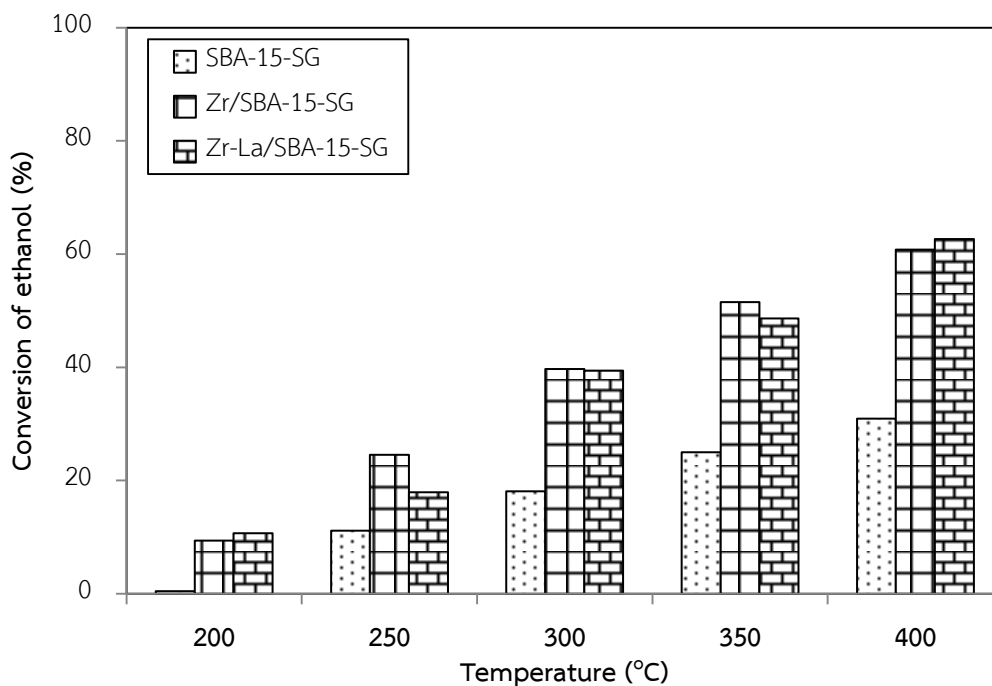


Figure 4.20 The conversion of ethanol over SBA-15 synthesized by sol-gel method.

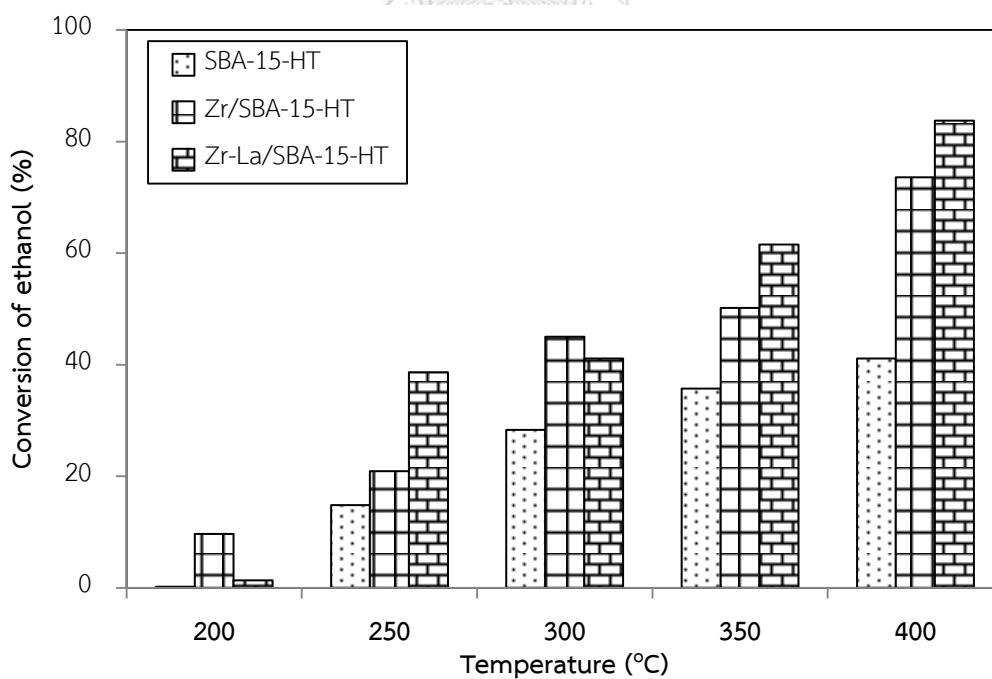


Figure 4.21 The conversion of ethanol over SBA-15 synthesized by hydrothermal method.

In order to measure the catalytic activity and product distribution, the catalytic ethanol dehydration reaction was performed over SBA-15 catalysts obtained by sol-gel and hydrothermal methods in the temperature range from 200 to 400°C. The results of ethanol conversion for all catalysts are shown in **Figure 4.20-4.21**. The increased temperature apparently resulted in an increase in ethanol conversion of both catalysts obtained from the sol-gel and hydrothermal methods. It can be observed that the ethanol conversion obtained from SBA-15 catalyst was the lowest because of weak reactivity of silica surface. It can be observed that the Zr-La/SBA-15-HT catalyst exhibited the highest ethanol conversion of 84% at 400°C among other catalysts. The enhanced catalytic activity is related to the reaction pathway. Basically, for ethylene production via catalytic dehydration of ethanol, there are two competitive pathways during reaction. At lower temperature, diethyl ether (DEE) is significantly produced by dehydration of ethanol. At temperature above 350°C, DEE decreases or disappears due to its decomposition to ethylene at high temperature [114]. Acetaldehyde is also produced by dehydrogenation of ethanol as a side reaction.

Considering the product distribution, the selectivity of ethylene is related to the reaction temperature as also reported by many authors [85, 136]. The selectivity (in mol %) is defined as the molar ratio of a specific product to all products present (ethylene, acetaldehyde and diethyl ether). As shown in **Figure 4.22-4.23**, the pure SBA-15-SG and -HT catalysts exhibited the lowest ethylene selectivity at low temperature. However, the selectivity of ethylene gradually increased with incorporation of Zr and bimetallic Zr-La in SBA-15 catalysts with increased temperature. It is suggested that the incorporation of Zr and bimetal Zr-La into the framework of SBA-15 is responsible for the formation of Brønsted acid sites. Salas et al. [83] reported that the bond between Zr and Si leads to structural microstrain

within in lattice cell and this is one of the possible origins giving rise to the Brønsted acid site. In fact, it should be noted that the addition of La metal into Zr/SBA-15 as the bimetallic Zr-La in SBA-15 (for both methods) did not increase ethylene selectivity significantly at high temperature (ca. 400°C). It is likely that this only increases the strength of medium-strong acid sites, but it does not affect the weak acid site.

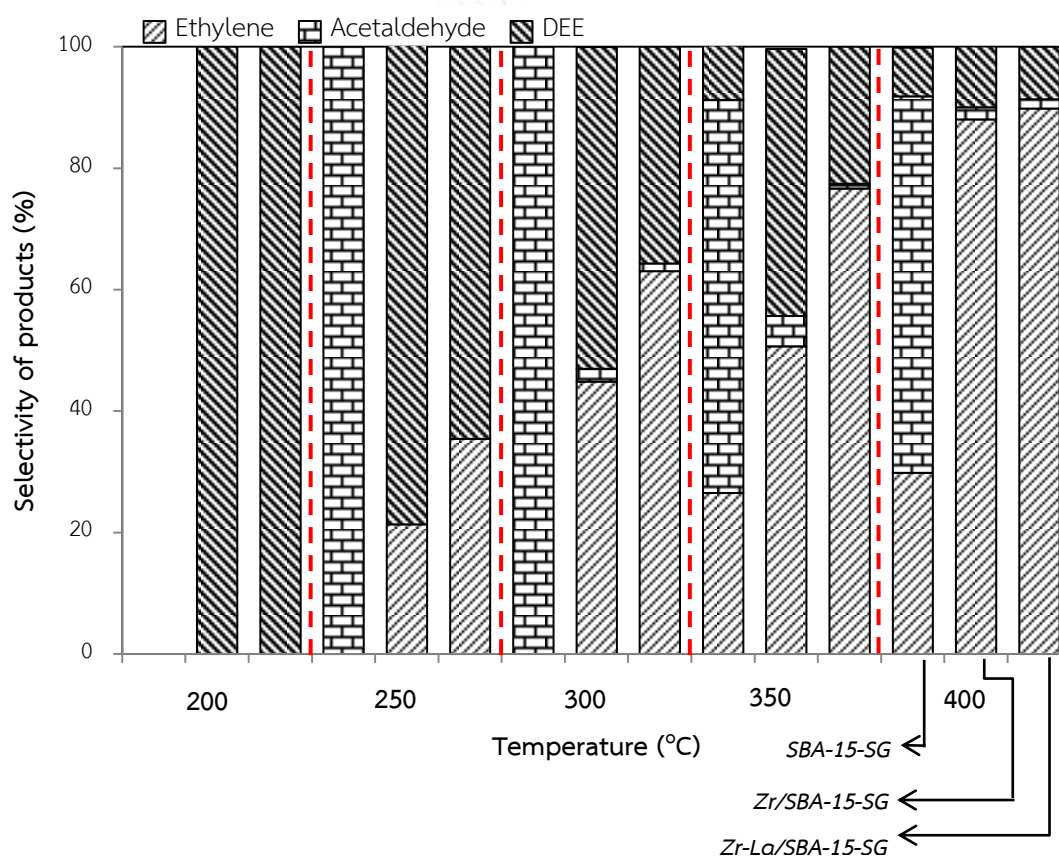


Figure 4.22 The selectivity of products over SBA-15 synthesized by sol-gel method.

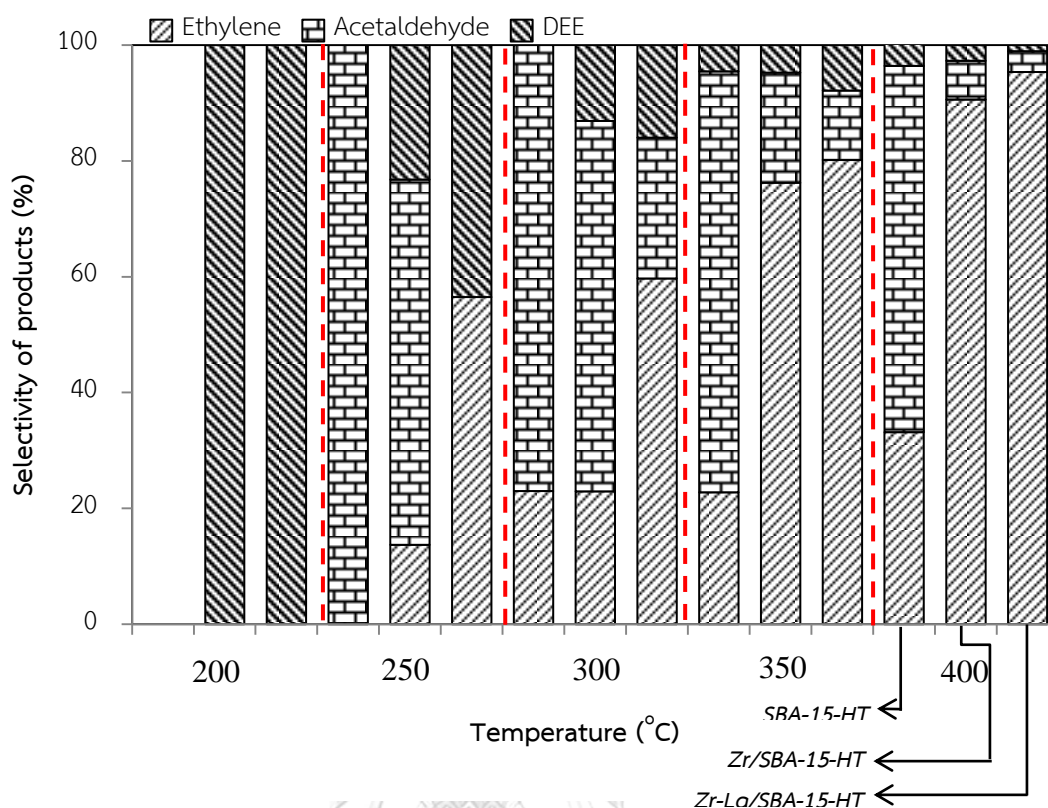


Figure 4.23 The selectivity of products over SBA-15 synthesized by hydrothermal method.

จุฬาลงกรณ์มหาวิทยาลัย
CHULALONGKORN UNIVERSITY

In order to investigate the effect of preparation methods on ethanol dehydration, the SBA-15 catalysts synthesized by sol-gel and hydrothermal methods were studied. It was found that the SBA-15 catalysts obtained by hydrothermal method showed better activity for ethanol dehydration gaining the complete conversion at 400 °C than the ones obtained from the sol-gel method. Based on the results of NH_3 -TPD, it seems to have a relationship between the activity and the weak acid sites of SBA-15 catalysts. As seen, the catalyst possessing higher number of weak acid sites showed better catalytic activity on ethanol dehydration. The higher activity of SBA-15 catalysts obtained by hydrothermal method can be attributed to

their higher surface area and higher amount of surface acidity, especially for the Zr-La/SBA-15-HT catalyst giving the highest ethylene selectivity of 95% at 400 °C despite having lower weak acid site (451.8 It is generally accepted that the amount of weak $\mu\text{mole NH}_3/\text{g cat.}$) than the Zr/SBA-15-HT (830.9 $\mu\text{mole NH}_3/\text{g cat.}$). This can be explained by the reduction of its surface area, blocking of NH_3 molecules whereupon the number of acid sites decreases [41]. In addition, the similar trend was found by Chanchuey et al. [47], where they reported that the acid property of catalysts depended on the metal loading. They found that increased metal (Mo) loading in catalysts (Al-SSP) resulted in increased weak acid sites, which enhanced the catalytic activity of ethanol dehydration acid site is probably more related to the Brønsted acid site indicating that it has relative stronger strength of acid sites in dehydration reaction. In contrast, Lewis acid site is more related to the strong acid site [50].

In addition, the pure SBA-15 catalysts obtained by sol-gel and hydrothermal methods still showed high acetaldehyde selectivity of 62% and 63% at 400°C, respectively, although they had weak reactivity of silica surface. Jankowska et al. [51] reported that thermal treatment or the temperature used in the reaction at 400°C presented the basic functional groups more than acid functional groups because the heat treatment caused an oxidation of Lewis oxygen within the structure of silica surface with basic site more than acid site. Moreover, further raising the reaction temperature from 350 to 400°C decreased the quantity of acid group on the SBA-15 surface.

From the product selectivity presented in **Figure 4.23**, it is obvious that the Zr-La/SBA-15-HT was able to dehydrate ethanol to ethylene with 95% selectivity at 400°C, while at this temperature, ethylene selectivity was only 91% and 33% for Zr/SBA-15-HT and SBA-15-HT, respectively. Although the SBA-15 catalysts obtained by sol-gel method showed lower activity than the ones obtained from the hydrothermal method, the ethylene selectivity was found to be in the order of Zr-La/SBA-15-SG > Zr/SBA-15-SG > SBA-15-SG. The outstanding catalytic performance of all SBA-15 catalysts (SG and HT) indicated that there might be some interactions between metal (Zr and Zr-La) used in each method, which played an important role in the ethanol dehydration to ethylene. Considering the ethylene yields (product of ethanol conversion and ethylene selectivity) obtained from each catalyst, they are shown in **Figure 4.24-4.25**. At lower temperature (ca. 200°C), there was no ethylene produced for all SBA-15 catalysts (SG and HT). Fundamentally, it increased with increasing reaction temperature up to 400°C. At this temperature, the highest ethylene yield (80%) with only slight amounts of DEE and acetaldehyde (**Table 4.4**) was obtained from the Zr-La/SBA-15-HT catalyst. The increased ethylene yield is associated with the appearance of Brønsted acid site due to the replacement of tetravalent Si^{4+} by larger Zr^{4+} and La^{3+} ions in the framework of the SBA-15 mesoporous silica.

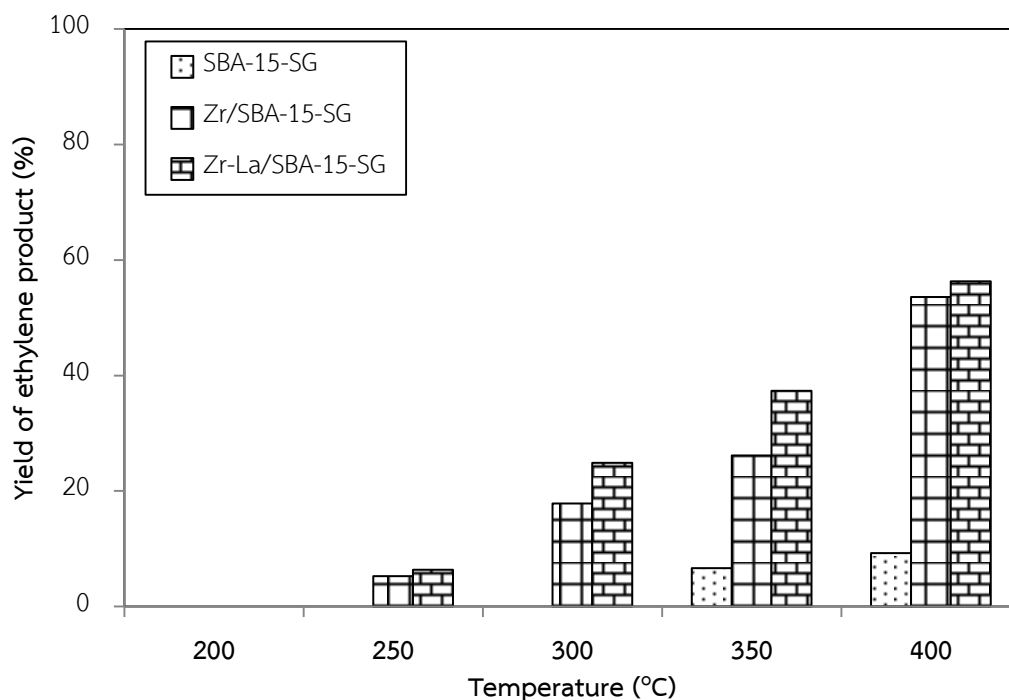


Figure 4.24 Yield of ethylene product over SBA-15 synthesized by sol-gel method.

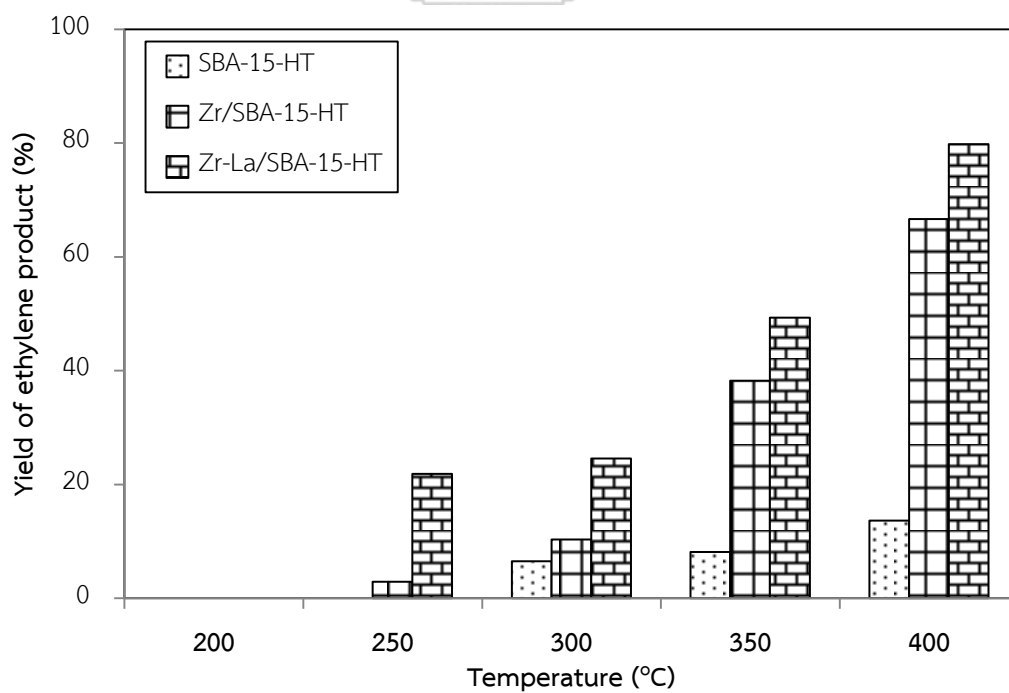


Figure 4.25 Yield of ethylene product over SBA-15 synthesized by hydrothermal method.

Table 4.4 Product yield obtained from ethanol dehydration at 400 °C.

Catalysts	Yield of products (wt %)		
	Ethylene	Diethyl ether	Acetaldehyde
SBA-15-SG	9.23	2.43	19.25
Zr/SBA-15-SG	53.54	4.86	1.17
Zr-La/SBA-15-SG	56.28	5.41	0.94
SBA-15-HT	13.61	1.47	25.98
Zr/SBA-15-HT	66.63	1.97	4.95
Zr-La/SBA-15-HT	79.82	0.85	3.04

4.3 Non-oxidative dehydrogenation and oxidative dehydrogenation of ethanol over different VOx/SBA-15 catalysts

This section was to synthesize the solid basic catalysts having vanadium oxides as the active phase dispersed on different SBA-15 supports with zirconium (Zr) and zirconium-lanthanum (Zr-La) modification. Then, the different VOx/SBA-15 catalysts were also tested in non-oxidative dehydrogenation and oxidative dehydrogenation of ethanol to produce acetaldehyde. The characteristics and catalytic properties depending on the role of basic sites and types of VOx species will be elucidated.

4.3.1 Characteristics of different VO_x/SBA-15 prepared by sol-gel and hydrothermal methods

4.3.1.1 X-ray diffraction pattern (XRD)

Figure 4.26 shows the SAXS patterns of vanadium doped SBA-15 based catalysts obtained from sol-gel method in the low angle region ($2\theta = 0.5^\circ$ - 3.5°). It exhibits three well resolved diffraction peaks, which can be indexed as the (100), (110) and (200) reflections associated with hexagonal symmetry [105, 137]. Comparison of the diffraction spectra of V/SBA-15-SG shows that the highly well-ordered patterns are still retained on V-Zr/SBA-15-SG and V-Zr-La/SBA-15-SG catalysts, while there was a decrease or may disappear in the intensity of the reflection peaks (100) and (200). The decrease of the reflection peaks was observed due to the substitution of metals into mesoporous silicate and slight collapse of mesostructure of the Si/Zr and Si/Zr-La support. Similar results have been found by other researchers [84, 104]. For XRD patterns in the high-angle regions (**Figure 4.27**), it can be observed that all catalysts have a broad peak centered between 21 - 25° , attributed to the amorphous character of the SBA-15. However, no diffraction peak for vanadium oxide or any metal oxide can be observed, suggesting that no crystalline vanadium oxide with remarkable size exists on SBA-15 catalysts obtained by sol-gel method. For catalysts obtained by hydrothermal method, the reduced order of homogeneity of the pores can be observed in the XRD data (**Figure 4.28**), as the (110) and (200) reflections almost disappear for the extensively washed in the last step of experimental as described by Thielemann et al. [26, 107, 108]. Moreover, high-pressure large scale autoclave used to prepare the catalysts obtained by this method causes the agglomeration of primary particles having a lot of porous shapes, with a decrease in crystallinity without collapse in the pore structure of the

mesoporous [87]. As a result, the mesopore structure of the catalysts obtained by hydrothermal method becomes less ordered than that of SBA-15 obtained by sol-gel method, except in the case of V/SBA-15-HT catalyst, which exhibits three resolved peaks at 0.84 , 1.42 and 1.64 features of SBA-15 with hexagonal symmetry due to weak bond strength and low electron density of vanadium on SBA-15 as can be further described and seen by TEM technique. The high-angle XRD pattern of catalysts obtained by hydrothermal method was broad because the sizes of metal oxide were very small, which is similar as seen in **Figure 4.29**.

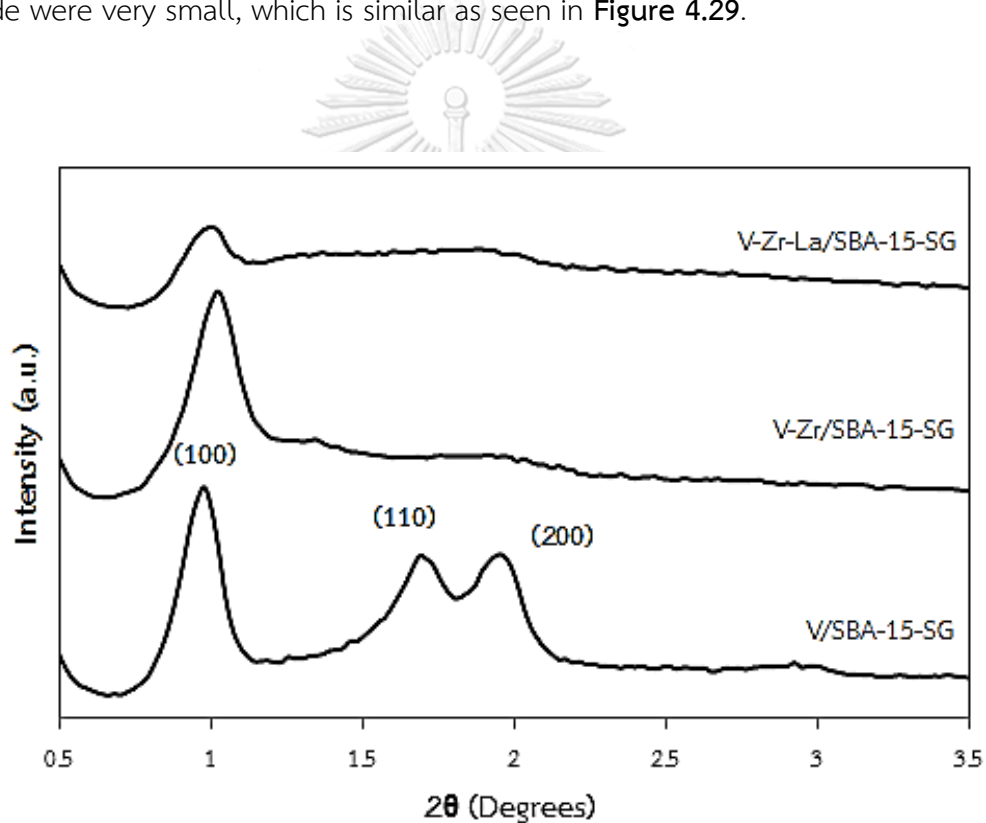


Figure 4.26 XRD patterns of all catalysts obtained from the sol-gel method at low-angle regions

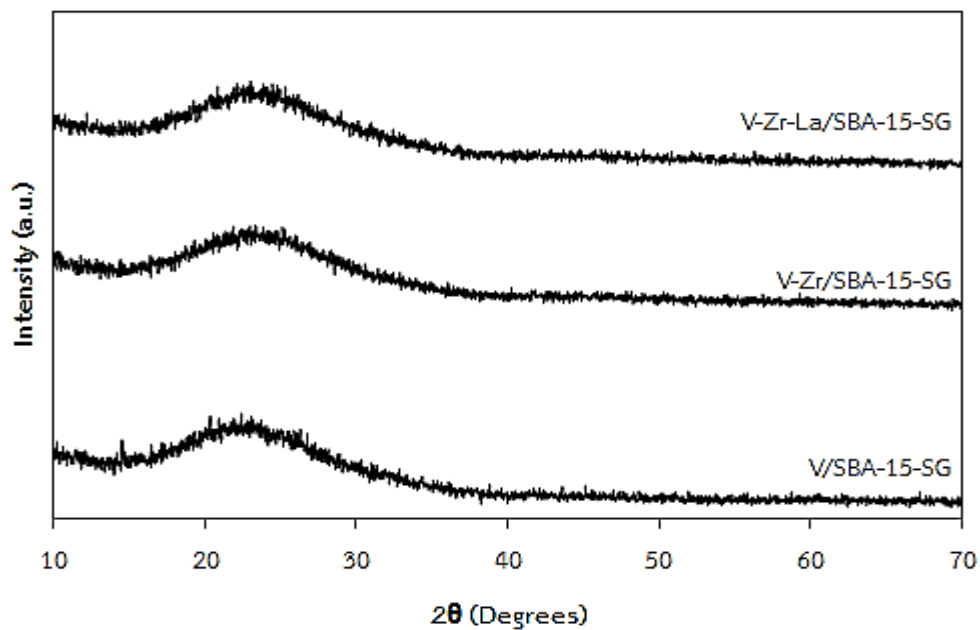


Figure 4.27 XRD patterns of all catalysts obtained from the sol-gel method at high-angle regions.

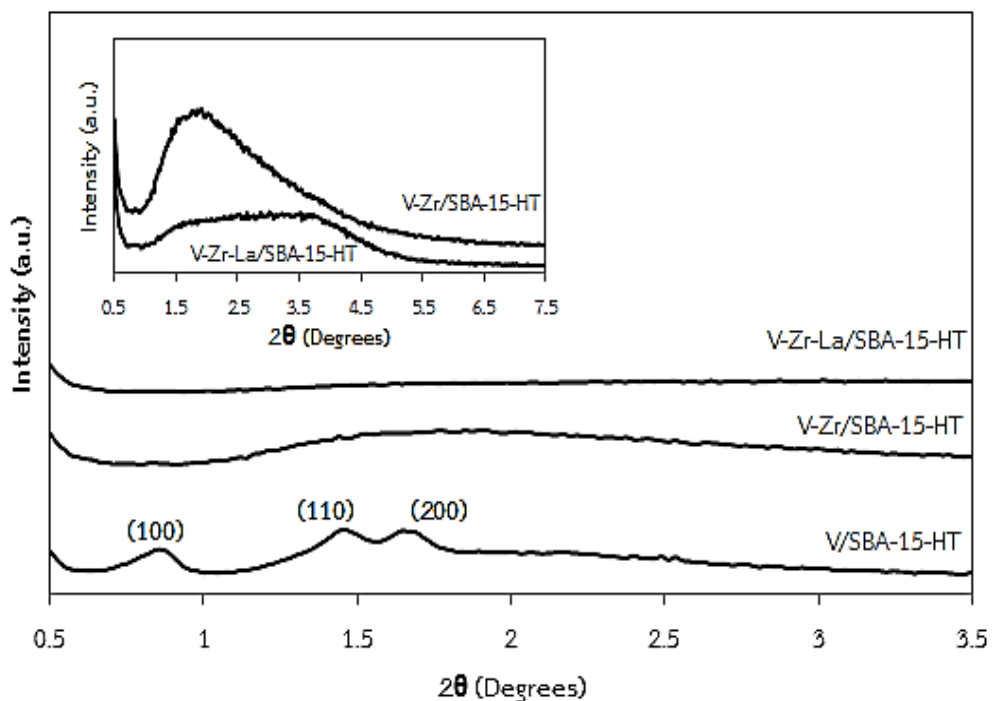


Figure 4.28 XRD patterns of all catalysts obtained from the hydrothermal method at low-angle regions.

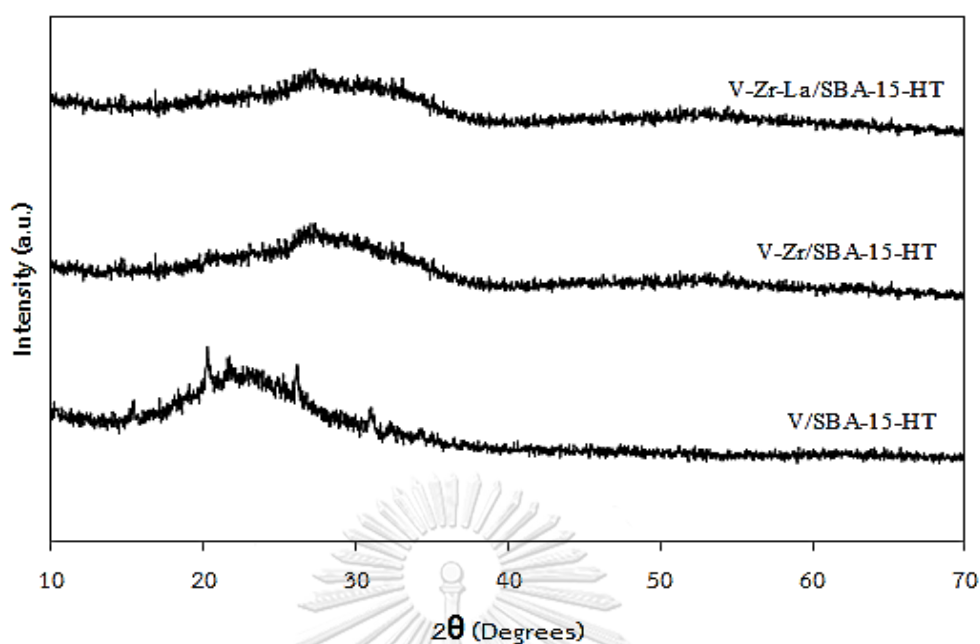


Figure 4.29 XRD patterns of all catalysts obtained from the hydrothermal method at high-angle regions.

4.3.1.2 N₂-physisorption

The mesoporous character of different VO_x/SBA-15 catalysts have been confirmed from the corresponding nitrogen adsorption–desorption isotherms at -196°C (**Figure 4.30-4.31**), where the typical irreversible type IV adsorption isotherms with a H1 hysteresis loop as defined by IUPAC classification were observed. The isotherms of catalysts obtained by the sol-gel method showed quite different patterns. Two inflection points and hysteresis loop moved toward lower relative pressure ($P/P_0 = 0.3-0.7$). However, for the isotherms of catalysts obtained by hydrothermal method, the volume adsorbed inflected sharply at relative pressure ($P/P_0 = 0.7-0.9$). It can be illustrated that the relative pressure increases to the degree that capillary condensation within uniform pores occurred. Besides, it should be noted that the hysteresis in the high relative pressure range corresponds to the larger

mesoporosity character of SBA-15, confirming that vanadium species are located inside the internal pores or hexagonal framework of SBA-15 support.

The structural parameters of all catalysts derived from N₂ physisorption isotherms are summarized in **Table 4.5**. For SBA-15 catalysts obtained by sol-gel, the BET surface area of the SBA-15 catalysts increased from 512 to 561 m²/g when V₂O₅ incorporated in Zr/SBA-15-SG and Zr-La/SBA-15-SG due to the vanadium oxides were mostly located at the external surfaces as reported by previous work [114], whereas the average pore diameter was rather similar for the different catalysts. For SBA-15 catalysts obtained by hydrothermal method, the pore volume of catalysts was higher than the ones obtained from sol-gel method. The BET surface area of the SBA-15 catalysts decreased from 528 to 172 m²/g compared with the surface area of pure vanadium on SBA-15 (V/SBA-15-HT). In addition, the low loaded (2 wt%) catalysts show appreciable changes of specific surface area and pore volume, even though the vanadium in these systems is highly dispersed as confirmed by the high-angle diffraction peak of XRD (**Figure 4.29**). It can be observed that the clogging of SBA-15 support pores by vanadium species occurs that makes them inaccessible for nitrogen adsorption. Another important reason, it is caused by dilution of silica mass in the catalyst by vanadium, which results in substantially less total specific surface area than silica [138]. These results suggest that the hydrothermal method is a suitable procedure method, which can match the vanadium oxide easily incorporated into the surface channels of SBA-15 mesoporous structure. A plot of pore size distribution (PSD) between pore volume and pore diameter also confirms the isotherm assertion and change in pore structures as seen in **Figure 4.32-4.33**. It reveals that the pore diameters of all catalysts were produced a broader pore diameter between 2 to 50 nm indicating the mesoporous structure. These results indicate that the vanadium bond or vanadium species in SBA-15 could be crystallized without any decrease in mesopore size via the direct synthesis approach under both methods [139].

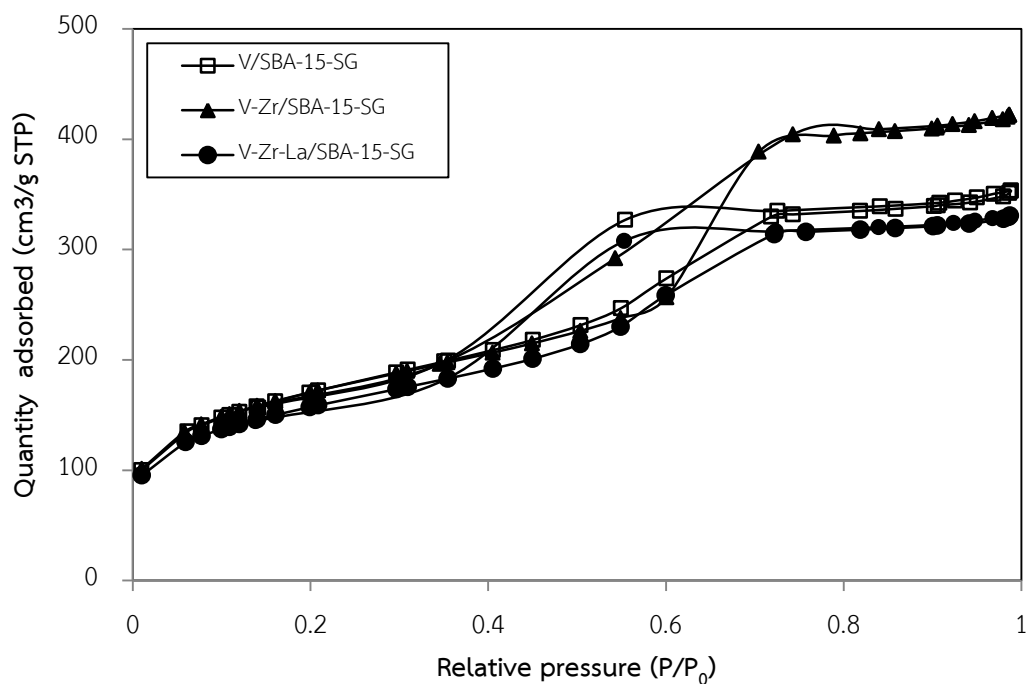


Figure 4.30 Nitrogen adsorption/desorption isotherms of all catalysts synthesized by sol-gel method.

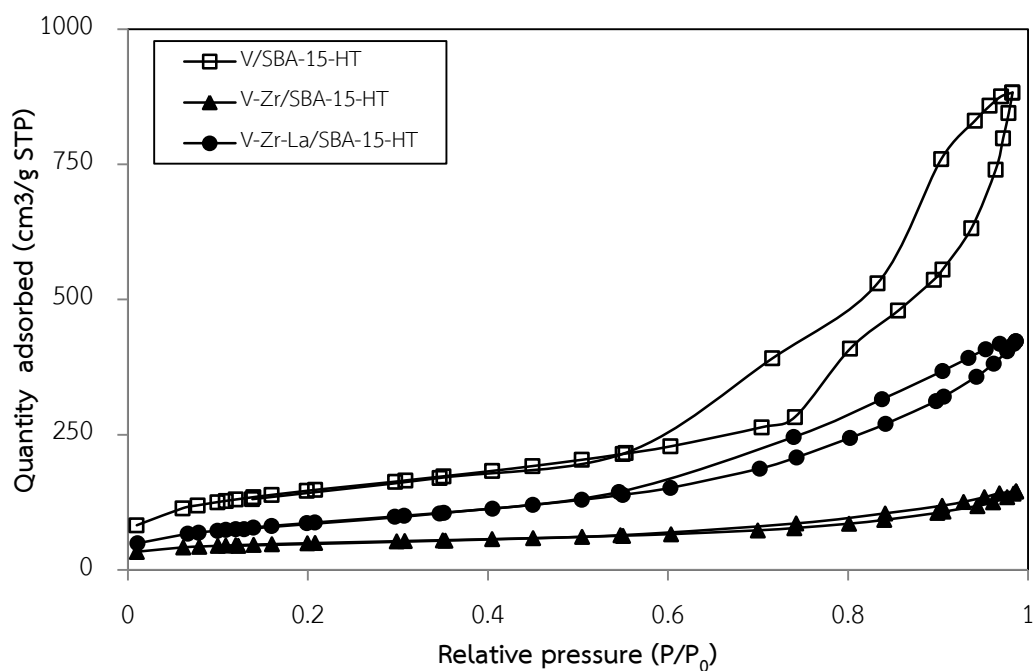


Figure 4.31 Nitrogen adsorption/desorption isotherms of all catalysts synthesized by hydrothermal method.

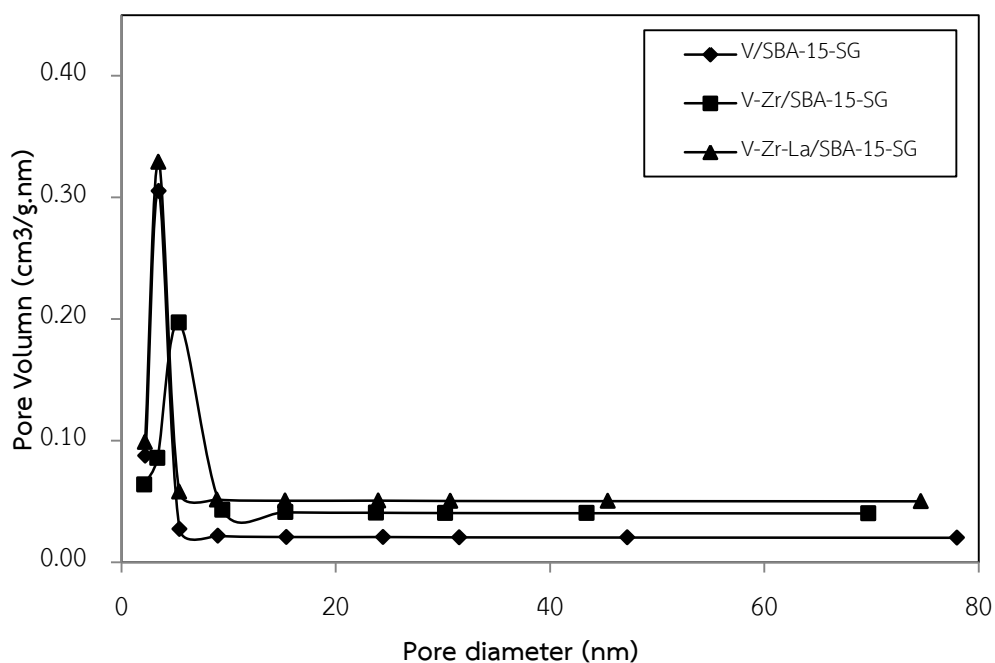


Figure 4.32 BJH pore size distribution of all catalysts obtained by sol-gel method.

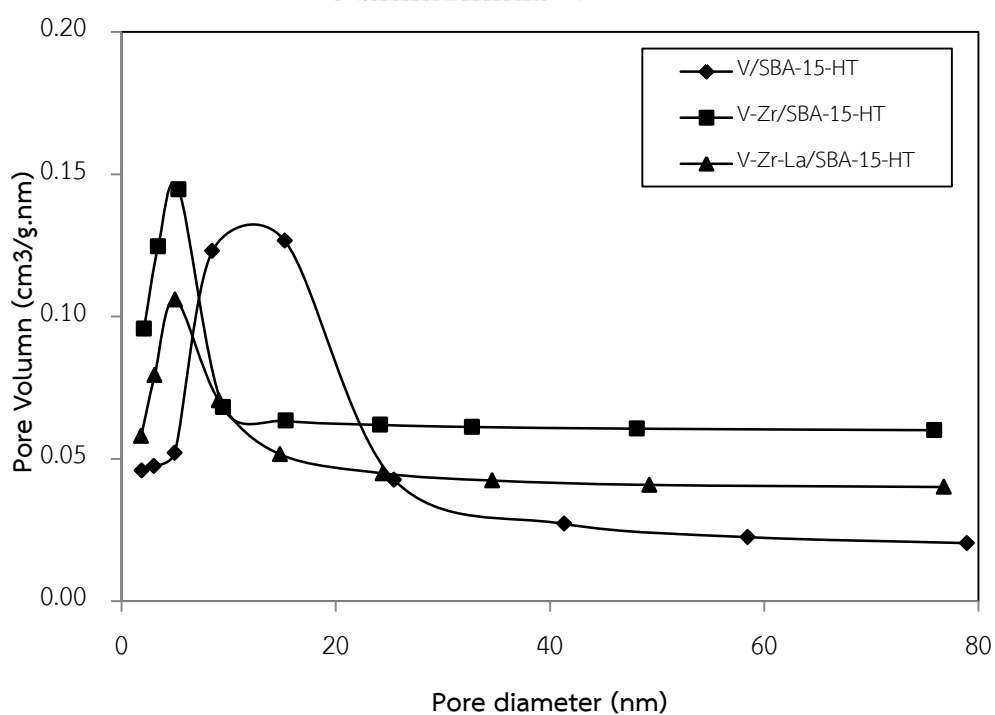


Figure 4.33 BJH pore size distribution of all catalysts obtained by hydrothermal method.

Table 4.5 Textural properties of all different VOx/SBA-15 catalysts.

Catalysts	Surface area (m ² /g)	Average pore diameter (nm)	Average pore volume (cm ³ /g)
V/SBA-15-SG	512	3.4	0.60
V-Zr/SBA-15-SG	523	3.9	0.69
V-Zr-La/SBA-15-SG	561	3.5	0.56
V-SBA-15-HT	528	8.9	1.38
V-Zr/SBA-15-HT	315	6.4	0.66
V-Zr-La/SBA-15-HT	172	6.5	0.21

4.3.1.3 Fourier-transform infrared spectroscopy (FTIR)

Infrared spectroscopy has been used extensively for the characterization of transition-metal cation modified molecular sieves. **Figure 4.34-4.35** reports the IR spectra of the vanadium doped SBA-15 based catalysts obtained by sol-gel (a) and hydrothermal (b) methods in the mid-infrared region from 4000–500 cm⁻¹ range for vibrational modes of the solid absorb. The two broad bands at 1300–1100 cm⁻¹ and 800 cm⁻¹ are readily assigned to the asymmetric and symmetric stretch vibrations of Si–O–Si (siloxane) groups of silica, respectively [140]. It is noteworthy that with the vanadium doped SBA-15 catalysts obtained by hydrothermal method, a weak band appears at *ca.* 930 cm⁻¹ (asterisk). It was assigned to a stretching vibration mode of a SiO₄ group unit bonded to a vanadium ion (Si–O–V) in vanadosilicate molecular sieves [141] indicating the vanadium species incorporated into the framework, especially for the SBA-15 catalysts obtained by hydrothermal method excepting for

the V-Zr/SBA-15-HT. This is because better dispersion of VO_x species inside silica walls is probably obtained. Other works have pointed out that the presence of this absorption band was ascribed to vanadyl oxygen stretching or symmetric stretching vibrations of V⁴⁺=O and the asymmetric vibration V–O–V, respectively [142]. This band was not detected for the catalysts obtained by sol-gel method due to the infinitesimal vanadium content and vanadium oxides were located mostly on the external surface as confirmed by the textural properties (**Table 4.5**). In the –OH spectral region (3000–4000 cm⁻¹), the band at ca. 3398–3750 cm⁻¹ corresponded to the vibration of physisorbed water due to easy hydration of the catalysts was observed [143]. This was very intense for the hydrothermal method. It has to be noted that vanadium species are introduced into the silica matrix with the formation of V–OH species. Their appearance, however, is difficult to be seen in IR spectra. They also show a peak at the same wavenumber [144], indicating that vanadium exists as a different species, which are not detectable as bulk V₂O₅. The remaining bands are due to lattice absorption and previously have been assigned to SBA-15 catalysts as described by Houwen et al. [145].

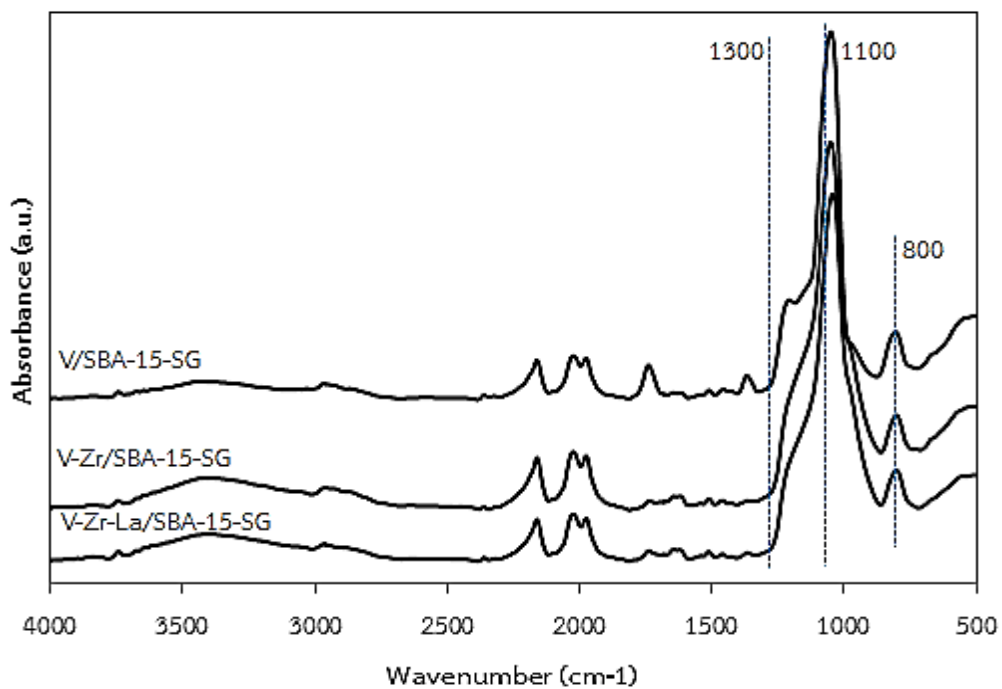


Figure 4.34 FTIR spectra of all catalysts obtained by sol-gel method.

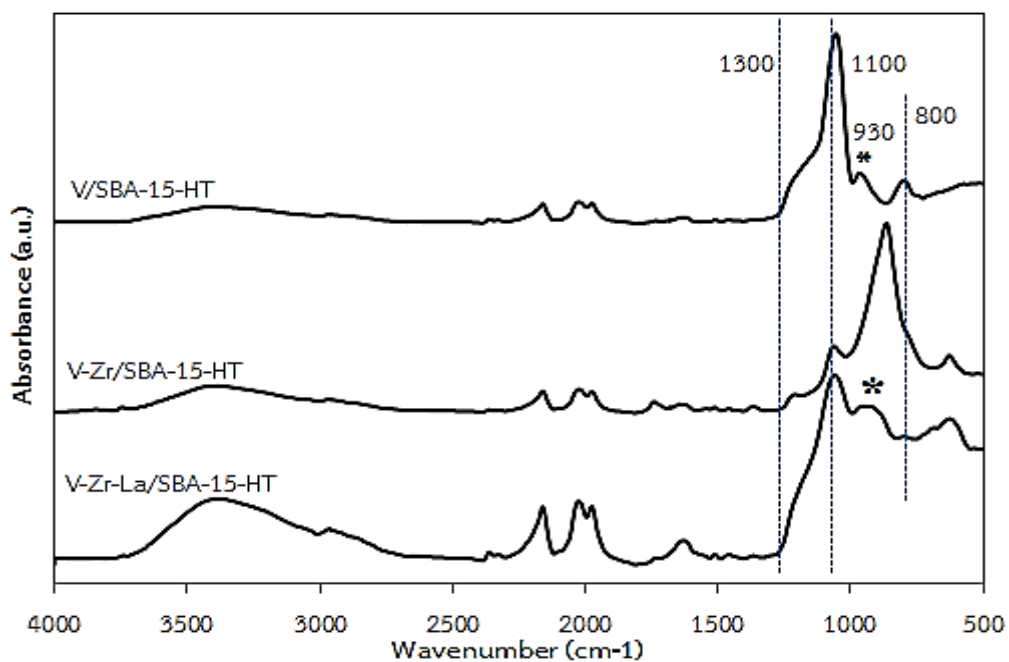


Figure 4.35 FTIR spectra of all catalysts obtained by hydrothermal method.

4.3.1.4 Raman spectroscopy

The Raman spectra of all vanadium incorporated in SBA-15 or VO_x species are shown in **Figure 4.36-4.37**. The Raman spectra of the prepared catalysts are presented in the spectra region of $200\text{--}1400\text{ cm}^{-1}$. Due to the low vanadium content (ca. 2 wt%), weak bands related to vanadium are observed. The vibrational resonance of the catalysts obtained by sol-gel method (**Figure 4.36**), exhibits no Raman signal because most of metal oxides were mostly located on the external surfaces, resulting into diminish of bond strength between metal and support. The intensity of Raman signals was depended on many factors (one of them was the quantity of sample probed among other such as structural defects, crystallinity and etc.). Usually, when a material did not lead to a sufficient signal, especially the vanadium catalysts obtained by sol-gel method, the wavelength of incident beam or the laser power should be increased. For catalysts obtained by hydrothermal method (**Figure 4.37**), the spectrum of V_2O_5 containing two weak bands is readily observed at 700 and 996 cm^{-1} . The former corresponds to lattice vibrations localized within the V-O-M ($\text{M} = \text{V}, \text{Zr}$ or La) bridge in the vanadium oxide structure, while the latter is responsible for the stretching vibration of vanadyl V=O bonds by vanadium atoms into SBA-15 framework. It is clear that the peak originates from a monoxo V=O stretch vibration, as also revealed by ^{18}O labeling that is related to the oxygen isotope exchange [146, 147]. The Raman band at 996 cm^{-1} was dominant in the spectra of V-Zr-La/SBA-15-HT . It can be shown that this catalyst contains predominantly vanadium in the form of isolated monomeric VO_x or VO_4^{3-} species. In addition, the d-orbital in Zr element may remain high-spin coupled, as is favored by exchange considerations, contributing little to the net bond energy. This balance between exchange and chemical bonding often hangs on the extent of the d-orbital relative to the p-orbital in V element [140], which dramatically decreased the Raman band at 996 cm^{-1} for V-Zr/SBA-15-HT catalyst.

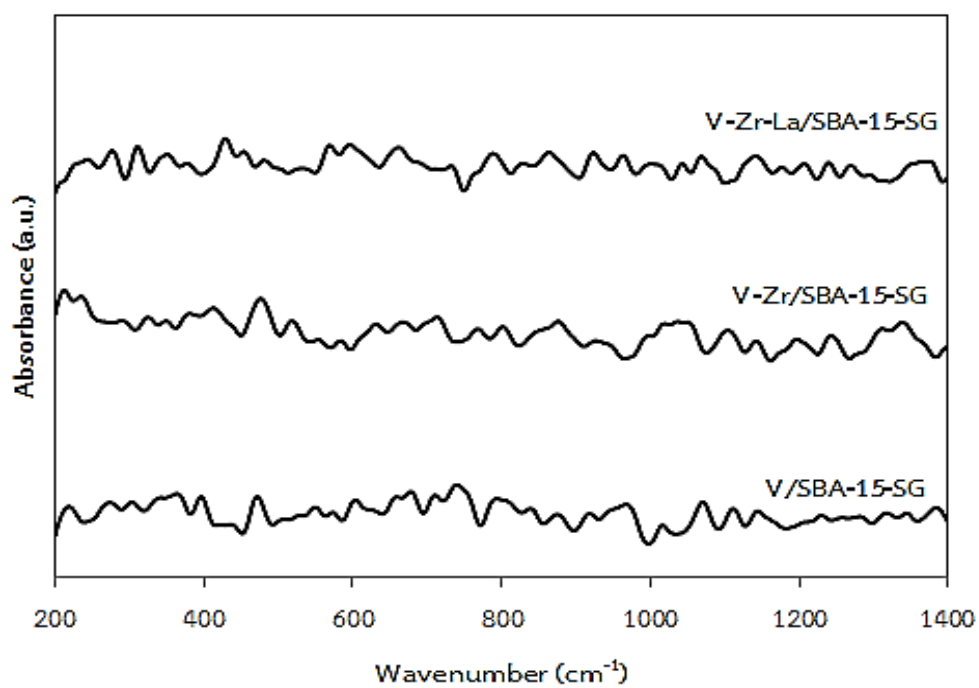


Figure 4.36 Raman spectra of all catalysts obtained by sol-gel method.

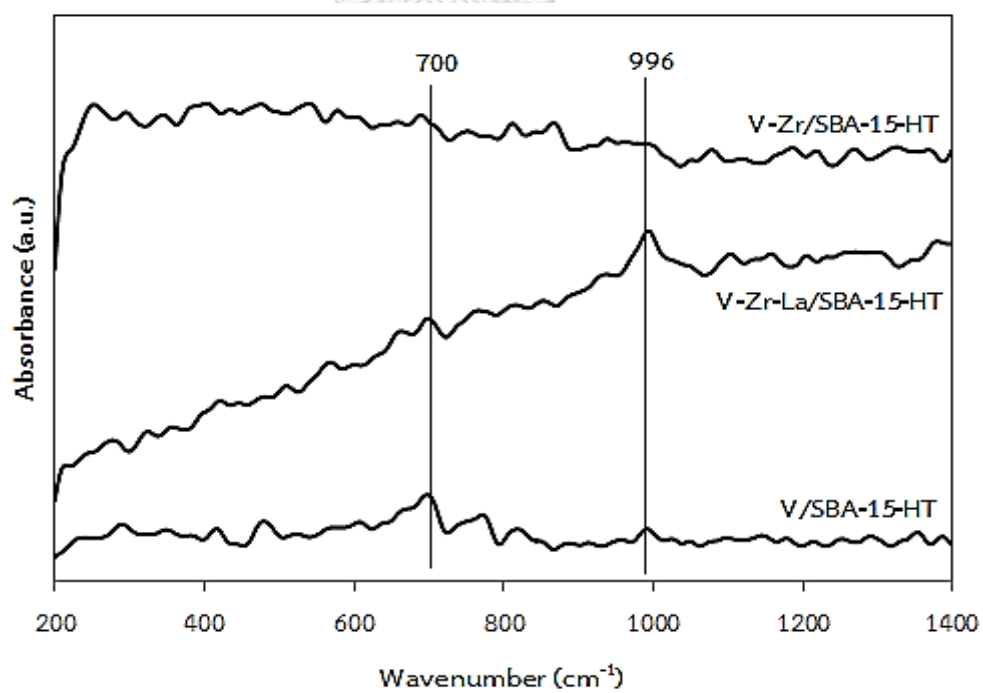


Figure 4.37 Raman spectra of all catalysts obtained by hydrothermal method.

4.3.1.5 UV-visible spectroscopy (UV-vis)

The diffuse reflectance UV-vis spectroscopy is promising as a very sensitive probe for the identification of metal ion coordination and its existence in the framework or in the extra framework position of metal-containing catalysts. **Figure 4.38-4.39** reveals the UV-vis DSR spectra of all catalysts obtained by sol-gel (a) and hydrothermal (b) methods. The spectrum of V/SBA-15 (-SG and -HT) shows two absorption bands between 250-380 assigned to (I) low-energy charge transfer transitions between tetrahedral oxygen ligands and isolated V^{5+} cations and (II) surface oligomeric V^{5+} species in tetrahedral coordination [148]. For V-Zr/SBA-15 and V-Zr-La/SBA-15 (-SG and -HT), the vanadium species are nearly completely removed and two components are observed at 250 and 360 nm for sol-gel method (**Figure 4.38**) and at 280 and 380 nm for hydrothermal method (**Figure 4.39**), compared with V/SBA-15 (-SG and -HT). Those two bands were assigned to highly disperse and low oligomeric tetrahedral V^{5+} species, respectively [41]. However, the band of isolated V^{5+} species of the catalysts obtained by hydrothermal, especially for V-Zr-La/SBA-15-HT (280 nm) is more intense than that of oligomeric VO_x species (380 nm). Therefore, a better vanadium dispersion and monomeric VO_x or VO_4^{3-} species can be achieved by this hydrothermal method.

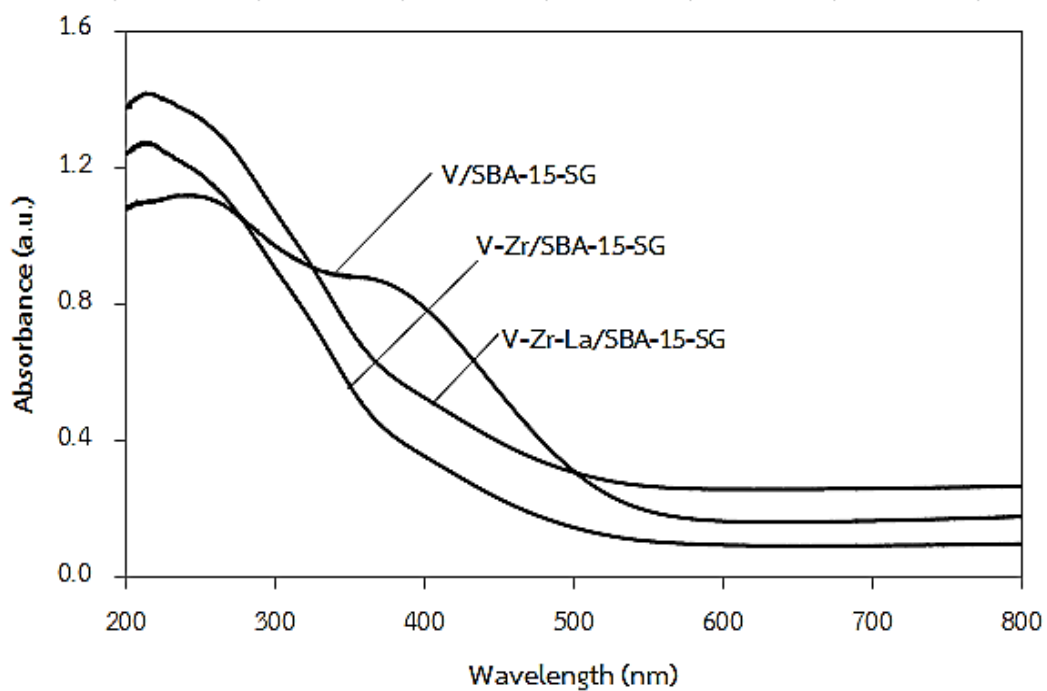


Figure 4.38 UV-Vis diffuse reflectance spectra of all catalysts obtained by sol-gel method.

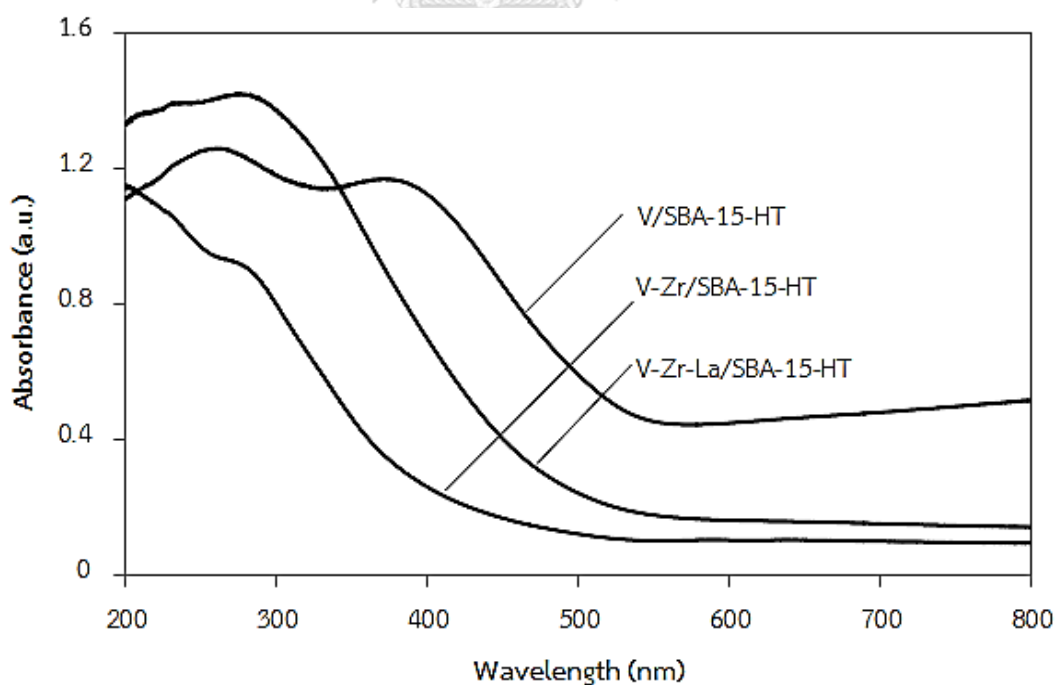


Figure 4.39 UV-Vis diffuse reflectance spectra of all catalysts obtained by hydrothermal method.

4.3.1.6 X-ray photoelectron spectroscopy (XPS)

In order to confirm the value state of the elements existed on the surface of the catalyst, X-ray photoelectron spectroscopy (XPS) analysis of V_2O_5 incorporated SBA-15 catalysts was conducted. **Figure 4.40-4.41** displays the full spectrum of different $VO_x/SBA-15$ catalysts (-SG and -HT). In addition, the observed Si 2p peak between 100.0-109.7 eV and O 1s peak at 535.0 eV are corresponding to Si and O elements in SBA-15, respectively [149]. However, the XPS peaks of O 1s (**Figure 4.43**) for V-Zr/SBA-15-HT and V-Zr-La/SBA-15-HT are shifted in the binding energy values. This shift is attributed to the redistribution of electric charge after the formation of the metal heteroatom, which is responsible for the disturbance of the local environment and electron density around the elements of the catalysts obtained by hydrothermal method [149]. It can be seen that the vanadium based SBA-15 catalysts had the O, C, Si and V elements. With the addition of vanadium into the Zr/SBA-15 and Zr-La/SBA-15 catalysts, the V, Zr and La elements were still detected in the sample, suggesting the successful incorporation of vanadium ions into the SBA-15 catalysts. This result agreed well with the results of Raman spectra. For the catalysts obtained by hydrothermal method, the peaks at 523.8 eV (lower binding energy) and 524.7-526.2 eV (higher binding energy) are also observed, corresponding to V(IV) 2p_{1/2} and V(V) 2p_{1/2}, respectively [150]. On the contrary, the catalysts obtained by sol-gel method (**Figure 4.42**) exhibit an opposite trend for the contribution of vanadium entities. It is shown that V(V) 2p_{1/2} entity was predominant, while the concentration of V(IV) 2p_{1/2} entity was lower or disappear in this catalysts. The existence of V(IV) could be ascribed to the decomposition of acetylacetonate ligand during the synthesis under high temperature conditions [151].

The Zr 3d spectra of the catalysts (-SG and -HT) are shown in **Figure 4.44-4.45**. The binding energies of 184.2 and 186.7 eV belong to ZrO_2 and Zr-V, respectively indicating zirconium ions in what form in the SBA-15 [152]. For V-Zr-La/SBA-15-HT, the binding energy shifted to binding energies state (184.0 and 186.5 eV) due to the relationship between zirconium ions and other metal oxides (V and La) dispersed on SBA-15. This conclusion also revealed that the presence of zirconium could enhance the dispersion and electron density of the active phase in SBA-15. For catalysts prepared by sol-gel method, they show a weak concentration spectra of Zr $3d_1$ and Zr $3d_2$ due to most of metal oxides were located on the external surface resulting in charge transfer between the active phase and the support, which in turn would decrease the binding energy [153]. It should be mentioned that using the surface-sensitive analytical technique such as XPS to analyze the oxidation states of V, Zr and La species of the SBA-15 catalysts obtained by sol-gel, is difficult to find the binding energy peak of metal oxide, especially for La 3d entity. This is because the La peak maybe shifted towards higher energies [154]. However, the EDX technique can confirm the existence and dispersion of these metal oxides in this study.

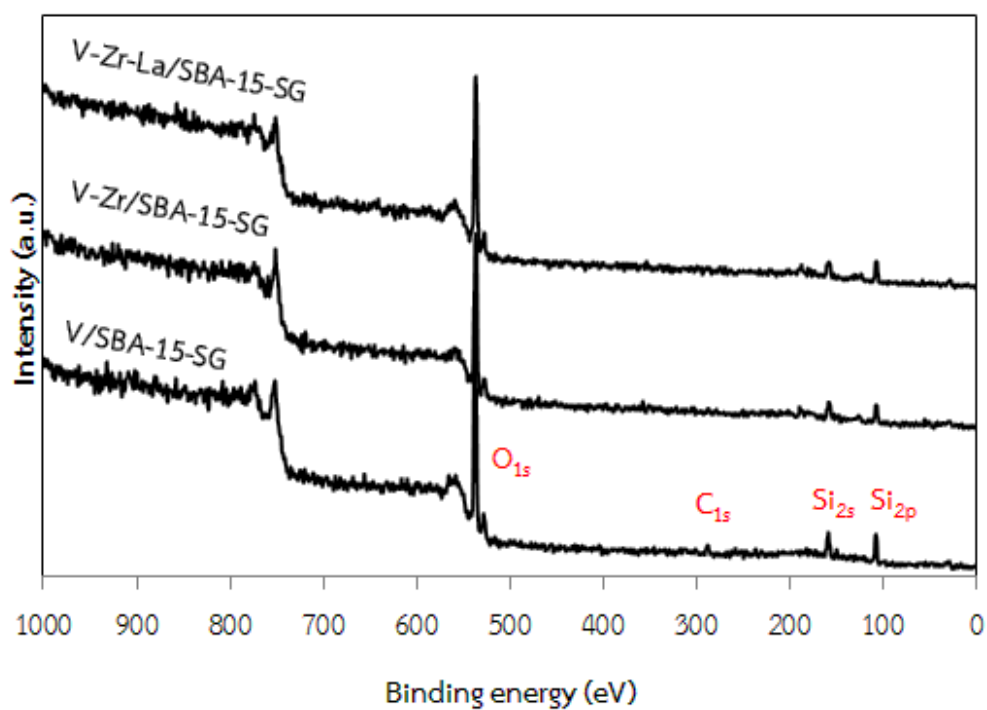


Figure 4.40 Full XPS spectrum of all catalysts obtained by sol-gel method.

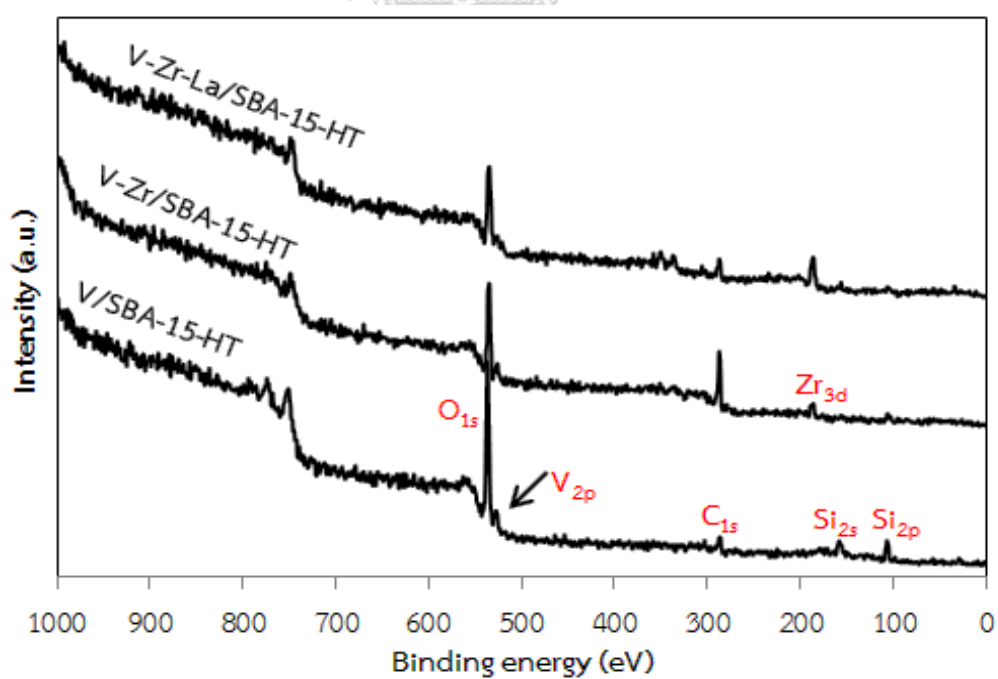


Figure 4.41 Full XPS spectrum of all catalysts obtained by hydrothermal method.

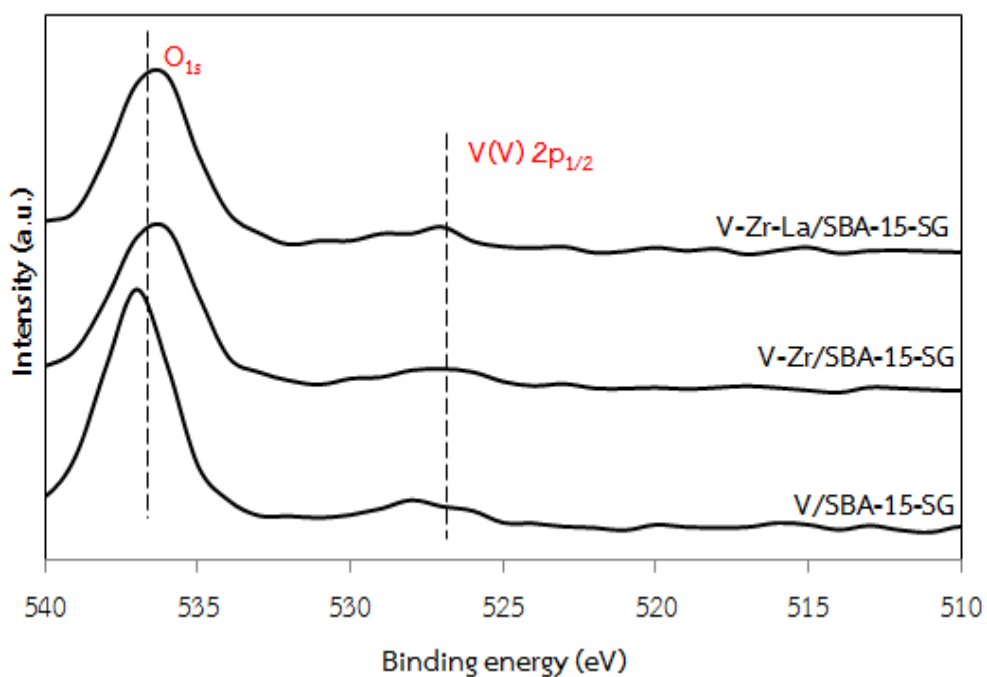


Figure 4.42 XPS spectra for O 1s and V 2p spectra of all catalysts obtained by sol-gel method.

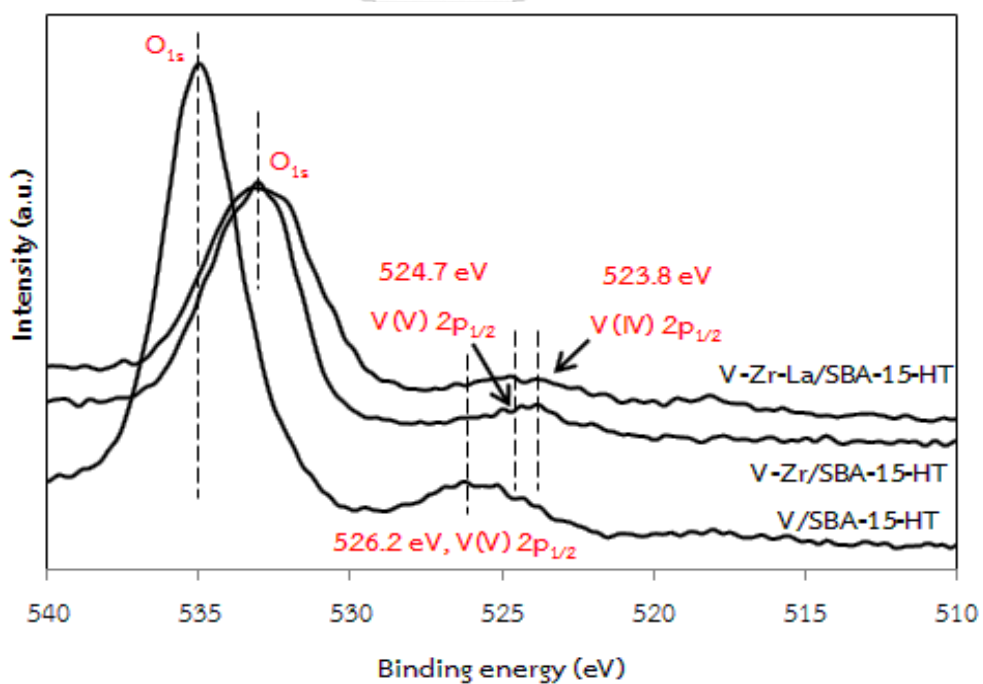


Figure 4.43 XPS spectra for O 1s and V 2p spectra of all catalysts obtained by hydrothermal method.

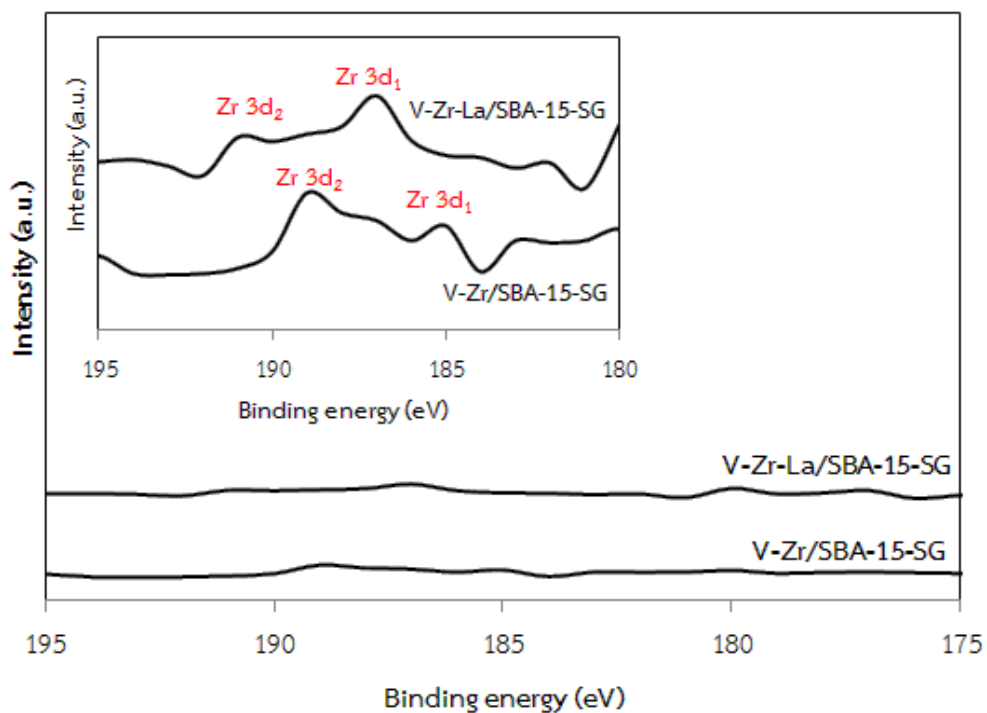


Figure 4.44 XPS spectra for Zr 3d spectra of all catalysts obtained by sol-gel method.

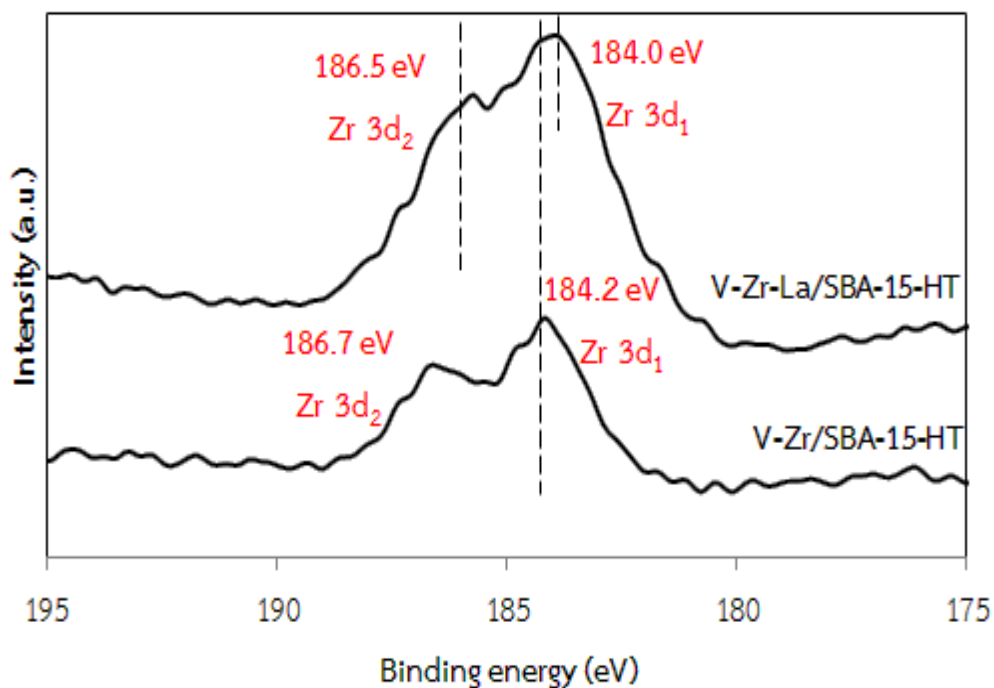


Figure 4.45 XPS spectra for Zr 3d spectra of all catalysts obtained by hydrothermal method.

4.3.1.7 Scanning electron microscope and energy dispersive X-ray spectroscopy (SEM/EDX)

The SEM images of all SBA-15 catalysts show lenticular particles of approx. 1-2 μm in diameter with an ordered porous structure of a typical SBA-15 material. The SEM images of SBA-15 catalysts with 2 wt% of vanadium are presented in **Figure 4.46**. The structure of SBA-15 synthesized by sol-gel method shows the typical worm-like morphology of SBA-15 with pores directed to longer axis of the particle relatively uniform grains. For those catalysts synthesized by hydrothermal method, especially for V-Zr/SBA-15-HT and V-Zr-La/SBA-15-HT, some surface probably due to a disordered form by hydrothermal method preparation (high pressure, 30 Bar) leads to the aggregates spherical particles of ca. 20-30 nm in diameter, which is similar to earlier reports [113]. For V/SBA-15-HT, the hexagonal prismatic morphology still remains, but the aggregation of primary particle was formed. This result will be ascribed and obviously seen by TEM results. It is clearly seen that the presence of vanadium in different SBA-15 was no significant change in the morphology of catalysts. In addition, impregnation method did not lead to any important change of the structure of the prepared catalysts.

The micro-analytical data of dispersive X-ray spectroscopy (EDX) by SEM was also conducted in order to study the chemical distribution. The typical EDX mappings of V-Zr-La/SBA-15-SG and V-Zr-La/SBA-15-HT catalysts are shown in **Figure 4.47**. The amounts of V, Zr, La, O and Si are observed (**Appendix B (Table B.1)**). The results show that the vanadium catalysts obtained by hydrothermal method exhibits a higher deviation of V concentration values (1.9-2.9 wt %) compared with the ones obtained by sol-gel method (1.7-2.2 wt %), probably owing to higher active phase concentration dispersed at the surface of SBA-15 [155]. However, the element concentration from the EDX analysis, which is not a bulk (but rather surface)

analytical tool, gives information down to a depth of approximately 2-5 microns from the typical external granule [156].

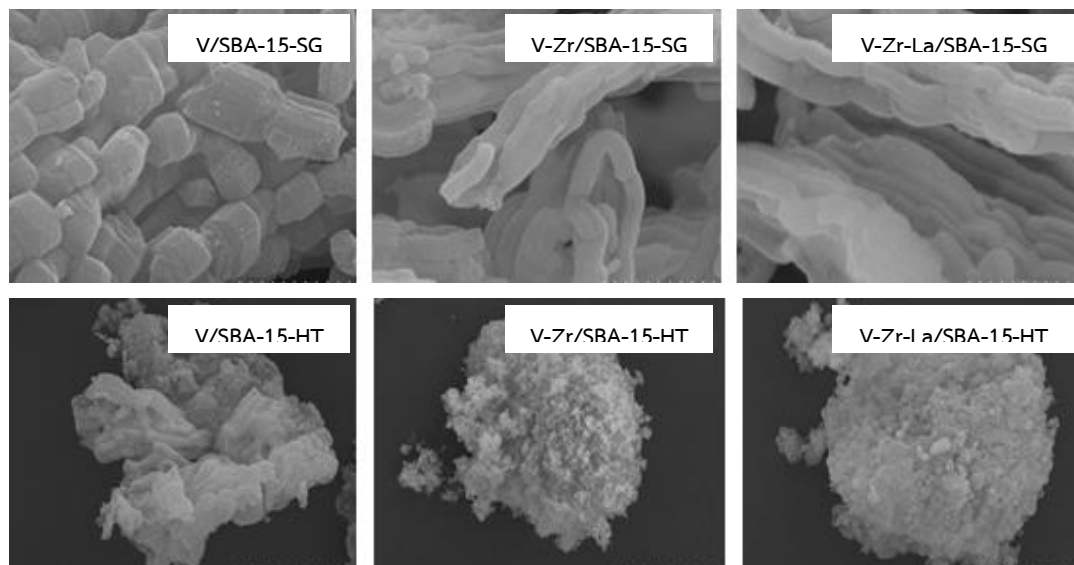


Figure 4.46 SEM images of all catalysts obtained from the sol-gel and hydrothermal methods.

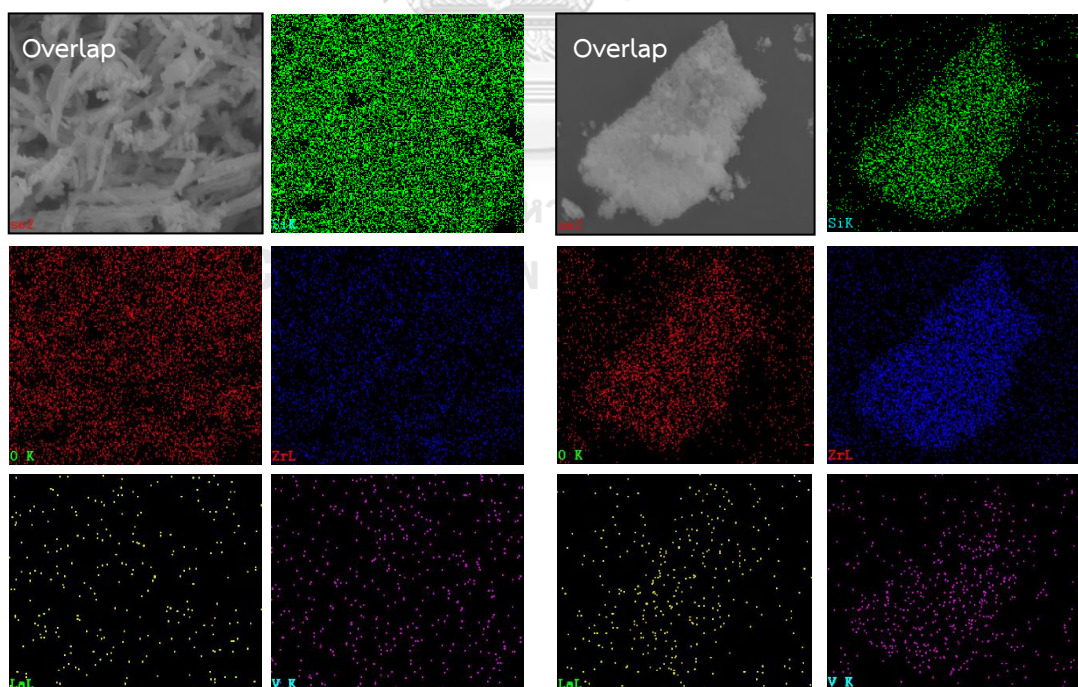


Figure 4.47 The typical SEM-EDX elemental mapping of V-Zr-La/SBA-15-SG (**left**) and V-Zr-La/SBA-15-HT (**right**) catalysts.

4.3.1.8 Transmission electron microscopy (TEM) and energy dispersive X-ray spectroscopy (EDX)

TEM images (**Figure 4.48**) reveal that the catalysts obtained by sol-gel method exhibit the hexagonal ordered structure without significant change after vanadium oxide loaded into the channels. For V-Zr/SBA-15-HT and V-Zr-La/SBA-15-HT, they clearly indicated the catalysts without well-ordered hexagonal mesopores suggesting that the framework of hexagonal ordering was not preserved after used high temperature and high pressure by this hydrothermal method. In the TEM image of V/SBA-15-HT, the uniform hexagonal mesostructured pores still remained, but the partially structural collapse of the SBA-15 ordered mesoporous after incorporation of V_2O_5 was evident. It should be emphasized that the weak bond strength and low electron density of mono-metallic with SBA-15 supported catalyst (V/SBA-15-HT) cause the formation of blocked pores (vanadium precursor) easily to rule out in the last step of calcination process, which is consistent with the results obtained from XRD.

TEM with the electron diffraction mode can determine the crystallographic structure of catalysts indicating the metal completely bonded with SBA-15 framework. From the electron diffraction results (**Figure 4.49**), it is shown that the V-Zr-La/SBA15 catalyst obtained by hydrothermal method were polycrystalline (**Figure 4.49b**). In a structure like this, a number of single crystals are held together by a layer of amorphous solids. This is because it does not have long range ordered arrangement of atoms, molecules or ions within the structure [157]. Therefore, in a polycrystalline structure, the long-range order has been disrupted. On the other hand, the ones obtained from sol-gel were amorphous material contains a hollow (white) and no diffraction rings otherwise crystalline material (**Figure 4.49a**). The long-range order has been uniformed. The results were in agreement with those obtained by low-angle XRD presented in **Figure 4.26** and **Figure 4.28**. The particle is clearly

observed in SEM image (**Figure 4.46**). In addition, Raman spectroscopy (**Figure 4.36-4.37**) may also be useful, as the vibrational modes of amorphous silica and the crystalline modification are different.

In order to confirm the presence of both V species and other metal species in the catalyst surface, an energy dispersive X-ray spectroscopy (EDX) mapping by TEM analysis of the sample was conducted (**Figure 4.50**). The EDX spectrum shows the presence of V, Zr, La, O and Si (C and Cu are associated with the grid and the dispersion medium, respectively). The mapping images were acquired using the L-line spectra of the elements. The overlap image (sum spectrum) is also shown. The results confirmed that vanadium and other metal species exist in the internal pore of the catalyst. However, it should be mentioned that the vanadium species content was only 2 wt%, but from the spectroscopy (**Appendix B (Table B.2)**), the content of vanadium species of catalyst (3.9 wt%, V-Zr-La/SBA-15-HT) seemed to be higher than that of the one obtained by sol-gel method (1.3 wt%, V-Zr-La/SBA-15-SG). The possible explanation for the observed course of the vanadium species tends to be concentrated on the internal pore of the SBA-15 (-HT methods) owing to its lower specific surface energy than that of the catalyst obtained by sol-gel method [158].

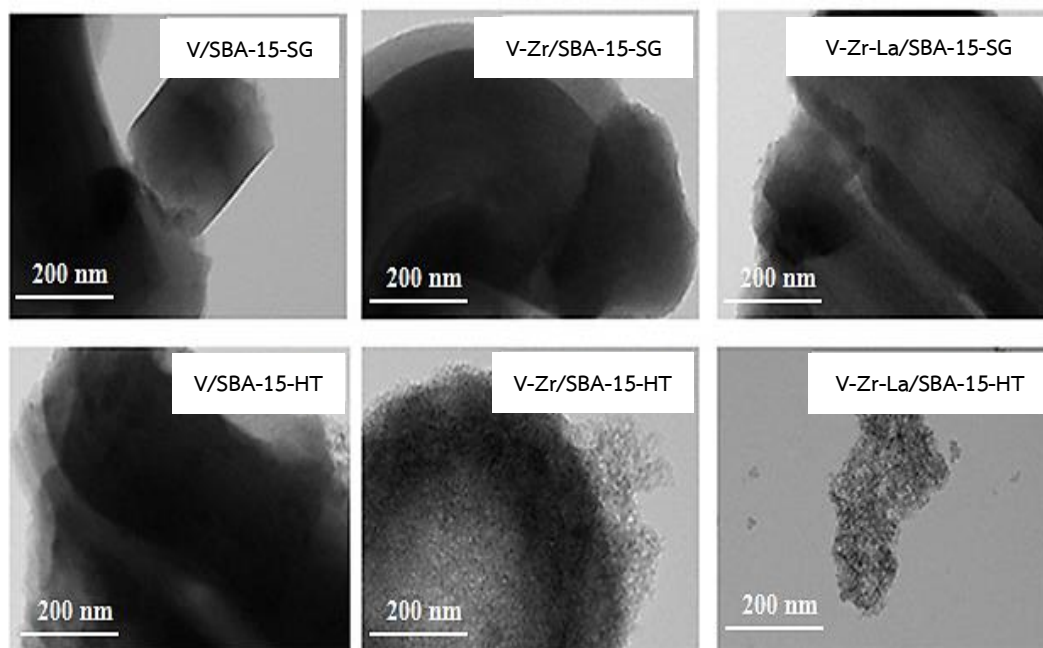


Figure 4.48 TEM micrographs of all catalysts obtained from the sol-gel and hydrothermal methods.

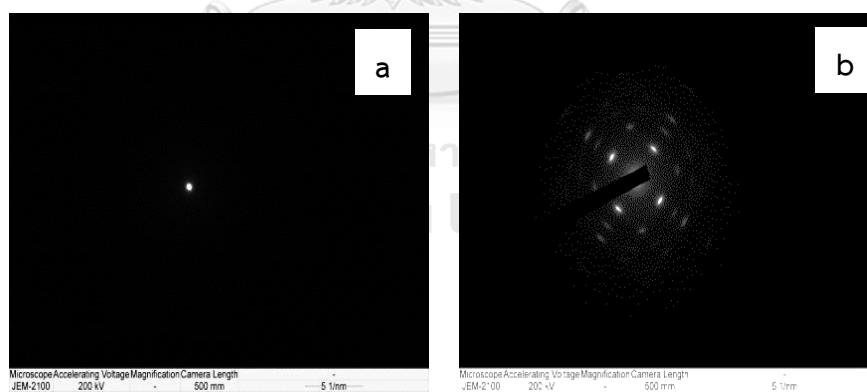


Figure 4.49 TEM micrographs of nanoscale V-Zr-La/SBA-15 (-SG (Figure 4.49a) and -HT (Figure 4.49b)) catalysts with electron diffraction mode.

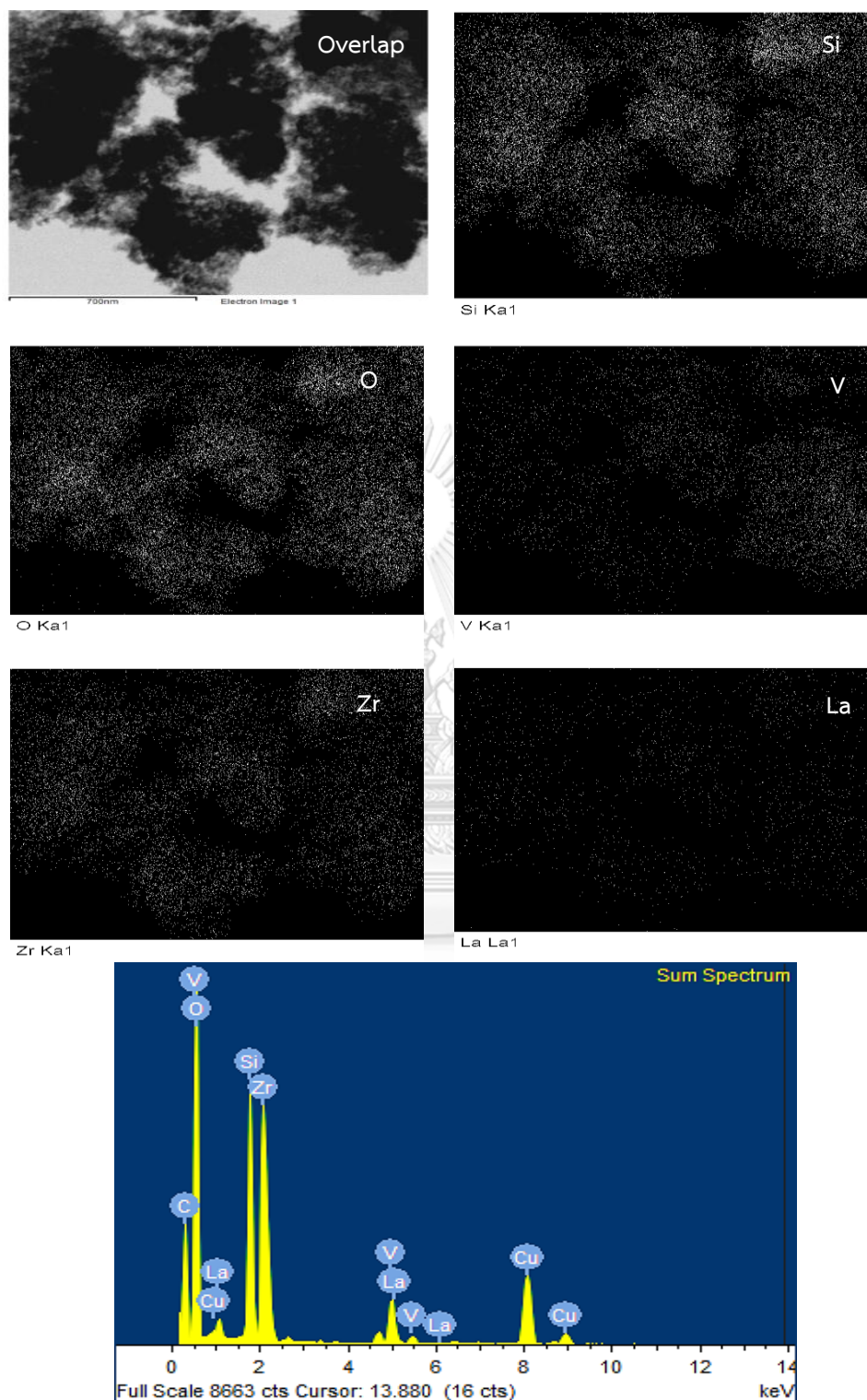


Figure 4.50 The typical TEM-EDX elemental mapping and EDX of the plotted area of V-Zr-La/SBA-15-HT catalyst.

4.3.1.9 Carbon dioxide Temperature-Programmed Desorption (CO₂-TPD)

CO₂-TPD experiments (**Figure 4.51**) were performed to measure the basicity of all catalysts. Using the calibration factor, the integrated CO₂ desorption curve could be converted into moles of CO₂ eluded [103]. Based on CO₂ desorption peaks, the weak basic sites, moderate basic sites and strong basic sites can be identified. Three different regions of CO₂ desorption can be distinguished, where the CO₂-TPD profiles occur at low desorption temperature near 100°C corresponding to CO₂ from bicarbonate species, which is formed by the reaction of CO₂ with OH groups adsorbed on the weak basic site [159]. While the medium (150°C) and high (245°C) desorption temperature can be ascribed to the desorption of bidentate carbonate species formed with metal–oxygen pairs interaction on the medium (Mⁿ⁺–O²⁻ pair site) and strong (O²⁻ ions) [160-162]. The catalysts obtained by sol-gel method exhibit very low-temperature desorption peak centered at about 100°C or seem to disappear desorption peak. This is because vanadium oxide accumulated on the external surface of SBA-15 as described in N₂ physisorption, resulting in the reduction of the bond strength between metal and support as well as the basic sites. Therefore, the number of basic sites is perhaps ascribed to affect by surface area. It is clear that the catalysts (-SG) had much lower value of basic site. Contrarily, the TPD profiles of the ones obtained by hydrothermal method, especially for V-Zr/SBA-15-HT and V-Zr-La/SBA-15-HT were obviously observed with the strong intensity of desorption peak. It can be clearly seen that those catalysts provide the highest value of basic site. The amount of CO₂ desorbed from the supports decreases in the following sequence: V-Zr-La/SBA-15-HT (37.1 μmole CO₂/g) > V-Zr/SBA-15-HT (30.3 μmole CO₂/g) > V/SBA-15-HT (13.9 μmole CO₂/g) > V-Zr-La/SBA-15-SG (7.2 μmole CO₂/g) > V-Zr/SBA-15-SG (6.1 μmole CO₂/g) > V/SBA-15-SG (4.4 μmole CO₂/g) (see **Table 4.6**). The order follows the basicity of the supports. The larger CO₂ amount in the case of the catalysts obtained by hydrothermal method can be attributed to much strong bond

strength and high electron density of tri-metallic (V-Zr-La) incomparable with the catalysts obtained by sol-gel method. This was in accordance with the highest catalytic activity. Hence, the TPD profiles varied greatly in catalysts synthesized by hydrothermal method.

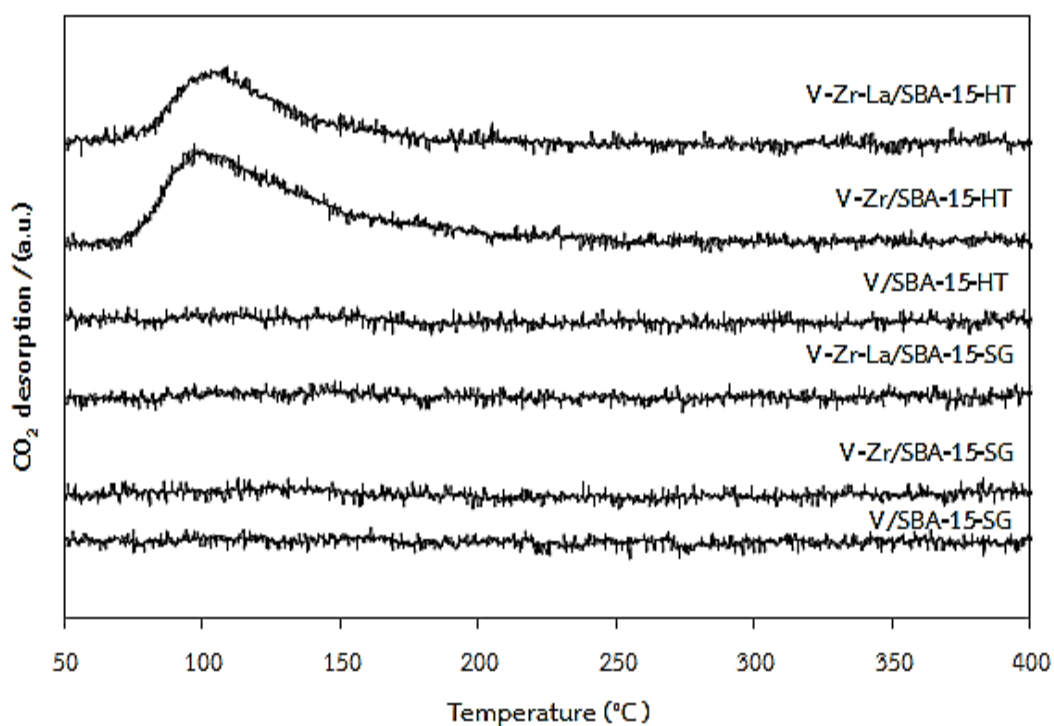


Figure 4.51 CO₂-TPD profiles of all prepared catalysts.

Table 4.6 The surface basicity of all catalysts from CO₂-TPD.

Samples	Number of basic site ($\mu\text{mole CO}_2/\text{g cat.}$)		
	Weak basic site	Medium-to-Strong basic site	Total basic sites
V/SBA-15-SG	-	-	4.4
V-Zr/SBA-15-SG	-	-	6.1
V-Zr-La/SBA-15-SG	-	-	7.2
V/SBA-15-HT	-	-	13.9
V-Zr/SBA-15-HT	19.9	10.4	30.3
V-Zr-La/SBA-15-HT	24.6	12.5	37.1

4.3.2 Catalytic properties

4.3.2.1 Non-oxidative dehydrogenation reaction

Figure 4.52 and **Figure 4.53** display the ethanol conversion and product selectivity as a function of reaction temperature for all catalysts in non-oxidative dehydrogenation. The reaction temperature is usually a driving force to improve catalytic conversion of endothermic reaction. The catalyst basicity and molecular structures formed at the surface of the support oxide (VO_x species) are also the important factor influencing on the reaction activity. In **Figure 4.52(a)** and **4.53(a)**, the temperature dependence of ethanol conversion of both catalysts obtained by the sol-gel and hydrothermal methods is presented for dehydrogenation conditions. Beginning with the reaction temperature of 150°C, the conversion continuously increased as the raising in temperature from 200 to 400°C. For instance, the presence of V-Zr-La/SBA-15-HT results in a strong increase of the conversion (80%) at 400°C

among other catalysts. The increasing of conversion associated with the endothermic behavior of dehydrogenation reaction that needs high temperatures to secure reasonable of products. A further incorporation of the vanadium oxide from bi-metallic (V-Zr) to tri-metallic (V-Zr-La) results in an increase of ethanol conversion from 72% to 78% and 63% to 80% at 400 °C for the catalysts obtained by sol-gel and hydrothermal methods, respectively. Based on the results of CO₂-TPD, it seems to have a relationship between the activity and the weak basic sites of all catalysts. As seen, the catalyst possessing higher number of weak basic sites showed better catalytic activity on ethanol dehydrogenation.

Figure 4.52(b) and **4.53(b)** show the selectivities of byproduct for the catalysts obtained by sol-gel and hydrothermal methods as a function of reaction temperature. The acetaldehyde selectivity for all catalysts decreases with rising in the reaction temperature as well as diethyl ether (DEE). The subsequent decrease in acetaldehyde selectivity was associated with formation of ethylene on acidic species of SBA-15 silica surface. It also represents clearly that all SBA-15 catalysts (HT) was significantly higher (acetaldehyde selectivity) in comparison with the ones obtained by sol-gel method. At the highest reaction temperature (400°C), the V-Zr-La/SBA-15-HT catalyst showed selectivity of acetaldehyde as high as approximately 48%. The catalysts obtained by sol-gel represents the lowest selectivity of acetaldehyde about 24-33% at 400 °C. These results indicate that the using of vanadium speciation (VO_x species) in SBA-15 supported catalyst obtained by both methods affects the rates of dehydrogenation and dehydration of ethanol [82].

The ethanol conversion and product selectivities agree with the characterization results from various techniques (such as Raman spectra, XPS, UV-Vis, CO₂-TPD, etc.) leading to enhance the catalytic activity and selectivities in this reaction. However, more details about the role of all catalysts will be discussed in **section 4.3.2.2** Considering the acetaldehyde yield (product of ethanol conversion and acetaldehyde selectivity) for each catalysts obtained by non-oxidative dehydrogenation as shown in **Figure 4.54 (a and b)**, it increased with increasing reaction temperature up to 400°C. At this temperature, the highest acetaldehyde yield reached 38.0% with 40.7% of ethylene yield (not shown data) and slight amount of DEE (0.8%) were obtained from the V-Zr-La/SBA-15-HT catalyst. We suggest that the weak Brønsted acid sites from SBA-15 supported catalysts (Zr/SBA-15 and Zr-La/SBA-15) also promote the dehydration of ethanol to ethylene. However, they do not further influence the dehydrogenation route. This result agrees with the concept that dehydrogenation is catalyzed by Si-O-Si sites of the SBA-15 surface [21, 22, 82, 163].

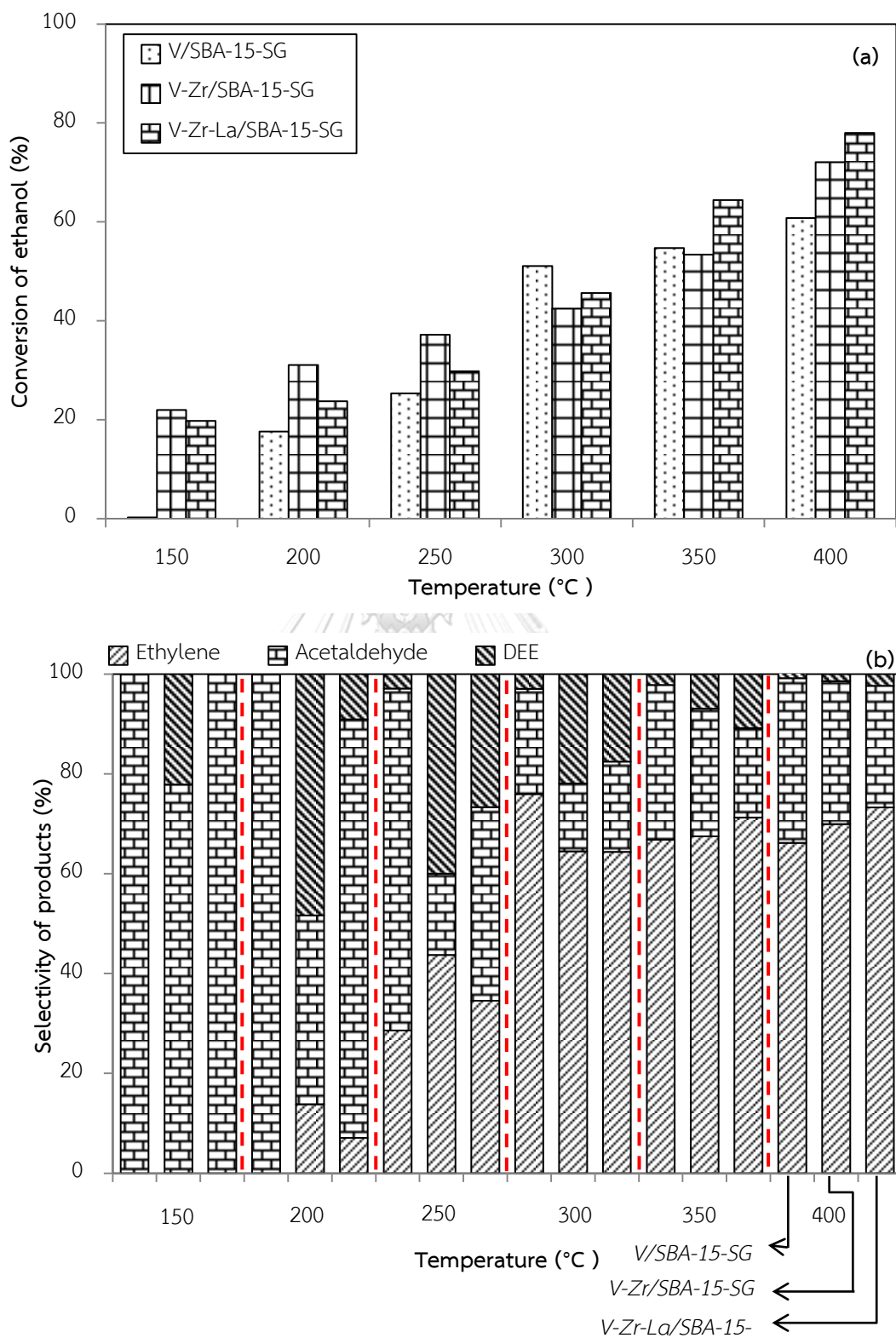


Figure 4.52 Conversion (a) and selectivity (b) of different VO_x/SBA-15 catalysts (SG) in non-oxidative dehydrogenation.

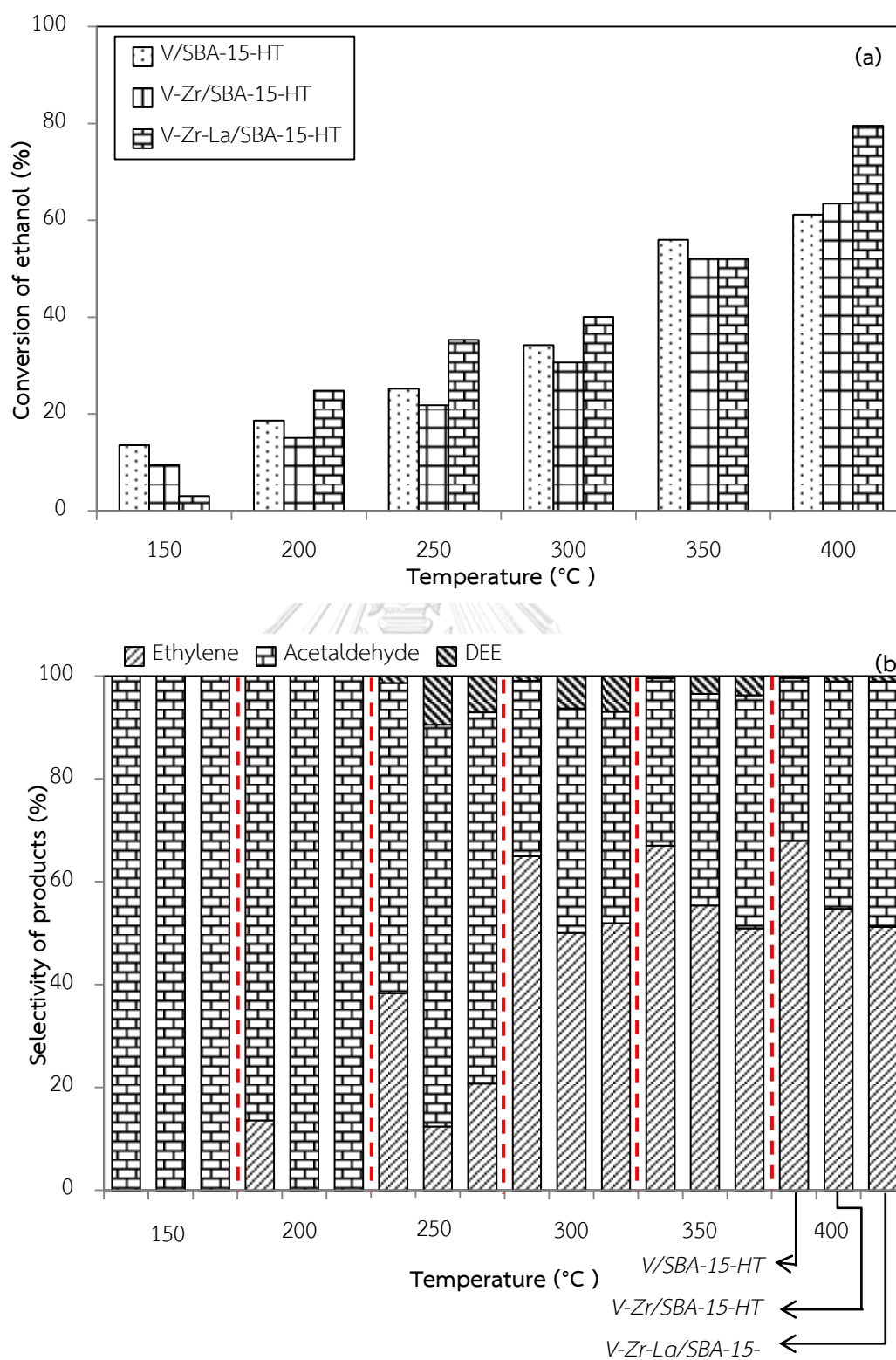


Figure 4.53 Conversion (a) and selectivity (b) of different VO_x/SBA-15 catalysts (HT) in non-oxidative dehydrogenation.

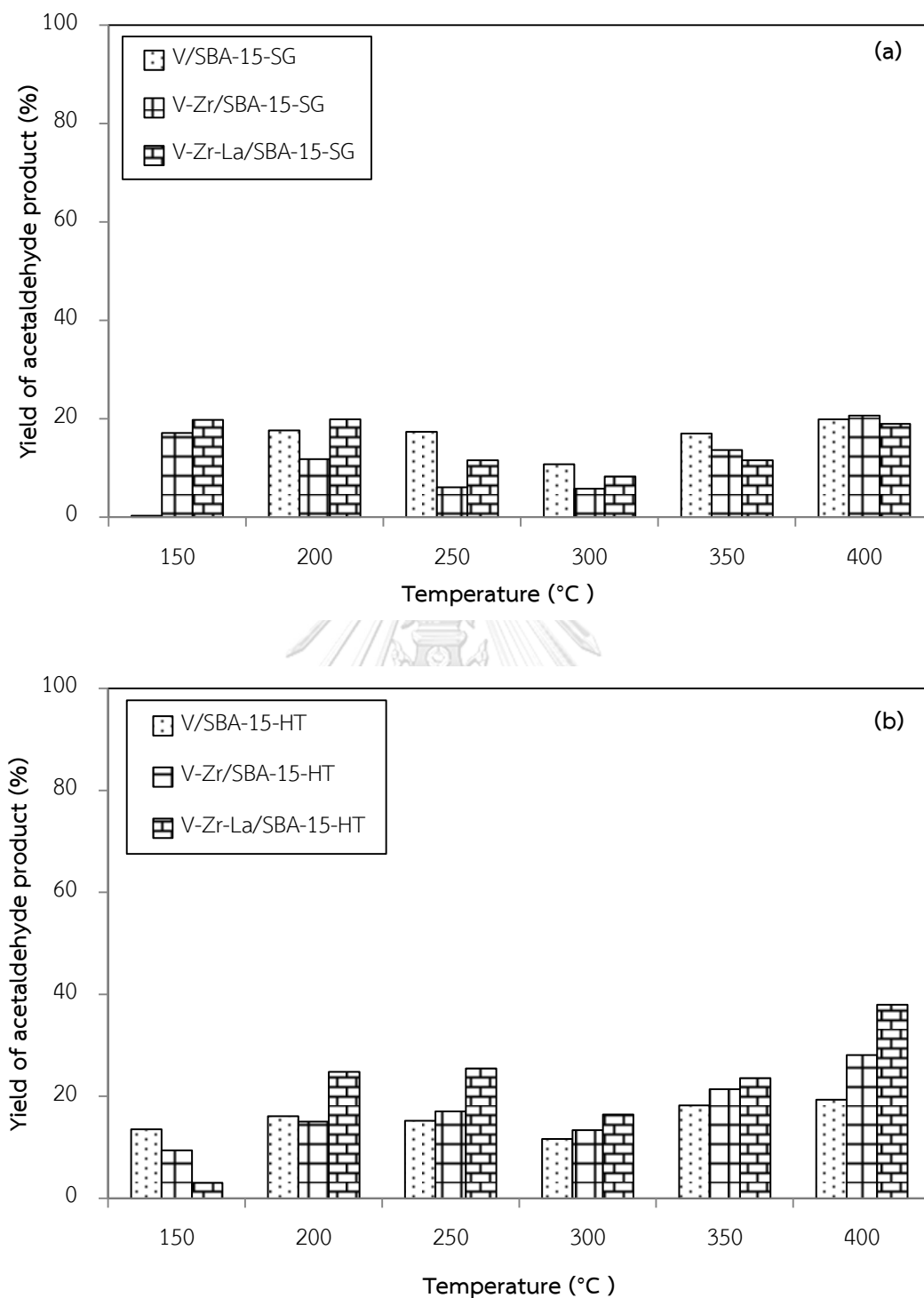


Figure 4.54 Yield of acetaldehyde product obtained from non-oxidative dehydrogenation reaction over different VO_x/SBA-15 catalysts synthesized by sol-gel (a) and hydrothermal (b) method.

4.3.2.2 Oxidative dehydrogenation reaction

In order to determine the catalytic behaviors of all catalysts, the conversion of ethanol and the selectivity to products such as acetaldehyde, carbon monoxide and carbon dioxide as a function of temperature were investigated in vapor phase oxidative dehydrogenation of ethanol (2 vol% O₂). The oxidative dehydrogenation activity is apparently significant at ca. 150°C and total at 400°C as shown in **Figure 4.55(a)** and **Figure 4.56(a)**. The increased temperature apparently resulted in an increase in ethanol conversion of both catalysts obtained by the sol-gel and hydrothermal methods, reaching ca. 98% for the V-Zr-La/SBA-15-HT at 300°C under the investigated conditions. It can be observed that the catalytic activity of the catalysts obtained by hydrothermal method exhibited remarkably higher catalytic activity than the ones obtained by the sol-gel method. The ethanol conversion was found to be in the order of V-Zr-La/SBA-15-HT > V-Zr/SBA-15-HT > V/SBA-15-HT. It is suggested that the incorporation of vanadium into the framework of SBA-15 is responsible for the formation of basic sites and VO_x species. In particular, the catalysts (HT) that could allow the metal oxide (vanadium) to easily incorporated into the surface channels of SBA-15, result in increased bond strength between metal and support, promoting the weak basic sites (**Figure 4.51**) and forming the isolated monomeric VO_x or VO₄³⁻ species (**Figure 4.37**). Weckhuysen and Keller [80] reported that the incorporation of vanadium allows probing the electronic density on the vanadium in supported vanadium oxide catalysts as a function of the support oxide. It was found that the electron density on vanadium increases when incorporated with other metal oxides such as V/Al₂O₃, V/ZrO₂, V/Nb₂O₅, etc. The high electron density of the vanadium facilitates the rate-determining breaking step in the V–O–CH₂CH₃ (vanadium ethoxy) reaction intermediate during ethanol oxidation and acetaldehyde desorbs, which can be referred as the catalytically active site. In the high reaction temperatures, i.e. ca. 300 to 400°C, the ethanol conversion of all

catalysts obtained by hydrothermal method (V-Zr/SBA-15-HT and V-Zr-La/SBA-15-HT) are quite similar around 83–90%, 91–94%, and 90–98% at 300, 350, and 400°C, respectively, whereas V/SBA-15 (–SG and –HT) gave the lowest value of ethanol conversion.

The conversion of the feed and the selectivity to the corresponding carbonyl compound are also important for assessment of the oxidative dehydrogenation catalyst. As shown in **Figure 4.55(b)** and **4.56(b)**, acetaldehyde was a major product with the temperature up to ca. 150–300°C. The major unselective product was ethylene and diethyl ether, which is associated with the presence of some surface acid sites at the catalyst surface. In addition, a rapid drop of acetaldehyde selectivity for the catalysts obtained by hydrothermal method was observed along with increased amounts of carbon oxide (CO and CO₂). In fact, it decreased with increased temperature (above 250°C) due to the deep oxidation of intermediates in the oxidative dehydrogenation products [164]. Generally, the CO_x selectivity for the catalysts obtained by hydrothermal method is much higher (even more than 6 times) than that for the catalysts obtained by sol-gel method. This trend of selectivity suggested that the catalysts obtained by hydrothermal method can produce higher amount of the desired product (acetaldehyde) than the ones obtained by sol-gel method. The DEE selectivity for the catalysts obtained by hydrothermal method was lower than that for the catalysts obtained by sol-gel method for every reaction temperature. These findings confirm that oxygen promote the dehydrogenation pathway. Besides, addition of oxygen was found to increase the rate constant of oxidative dehydrogenation reaction over silica as reported by Yao et al. [165]. According to the acetaldehyde yields for all catalysts obtained by oxidative dehydrogenation reaction, they are shown in **Figure 4.57 (a and b)**. The yields of acetaldehyde accrue in the temperature of 200 to 300°C. Among all catalysts, V-Zr-La/SBA-15-HT exhibits the outstanding performance that gives the highest value for

acetaldehyde yield of 40% at 300°C. Moreover, the acetaldehyde yields in oxidative dehydrogenation are much higher than those found in non-oxidative dehydrogenation reaction. In addition, the bonding of oxygen may also initiate in the reductive elimination of adsorbed ethoxy species to acetaldehyde by water formation [166]. These results show that with the incorporation of V in the SBA-15 supported catalysts (-SG and -HT) and controlling the oxygen content in the feed, one may selectively convert ethanol to acetaldehyde or ethylene with desired conversion and selectivity.

Correlating these findings with the characterization data, we conclude that the active species for non-oxidative dehydrogenation and oxidative dehydrogenation reaction such as basic sites, vanadium or VO_x species on the surface and other techniques are crucial. From **Figure 4.40-4.45**, we are able to find that the oxidation states of vanadium species for all catalysts with higher valence state are generally relevant to higher activity and selectivity. Zhang et al. [167] reported that, in the oxidative dehydrogenation of methanol to formaldehyde, V^{4+} species seem to be more selective to formaldehyde, although less active, than V^{5+} species, due to its lower oxidation potential. The main oxidation states related to this reaction are V^{+4} and V^{+5} . In fact, V^{+5} can be present in tetrahedral (VO_4), pentahedral (VO_5) and octahedral (VO_6) coordination environment and tends to form polyoxoanions, while V^{+4} is also stable and mostly present in square pyramidal or pseudo-octahedral coordination as an isolated cation [80]. Therefore, the catalysts obtained by hydrothermal method, especially for the V-Zr-La/SBA-15-HT catalyst, it shows both high ethanol conversion and high acetaldehyde selectivity in non-oxidative dehydrogenation and oxidative dehydrogenation reaction. From the results of Raman spectroscopy (**Figure 4.36-4.37**) and UV-vis (**Figure 4.38-4.39**) studies, we know that the amount of isolated or monomeric VO_x species ($\text{V}=\text{O}$) in the catalysts (HT) are higher than the ones obtained by sol-gel method. Many authors [80, 137, 168] have

convinced that this bond contains the oxygen critical participate for alcohol oxidation (such as ethanol, methanol, glycerol, etc.). In addition, the amount of aggregated or oligomeric VO_x species (V–O–V bridges) in the catalysts (SG) is predominant on the catalyst surface. Besides, the basicity of catalyst surface needs to be considered. Basically, the dehydrogenation of ethanol to produce acetaldehyde greatly depends on the basic sites of catalyst [169]. This indicated that most effective catalyst (–HT) contained mostly the weak basic sites. In fact, it should be noted that the catalysts (–SG) showed very low amount of total basic sites (4.4-7.2 $\mu\text{mole CO}_2/\text{g cat.}$), but significantly affected the catalytic activity. Therefore, the catalytic activity should not totally depend on the basic sites of the catalyst. In utilization, the vanadium species, particularly the V^{4+} species that consisted of V=O (monomeric vanadium or VO_x species) as well as the basicity of catalyst played a more important role in the non-oxidative dehydrogenation and oxidative dehydrogenation of ethanol to acetaldehyde.

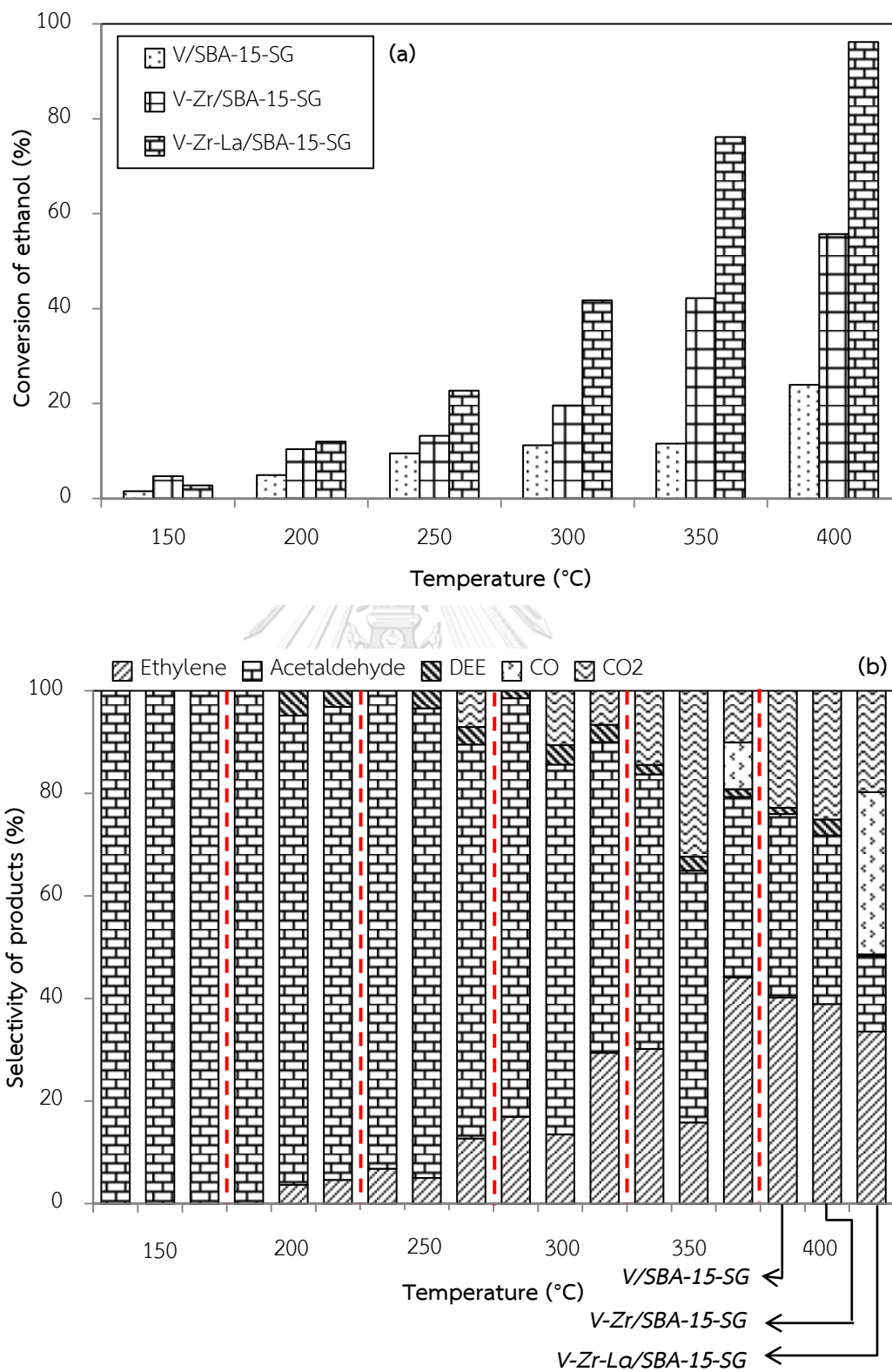


Figure 4.55 Conversion (a) and selectivity (b) of different VO_x/SBA-15 catalysts (SG) in oxidative dehydrogenation.

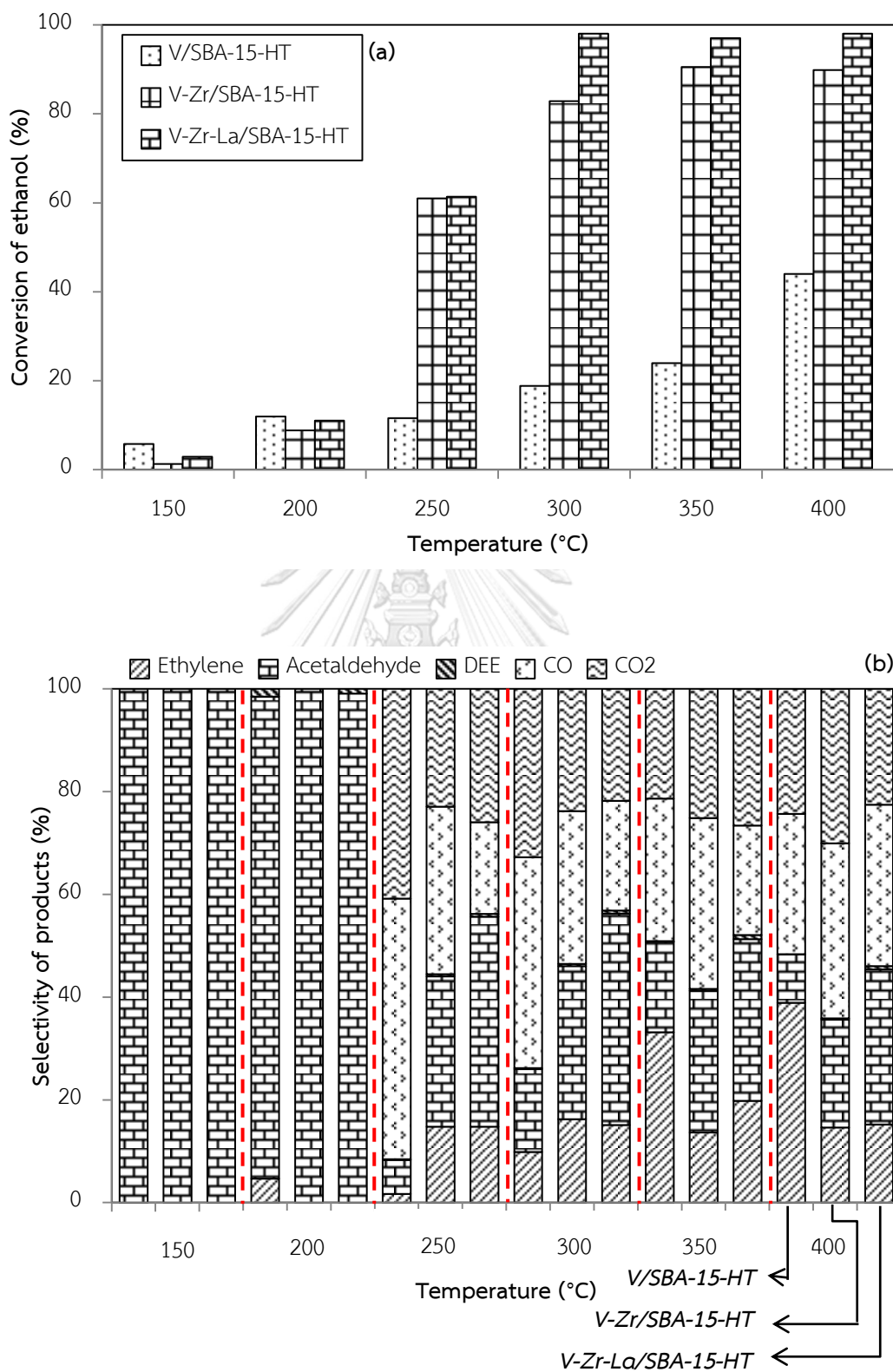


Figure 4.56 Conversion (a) and selectivity (b) of different VO_x/SBA-15 catalysts (HT) in oxidative dehydrogenation.

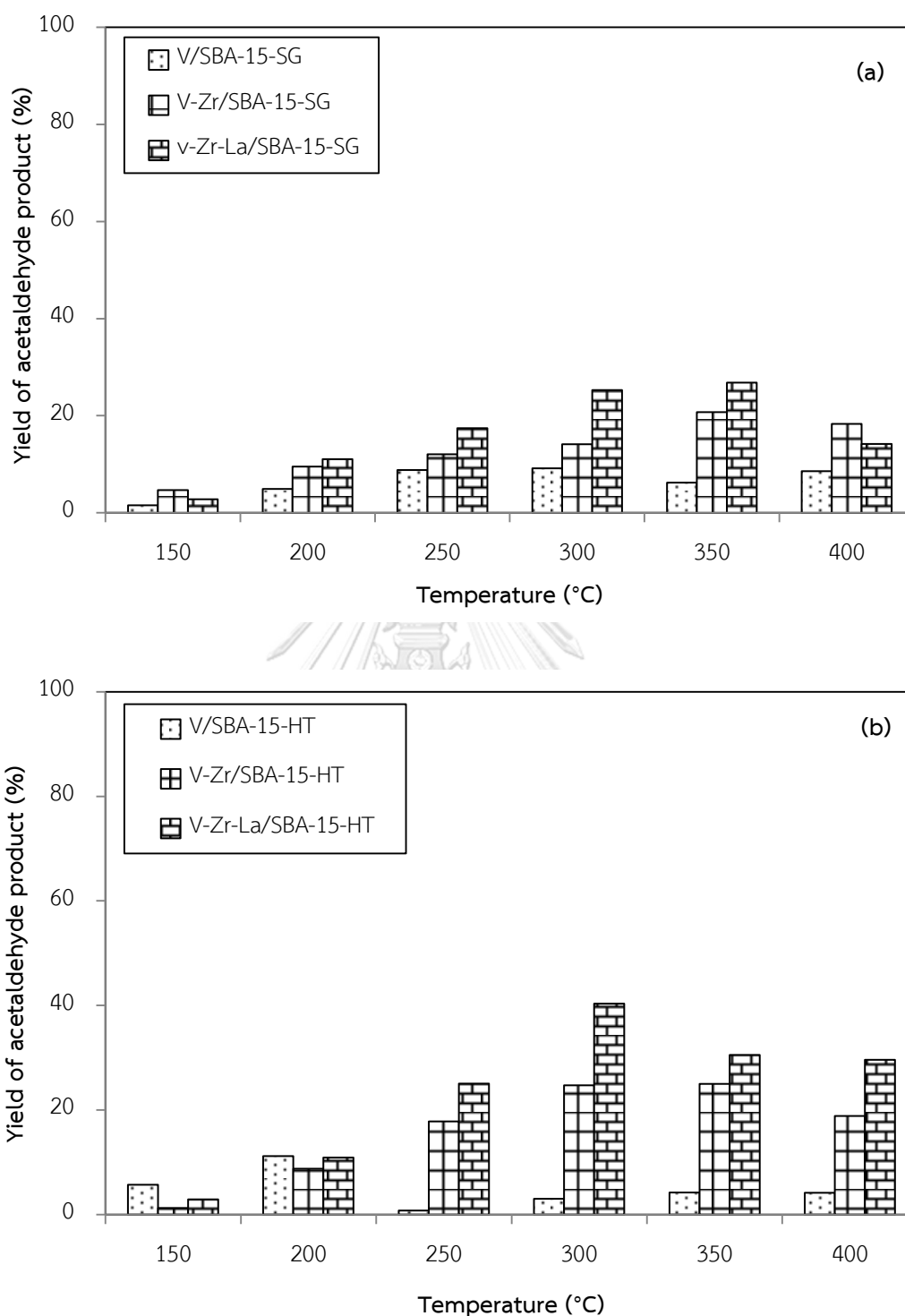


Figure 4.57 Yield of acetaldehyde product obtained from oxidative dehydrogenation reaction over different VO_x/SBA-15 catalysts synthesized by sol-gel **(a)** and hydrothermal **(b)** method.

4.3.3 Characterization of spent catalysts after reaction

During the transformation of organic compounds over solid basic catalysts, there is always formation and retention of heavy side-products, either in the pores or on the external surface [170]. Deactivation of the catalysts occur as a result of; coke, contamination on active sites, agglomeration and catalyst poisoning [171]. Therefore, the carbon deposition on catalyst surface was studied and determined through the morphology and elemental distribution over the catalyst surface by SEM-EDX technique. **Figure 4.58** shows the SEM images of spent catalysts from non-oxidative dehydrogenation and oxidative dehydrogenation reactions respectively in temperature program between 150-400°C and **Table 4.7** shows the relative percentage of element distribution and coke deposition in spent catalysts. A fine porous type dispersion of the mixture of V, Zr and La is observed in the fresh (V-Zr-La/SBA-15-HT) catalyst (**Figure 4.58 (a)**) and it is difficult to distinguish V, Zr and La in the composite. The spent catalysts from non-oxidative dehydrogenation reaction show some darker shades as compared to the fresh catalysts, where the surfaces are brighter. Filament like deposited carbon species are observed in this catalyst [172], as marked by circles (**Figure 4.58(b)-(c)**). This can be assigned to the formation of carbon deposition during ethanol dehydrogenation reaction. From **Table 4.7**, the different VOx/SBA-15 catalysts obtained from non-oxidative dehydrogenation reaction undoubtedly has the highest carbon content compared to the different VOx/SBA-15 catalysts obtained from oxidative dehydrogenation reaction, which is 3.1-7.0 wt%. This suggests that less carbon was deposited on the oxidative dehydrogenation reaction compared to different VOx/SBA-15 catalysts obtained from non-oxidative dehydrogenation reaction as also further corroborated by the SEM-EDX analysis of the spent catalysts. Therefore, the results showed that the presence of oxygen can prevent the coke formation by carbon blocking the active surface that conclude from lowest coke formation of only 7.0 wt% of V-Zr-La/SBA-15-HT (optimal catalyst) in

oxidative dehydrogenation reaction. In addition, the EDX study of different VOx/SBA-15 catalysts synthesized by sol-gel and hydrothermal methods confirm that there was no significant change in the metal (V, Zr and La) distribution after the reaction.

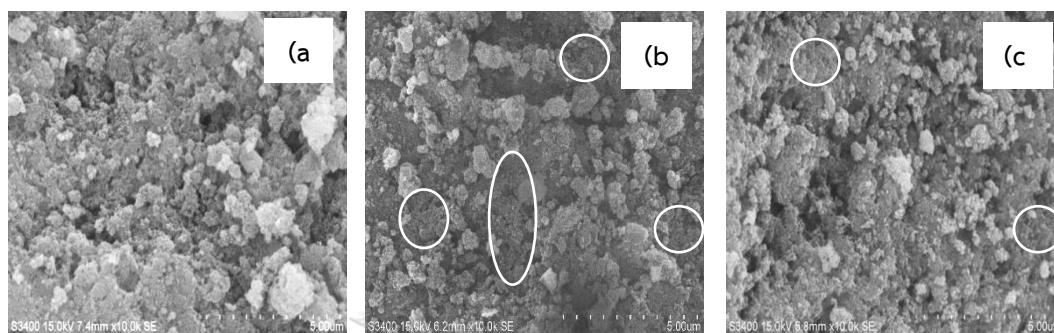


Figure 4.58 SEM images of fresh catalyst (a) and spent catalyst of V-Zr-La/SBA-15-HT from non-oxidative dehydrogenation (b) and oxidative dehydrogenation (c) reaction respectively.

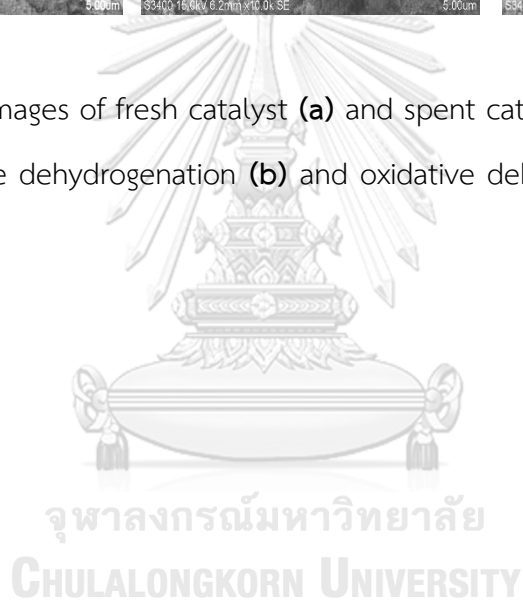


Table 4.7 Relative percentage of elements distribution in spent catalysts obtained from non-oxidative dehydrogenation and oxidative dehydrogenation reaction.

Catalysts	Amount of weight on surface (wt%)					
	Si	O	Zr	La	V	C
Non-oxidative dehydrogenation						
V/SBA-15-SG	53.8	39.3	0	0	1.7	5.2
V-Zr/SBA-15-SG	42.2	31.6	17.4	0	1.9	6.9
V-Zr-La/SBA-15-SG	44.3	32.8	13.9	0.4	2.2	6.4
V/SBA-15-HT	56.6	31.5	0	0	2.2	9.6
V-Zr/SBA-15-HT	17.5	23.1	43.2	0	2.3	13.9
V-Zr-La/SBA-15-HT	17.9	14.1	51.7	4.6	2.2	9.3
Oxidative dehydrogenation						
V/SBA-15-SG	60.7	34.4	0	0	1.8	3.1
V-Zr/SBA-15-SG	43.6	34.0	16.4	0	2.4	3.6
V-Zr-La/SBA-15-SG	48.1	24.5	17.9	1.1	2.5	5.9
V/SBA-15-HT	62.7	30.6	0	0	1.5	5.3
V-Zr/SBA-15-HT	16.8	30.3	45.2	0	2.2	5.5
V-Zr-La/SBA-15-HT	14.1	12.6	59.7	5.2	1.4	7.0

CHAPTER V

CONCLUSION AND RECOMMENDATIONS

5.1 Conclusion

In the first part of this work, zirconium (Zr) and bimetal (Zr and La) containing mesoporous silicas (SBA-15) were synthesized by conventional sol-gel and one-step hydrothermal methods without addition of hydrochloric acid. The influence of synthesis method on the structure and characteristics of these materials has been investigated. It appears that the catalysts obtained by the sol-gel method retain the two-dimensional hexagonal order structure of siliceous SBA-15 material. In contrast to catalysts obtained by the hydrothermal method, the characteristic diffraction peak was slightly changed in the intensity with a pore system lacking long-range order. The incorporation of Zr and bimetal (Zr and La) had an effect on the textural properties for both methods. For those catalysts synthesized by sol-gel method, they consisted of agglomerated particles with primarily irregular shape with the metal oxide located on the external surfaces. For catalysts synthesized by hydrothermal method, the agglomeration of primary particles altered the porous shape. Besides, this hydrothermal method still had some outstanding advantages, such as environmental friendly with avoiding of toxic reagents and making new active sites, especially Brønsted acid types. Thus, SBA-15 synthesized by both methods provided a better and more practical than the existing methodologies with their potential and better applications when acid sites are required.

In the second part, the catalytic performance for ethanol dehydration from the temperature range of 200 to 400°C over various SBA-15 catalysts prepared by sol-gel and hydrothermal methods was investigated. The method of preparation has

a significant impact on the catalytic performance, since it influences the catalyst porosity, structure and surface composition. It appears that the Zr-La/SBA-15-HT catalyst showed the highest catalytic activity with 84% conversion of ethanol and ethylene selectivity (95%) to obtain the ethylene yield of ca. 80% (at 400°C), indicating some interactions between metals (Zr and Zr-La) used with hydrothermal method, which played an important role in the ethanol dehydration. Furthermore, the present study has shown the broad distribution of acid sites (especially weak acid sites) on these catalysts that could allow them to be used for the dehydration of ethanol to ethylene.

In the third part, the catalytic performance of different VO_x/SBA-15 catalysts obtained by sol-gel and hydrothermal methods was investigated for ethanol non-oxidative dehydrogenation and oxidative dehydrogenation from the temperature range of 150 to 400°C. It was found that a variation in the VO_x species with different basicity, especially weak basic site influenced the catalytic performance of both reactions. The amounts of monomeric to oligomeric VO_x species and basic sites depend on the preparation method of catalysts. Besides, the amounts of isolated or monomeric VO_x species (V=O) in the catalysts obtained by hydrothermal method are higher than the ones obtained by sol-gel method, and more interestingly, provided an unusually high selectivity towards acetaldehyde. It appears that the V-Zr-La/SBA-15-HT catalyst showed the highest catalytic activity with 80% conversion of ethanol and acetaldehyde selectivity (48%) to obtain the acetaldehyde yield of ca. 38% at 400°C in non-oxidative dehydrogenation and 98% conversion of ethanol and acetaldehyde selectivity (41%), which gives acetaldehyde yield of ca. 40% at lower temperature (300°C) in oxidative dehydrogenation. The presence of oxygen promotes the rate of dehydrogenation reaction pathway over these catalysts. Therefore, it can be concluded that the catalytic activity should not totally depend on the basic sites

of the catalyst. In utilization, the vanadium species, particularly the V^{4+} species (as deduced from XPS data) that consisted of V=O isolated monomeric VOx species as well as the basicity of catalyst played a more important role in the non-oxidative dehydrogenation and oxidative dehydrogenation of ethanol to acetaldehyde. Although all catalysts will eventually deactivate, proper catalyst by the addition of oxygen can prevent rapid deterioration of catalytic activity.

5.2 Recommendations

1. In the further study, the IR of pyridine and pyrrole chemisorbed should be used to distinguish types of the acid and basic sites, respectively.
2. The effect of vanadium loading on the catalytic performance should be further investigated under the same experimental conditions. The obtained results should be used to deeper understand the behavior of vanadium or VOx species which was an important factor for the selectivity to acetaldehyde.
3. The X-ray absorption fine structure spectroscopy (XAFS) technique, including Extended X-ray absorption fine structure (EXAFS) and X-ray absorption near edge structure (XANES) should be further characterized to provides detailed information on the oxidation state and the coordination environment of supported vanadium oxides such as electron density of the vanadium with other metal oxides.
4. In order to apply this research to industry scale, the effect of crude distillate from the fermentation broth of the microbial production of bio-ethanol is very important for studied in these reactions.

5. The catalytic stability of all different SBA-15 catalysts obtained by sol-gel and hydrothermal methods should be further investigated in order to apply the good activity and stability catalysts to the commercial usage.



REFERENCES

1. Bridgwater, T., *Biomass for energy*. Journal of the Science of Food and Agriculture, 2006. **86**(12): p. 1755-1768.
2. Huber, G.W., S. Iborra, and A. Corma, *Synthesis of transportation fuels from biomass: chemistry, catalysts, and engineering*. Chemical reviews, 2006. **106**(9): p. 4044-4098.
3. Niven, R.K., *Ethanol in gasoline: environmental impacts and sustainability review article*. Renewable and Sustainable Energy Reviews, 2005. **9**(6): p. 535-555.
4. Gucbilmez, Y., T. Dogu, and S. Balci, *Ethylene and acetaldehyde production by selective oxidation of ethanol using mesoporous V-MCM-41 catalysts*. Industrial & engineering chemistry research, 2006. **45**(10): p. 3496-3502.
5. Haryanto, A., et al., *Current status of hydrogen production techniques by steam reforming of ethanol: a review*. Energy & Fuels, 2005. **19**(5): p. 2098-2106.
6. Mallat, T. and A. Baiker, *Oxidation of alcohols with molecular oxygen on solid catalysts*. Chemical Reviews, 2004. **104**(6): p. 3037-3058.
7. Varisli, D., T. Dogu, and G. Dogu, *Ethylene and diethyl-ether production by dehydration reaction of ethanol over different heteropolyacid catalysts*. Chemical Engineering Science, 2007. **62**(18-20): p. 5349-5352.
8. Chen, G., et al., *Catalytic dehydration of bioethanol to ethylene over TiO₂/Y-Al₂O₃ catalysts in microchannel reactors*. Catalysis Today, 2007. **125**(1-2): p. 111-119.
9. Wu, L.-P., et al., *The fabrication of TiO₂-supported zeolite with core/shell heterostructure for ethanol dehydration to ethylene*. Catalysis Communications, 2009. **11**(1): p. 67-70.
10. Mokhtar, M., S.N. Basahel, and T.T. Ali, *Ethanol to hydrocarbons using silver substituted polyoxometalates: physicochemical and catalytic study*. Journal of Industrial and Engineering Chemistry, 2014. **20**(1): p. 46-53.

11. Matachowski, L., et al., *Ecofriendly production of ethylene by dehydration of ethanol over $Ag_3PW_{12}O_{40}$ salt in nitrogen and air atmospheres*. Applied Catalysis B: Environmental, 2012. **123**: p. 448-456.
12. Phung, T.K., *Ethanol dehydration on silica-aluminas: Active sites and ethylene/diethyl ether selectivities*. Catalysis Communications, 2015. **68**: p. 110-115.
13. Phung, T.K., et al., *Tuning of product selectivity in the conversion of ethanol to hydrocarbons over H-ZSM-5 based zeolite catalysts*. Fuel Processing Technology, 2015. **137**: p. 290-297.
14. Zaki, T., *Catalytic dehydration of ethanol using transition metal oxide catalysts*. Journal of colloid and Interface Science, 2005. **284**(2): p. 606-613.
15. Phung, T.K., L.P. Hernández, and A. Lagazzo, *Dehydration of ethanol over zeolites, silica alumina and alumina: Lewis acidity, Brønsted acidity and confinement effects*. Applied Catalysis A: General, 2015. **493**: p. 77-89.
16. Rioux, R. and M. Vannice, *Hydrogenation/dehydrogenation reactions: isopropanol dehydrogenation over copper catalysts*. Journal of Catalysis, 2003. **216**(1-2): p. 362-376.
17. Chang, F.-W., W.-Y. Kuo, and K.-C. Lee, *Dehydrogenation of ethanol over copper catalysts on rice husk ash prepared by incipient wetness impregnation*. Applied Catalysis A: General, 2003. **246**(2): p. 253-264.
18. Issaadi, R., F. Garin, and C.-E. Chitour, *Study of the acid character of some palladium-modified pillared clay catalysts: Use of isopropanol decomposition as test reaction*. Catalysis today, 2006. **113**(3-4): p. 166-173.
19. Blasco, T. and J.L. Nieto, *Oxidative dehydrogenation of short chain alkanes on supported vanadium oxide catalysts*. Applied Catalysis A: General, 1997. **157**(1-2): p. 117-142.
20. Vohs, J. and M. Barteau, *Dehydration and dehydrogenation of ethanol and 1-propanol on the polar surfaces of zinc oxide*. Surface science, 1989. **221**(3): p. 590-608.

21. Matsumura, Y., K. Hashimoto, and S. Yoshida, *Selective dehydrogenation of ethanol over highly dehydrated silica*. Journal of Catalysis, 1989. **117**(1): p. 135-143.
22. Matsumura, Y., K. Hashimoto, and S. Yoshida, *Selective dehydrogenation of ethanol to acetaldehyde over silicalite-1*. Journal of Catalysis, 1990. **122**(2): p. 352-361.
23. Xin, H., et al., *Enhanced catalytic oxidation by hierarchically structured TS-1 zeolite*. The Journal of Physical Chemistry C, 2010. **114**(14): p. 6553-6559.
24. Xin, H., et al., *Catalytic dehydration of ethanol over post-treated ZSM-5 zeolites*. Journal of Catalysis, 2014. **312**: p. 204-215.
25. Li, C., et al., *Chiral catalysis in nanopores of mesoporous materials*. Chemical Communications, 2007(6): p. 547-558.
26. Kruk, M., et al., *Characterization of the porous structure of SBA-15*. Chemistry of materials, 2000. **12**(7): p. 1961-1968.
27. Xin, H., et al., *Organosilane surfactant-directed synthesis of mesoporous zeolites*. Energy and Environment Focus, 2013. **2**(1): p. 18-40.
28. Kresge, C., et al., *Ordered mesoporous molecular sieves synthesized by a liquid-crystal template mechanism*. nature, 1992. **359**(6397): p. 710.
29. Rahmat, N., A.Z. Abdullah, and A.R. Mohamed, *A review: mesoporous Santa Barbara amorphous-15, types, synthesis and its applications towards biorefinery production*. American Journal of Applied Sciences, 2010. **7**(12): p. 1579-1586.
30. Hongchuan, X. and Y. Qihua, *Progress in Research of Iron-Containing Mesoporous Silica*. Petrochemical Technology, 2006. **35**(11): p. 1017.
31. Lapisardi, G., et al., *Preparation, characterisation and catalytic activity of new bifunctional Ti-ALSBA15 materials. Application to a "one-pot" green synthesis of adipic acid from cyclohexene and organic hydroperoxides*. Microporous and mesoporous materials, 2005. **78**(2-3): p. 289-295.
32. Fang, Y., et al., *Ethylene Production from Ethanol Over Metal/Phosphorus-Modified ZSM-5 Catalysts*. Energy and Environment Focus, 2014. **3**(3): p. 227-235.

33. Liu, J., et al., *A novel and simple strategy for the direct synthesis bimetallic mesoporous materials Zr-La-SBA-15*. *Materials Letters*, 2014. **128**: p. 15-18.
34. Brinker, C.J. and G.W. Scherer, *Sol-gel science: the physics and chemistry of sol-gel processing*. 2013: Academic press.
35. Dawson, W.J., *Hydrothermal synthesis of advanced [electronic] ceramic powders*. *American Ceramic Society Bulletin*, 1988. **67**(10): p. 1673-8.
36. Deng, S. and Y. Lin, *Microwave synthesis of mesoporous and microporous alumina powders*. *Journal of materials science letters*, 1997. **16**(15): p. 1291-1294.
37. Deng, Y., et al., *Solvothermal preparation and characterization of nanocrystalline Bi₂Te₃ powder with different morphology*. *Journal of Physics and Chemistry of Solids*, 2002. **63**(11): p. 2119-2121.
38. Deng, Y., G.-D. Wei, and C.-W. Nan, *Ligand-assisted control growth of chainlike nanocrystals*. *Chemical physics letters*, 2003. **368**(5-6): p. 639-643.
39. Ozkan, U.S., T.A. Harris, and B.T. Schilf, *The partial oxidation of C5 hydrocarbons over vanadia-based catalysts*. *Catalysis today*, 1997. **33**(1-3): p. 57-71.
40. Bond, G.C. and S.F. Tahir, *Vanadium oxide monolayer catalysts Preparation, characterization and catalytic activity*. *Applied Catalysis*, 1991. **71**(1): p. 1-31.
41. Fornes, V., et al., *Catalytic performance of mesoporous VOx/SBA-15 catalysts for the partial oxidation of methane to formaldehyde*. *Applied Catalysis A: General*, 2003. **249**(2): p. 345-354.
42. Liu, Y.-M., et al., *Vanadium oxide supported on mesoporous SBA-15 as highly selective catalysts in the oxidative dehydrogenation of propane*. *Journal of Catalysis*, 2004. **224**(2): p. 417-428.
43. Orlov, A., Q.-Z. Zhai, and J. Klinowski, *Photocatalytic properties of the SBA-15 mesoporous silica molecular sieve modified with titanium*. *Journal of materials science*, 2006. **41**(8): p. 2187-2193.
44. Zhao, D., et al., *Morphological control of highly ordered mesoporous silica SBA-15*. *Chemistry of Materials*, 2000. **12**(2): p. 275-279.

45. Fan, D., D.-J. Dai, and H.-S. Wu, *Ethylene formation by catalytic dehydration of ethanol with industrial considerations*. *Materials*, 2012. **6**(1): p. 101-115.
46. Zhang, M. and Y. Yu, *Dehydration of ethanol to ethylene*. *Industrial & Engineering Chemistry Research*, 2013. **52**(28): p. 9505-9514.
47. Chen, Y., et al., *Dehydration reaction of bio-ethanol to ethylene over modified SAPO catalysts*. *Journal of Industrial and Engineering Chemistry*, 2010. **16**(5): p. 717-722.
48. Imhof, P. and J.C. van der Waal, *Catalytic process development for renewable materials*. 2013: John Wiley & Sons.
49. Takahara, I., et al., *Dehydration of ethanol into ethylene over solid acid catalysts*. *Catalysis Letters*, 2005. **105**(3-4): p. 249-252.
50. Madeira, F.F., et al., *Ethanol transformation over HFAU, HBEA and HMFI zeolites presenting similar Brønsted acidity*. *Applied Catalysis A: General*, 2009. **367**(1-2): p. 39-46.
51. Alharbi, W., et al., *Dehydration of ethanol over heteropoly acid catalysts in the gas phase*. *Journal of Catalysis*, 2014. **319**: p. 174-181.
52. Lanzafame, P., G. Centi, and S. Perathoner, *Catalysis for biomass and CO₂ use through solar energy: opening new scenarios for a sustainable and low-carbon chemical production*. *Chemical Society Reviews*, 2014. **43**(22): p. 7562-7580.
53. Yoneda, N., et al., *Recent advances in processes and catalysts for the production of acetic acid*. *Applied Catalysis A: General*, 2001. **221**(1-2): p. 253-265.
54. Christensen, C.H., et al., *Formation of Acetic Acid by Aqueous-Phase Oxidation of Ethanol with Air in the Presence of a Heterogeneous Gold Catalyst*. *Angewandte Chemie International Edition*, 2006. **45**(28): p. 4648-4651.
55. Jørgensen, B., et al., *Aerobic oxidation of aqueous ethanol using heterogeneous gold catalysts: Efficient routes to acetic acid and ethyl acetate*. *Journal of Catalysis*, 2007. **251**(2): p. 332-337.

56. Li, X. and E. Iglesia, *Selective Catalytic Oxidation of Ethanol to Acetic Acid on Dispersed Mo-V-Nb Mixed Oxides*. Chemistry-A European Journal, 2007. **13**(33): p. 9324-9330.
57. Zhou, H., et al., *Studies of oxidative dehydrogenation of ethanol over manganese oxide octahedral molecular sieve catalysts*. Microporous and Mesoporous Materials, 1998. **21**(4-6): p. 315-324.
58. Tesser, R., et al., *Kinetics of the Oxidative Dehydrogenation of Ethanol to Acetaldehyde on V₂O₅/TiO₂- SiO₂ Catalysts Prepared by Grafting*. Industrial & engineering chemistry research, 2004. **43**(7): p. 1623-1633.
59. Wan, Y. and D. Zhao, *On the controllable soft-templating approach to mesoporous silicates*. Chemical reviews, 2007. **107**(7): p. 2821-2860.
60. Han, Y. and D. Zhang, *Ordered mesoporous silica materials with complicated structures*. Current Opinion in Chemical Engineering, 2012. **1**(2): p. 129-137.
61. Fedeyko, J.M., D.G. Vlachos, and R.F. Lobo, *Understanding the differences between microporous and mesoporous synthesis through the phase behavior of silica*. Microporous and mesoporous materials, 2006. **90**(1-3): p. 102-111.
62. Morey, M., A. Davidson, and G. Stucky, *Silica-based, cubic mesostructures: synthesis, characterization and relevance for catalysis*. Journal of Porous Materials, 1998. **5**(3-4): p. 195-204.
63. Yanagisawa, T., et al., *The preparation of alkyltriethylammonium-kaneinite complexes and their conversion to microporous materials*. Bulletin of the Chemical Society of Japan, 1990. **63**(4): p. 988-992.
64. Santhanaraj, D., et al., *Structural and catalytic properties of V-SBA-15 for the vapor phase oxidation of diphenylmethane*. Reaction Kinetics, Mechanisms and Catalysis, 2011. **104**(2): p. 399-415.
65. Cui, X., et al., *Nonionic triblock copolymer synthesis of SBA-15 above the isoelectric point of silica (pH= 2-5)*. Materials Letters, 2005. **59**(18): p. 2257-2261.
66. Zhao, D., et al., *Triblock copolymer syntheses of mesoporous silica with periodic 50 to 300 angstrom pores*. science, 1998. **279**(5350): p. 548-552.

67. Schmidt-Winkel, P., et al., *Mesocellular siliceous foams with uniformly sized cells and windows*. Journal of the American Chemical Society, 1999. **121**(1): p. 254-255.
68. Brady, R., et al., *Hierarchical mesoporous silica materials for separation of functional food ingredients—A review*. Innovative food science & emerging technologies, 2008. **9**(2): p. 243-248.
69. Fonseca-Correa, R.A., et al., *Microporous and Mesoporous Materials in Decontamination of Water Process*, in *Microporous and Mesoporous Materials*. 2016, InTech.
70. Benreguia, N., A. Barnabé, and M. Trari, *Preparation and characterization of the semiconductor CuMnO_2 by sol-gel route*. Materials Science in Semiconductor Processing, 2016. **56**: p. 14-19.
71. Rogojan, R., et al., *Synthesis and characterization of alumina nano-powder obtained by sol-gel method*. UPB Buletin Stiintific, Series B: Chemistry and Materials Science, 2011. **73**(2): p. 67-76.
72. Meskin, P.E., et al., *Ultrasonically assisted hydrothermal synthesis of nanocrystalline ZrO_2 , TiO_2 , NiFe_2O_4 and NiO , 5ZnO , $5\text{Fe}_2\text{O}_4$ powders*. Ultrasonics sonochemistry, 2006. **13**(1): p. 47-53.
73. Xu, F. and L. Sun, *Solution-derived ZnO nanostructures for photoanodes of dye-sensitized solar cells*. Energy & Environmental Science, 2011. **4**(3): p. 818-841.
74. Guo, X., *Property degradation of tetragonal zirconia induced by low-temperature defect reaction with water molecules*. Chemistry of materials, 2004. **16**(21): p. 3988-3994.
75. Hannink, R.H., P.M. Kelly, and B.C. Muddle, *Transformation toughening in zirconia-containing ceramics*. Journal of the American Ceramic Society, 2000. **83**(3): p. 461-487.
76. Mercera, P., et al., *Zirconia as a support for catalysts Influence of additives on the thermal stability of the porous texture of monoclinic zirconia*. Applied catalysis, 1991. **71**(2): p. 363-391.

77. Mercera, P., et al., *Zirconia as a support for catalysts: Evolution of the texture and structure on calcination in air*. Applied catalysis, 1990. **57**(1): p. 127-148.
78. Haxel, G.B., et al., *Rare earth elements: critical resources for high technology*. 2002.
79. Krishnamurthy, N. and C.K. Gupta, *Extractive metallurgy of rare earths*. 2004: CRC press.
80. Weckhuysen, B.M. and D.E. Keller, *Chemistry, spectroscopy and the role of supported vanadium oxides in heterogeneous catalysis*. Catalysis Today, 2003. **78**(1): p. 25-46.
81. Bell, R. and A. Castleman, *Reactions of vanadium oxide cluster ions with 1, 3-butadiene and isomers of butene*. The Journal of Physical Chemistry A, 2002. **106**(42): p. 9893-9899.
82. Guan, Y., et al., *Controlling reaction pathways for alcohol dehydration and dehydrogenation over FeSBA-15 catalysts*. Catalysis Letters, 2007. **117**(1-2): p. 18-24.
83. Salas, P., et al., *Effect of the Si/Zr molar ratio on the synthesis of Zr-based mesoporous molecular sieves*. Materials Chemistry and Physics, 2009. **114**(1): p. 139-144.
84. Sheng, X., et al., *Effect of different lanthanum source and preparation method on the lanthanum-doped mesoporous SBA-15 synthesis*. Journal of Porous Materials, 2011. **18**(6): p. 677-683.
85. Zhan, N., et al., *Lanthanum-phosphorous modified HZSM-5 catalysts in dehydration of ethanol to ethylene: A comparative analysis*. Catalysis Communications, 2010. **11**(7): p. 633-637.
86. Nguyen, T., et al., *Synthesis, characterization and study of lanthanum phosphates as light alcohols dehydration catalysts*. Applied Catalysis B: Environmental, 2015. **166**: p. 432-444.
87. Wannaborworn, M., P. Prasertdam, and B. Jongsomjit, *A comparative study of solvothermal and sol-gel-derived nanocrystalline alumina catalysts for ethanol dehydration*. Journal of Nanomaterials, 2015. **16**(1): p. 429.

88. Cecilia, J., et al., *V and V-P containing Zr-SBA-15 catalysts for dehydration of glycerol to acrolein*. *Catalysis Today*, 2015. **254**: p. 43-52.
89. Cecilia, J., et al., *WO₃ supported on Zr doped mesoporous SBA-15 silica for glycerol dehydration to acrolein*. *Applied Catalysis A: General*, 2016. **516**: p. 30-40.
90. Ginjupalli, S.R., et al., *Vapour phase dehydration of glycerol to acrolein over tungstated zirconia catalysts*. *Applied Surface Science*, 2014. **309**: p. 153-159.
91. Chai, S.-H., et al., *Sustainable production of acrolein: effects of reaction variables, modifiers doping and ZrO₂ origin on the performance of WO₃/ZrO₂ catalyst for the gas-phase dehydration of glycerol*. *RSC Advances*, 2014. **4**(9): p. 4619-4630.
92. Massa, M., A. Andersson, and E. Finocchio, *Gas-phase dehydration of glycerol to acrolein over Al₂O₃, SiO₂, and TiO₂-supported Nb-and W-oxide catalysts*. *Journal of catalysis*, 2013. **307**: p. 170-184.
93. Omata, K., et al., *Hydrothermal synthesis of W-Nb complex metal oxides and their application to catalytic dehydration of glycerol to acrolein*. *Catalysis today*, 2013. **201**: p. 7-11.
94. Wang, H., et al., *Dehydrogenation and oxidative coupling of alcohol and amines catalyzed by organosilicon-supported TiO₂@ PMHSIPN*. *RSC Advances*, 2014. **4**(65): p. 34681-34686.
95. Yang, Z., et al., *Gas-phase oxidation of alcohols over silver: The extension of catalytic cycles of oxidation of alcohols in liquid-phase*. *Journal of Molecular Catalysis A: Chemical*, 2005. **241**(1-2): p. 15-22.
96. Forzatti, P., E. Tronconi, and A.S. Elmi, *Methanol oxidation over vanadia-based catalysts*. *Applied Catalysis A: General*, 1997. **157**(1-2): p. 387-408.
97. Khodakov, A., et al., *Structure and catalytic properties of supported vanadium oxides: support effects on oxidative dehydrogenation reactions*. *Journal of Catalysis*, 1999. **181**(2): p. 205-216.
98. Santacesaria, E., et al., *Oxidative dehydrogenation of ethanol to acetaldehyde on V₂O₅/TiO₂-SiO₂ catalysts obtained by grafting vanadium and*

- titanium alkoxides on silica*. Journal of Molecular Catalysis A: Chemical, 2003. **204**: p. 617-627.
99. Guan, Y. and E.J. Hensen, *Ethanol dehydrogenation by gold catalysts: The effect of the gold particle size and the presence of oxygen*. Applied Catalysis A: General, 2009. **361**(1-2): p. 49-56.
100. Nakamura, Y., T. Murayama, and W. Ueda, *Hydrogen-transfer dehydration between alcohols over V_2O_3 and MoO_2 catalysts for the formation of corresponding alkanes and aldehydes*. Journal of Molecular Catalysis A: Chemical, 2014. **394**: p. 137-144.
101. Dutov, V.V., et al., *Silica-supported silver-containing OMS-2 catalysts for ethanol oxidative dehydrogenation*. Catalysis Today, 2016. **278**: p. 164-173.
102. Barrett, E.P., L.G. Joyner, and P.P. Halenda, *The determination of pore volume and area distributions in porous substances. I. Computations from nitrogen isotherms*. Journal of the American Chemical society, 1951. **73**(1): p. 373-380.
103. Maroto-Valer, M.M., C. Song, and Y. Soong, *Environmental challenges and greenhouse gas control for fossil fuel utilization in the 21st century*. 2012: Springer Science & Business Media.
104. Chamack, M., A. Mahjoub, and H. Aghayan, *Catalytic performance of vanadium-substituted molybdophosphoric acid supported on zirconium modified mesoporous silica in oxidative desulfurization*. Chemical Engineering Research and Design, 2015. **94**: p. 565-572.
105. Tang, Y., et al., *Zirconia functionalized SBA-15 as effective adsorbent for phosphate removal*. Microporous and Mesoporous Materials, 2012. **155**: p. 192-200.
106. Chytil, S., W.R. Glomm, and E.A. Blekkan, *Characterization of Pt/SBA-15 prepared by the deposition-precipitation method*. Catalysis Today, 2009. **147**(3): p. 217-223.
107. Bae, Y.K. and O.H. Han, *Removal of copolymer template from SBA-15 studied by 1H MAS NMR*. Microporous and Mesoporous Materials, 2007. **106**(1): p. 304-307.

108. Thielemann, J.P., et al., *Pore structure and surface area of silica SBA-15: influence of washing and scale-up*. Beilstein journal of nanotechnology, 2011. **2**: p. 110.
109. Chandrasekar, G., et al., *Synthesis of hexagonal and cubic mesoporous silica using power plant bottom ash*. Microporous and Mesoporous Materials, 2008. **111**(1): p. 455-462.
110. Halina, M., et al., *Non-hydrothermal synthesis of mesoporous materials using sodium silicate from coal fly ash*. Materials chemistry and physics, 2007. **101**(2): p. 344-351.
111. Wu, B., Z. Tong, and X. Yuan, *Synthesis, characterization and catalytic application of mesoporous molecular sieves SBA-15 functionalized with phosphoric acid*. Journal of Porous Materials, 2012. **19**(5): p. 641-647.
112. Ryoo, R., et al., *Disordered molecular sieve with branched mesoporous channel network*. The Journal of Physical Chemistry, 1996. **100**(45): p. 17718-17721.
113. Pang, X. and F. Tang, *Morphological control of mesoporous materials using inexpensive silica sources*. Microporous and mesoporous materials, 2005. **85**(1): p. 1-6.
114. Chanchuey, T., C. Autthanit, and B. Jongsomjit, *Effect of Mo-doped mesoporous Al-SSP catalysts for the catalytic dehydration of ethanol to ethylene*. Journal of Chemistry, 2016. **2016**.
115. Bendou, S. and M. Amrani, *Effect of hydrochloric acid on the structural of sodic-bentonite clay*. Journal of Minerals and Materials Characterization and Engineering, 2014. **2**(05): p. 404.
116. Xin, H., Y. Fang, and X. Li, *Green synthesis of mesoporous Fe-SBA-15 with well-isolated iron sites*. Energy and Environment Focus, 2014. **3**(3): p. 282-286.
117. Sanjini, N. and S. Velmathi, *Iron impregnated SBA-15, a mild and efficient catalyst for the catalytic hydride transfer reduction of aromatic nitro compounds*. Rsc Advances, 2014. **4**(30): p. 15381-15388.
118. Sing, K.S., *Reporting physisorption data for gas/solid systems with special reference to the determination of surface area and porosity*

- (*Recommendations 1984*). Pure and applied chemistry, 1985. **57**(4): p. 603-619.
119. Laha, S., et al., *Cerium containing MCM-41-type mesoporous materials and their acidic and redox catalytic properties*. Journal of Catalysis, 2002. **207**(2): p. 213-223.
120. Kishor, R. and A.K. Ghoshal, *N 1-(3-Trimethoxysilylpropyl) diethylenetriamine grafted KIT-6 for CO 2/N 2 selective separation*. RSC Advances, 2016. **6**(2): p. 898-909.
121. Rahmani, A., M. Benoit, and C. Benoit, *Signature of small rings in the Raman spectra of normal and compressed amorphous silica: A combined classical and ab initio study*. Physical Review B, 2003. **68**(18): p. 184202.
122. Morrow, B. and A. McFarlan, *Chemical reactions at silica surfaces*. Journal of non-crystalline solids, 1990. **120**(1-3): p. 61-71.
123. Gao, X., J. Fierro, and I.E. Wachs, *Structural characteristics and catalytic properties of highly dispersed ZrO₂/SiO₂ and V₂O₅/ZrO₂/SiO₂ catalysts*. Langmuir, 1999. **15**(9): p. 3169-3178.
124. Zhang, M., et al., *Annealing of-decay damage in zircon: a Raman spectroscopic study*. Journal of Physics: Condensed Matter, 2000. **12**(13): p. 3131.
125. Li, H., et al., *Ni/SBA-15 catalysts for CO methanation: effects of V, Ce, and Zr promoters*. RSC Advances, 2015. **5**(117): p. 96504-96517.
126. Klimova, T., et al., *Advantages of ZrO₂-and TiO₂-SBA-15 mesostructured supports for hydrodesulfurization catalysts over pure TiO₂, ZrO₂ and SBA-15*. Microporous and Mesoporous Materials, 2010. **133**(1-3): p. 91-99.
127. Wu, S., et al., *Synthesis of heteroatom substituted SBA-15 by the "pH-adjusting" method*. Chemistry of materials, 2004. **16**(3): p. 486-492.
128. Chen, S.-Y., et al., *Direct preparation of thermally stable Sn-incorporated SBA-15 mesoporous materials in the self-generated acidic environment*. The Journal of Physical Chemistry C, 2009. **113**(34): p. 15226-15238.

129. Kosuge, K., et al., *Morphological control of rod-and fiberlike SBA-15 type mesoporous silica using water-soluble sodium silicate*. Chemistry of Materials, 2004. **16**(5): p. 899-905.
130. Pang, X. and F. Tang, *Morphological control of mesoporous materials using inexpensive silica sources*. Microporous and mesoporous materials, 2005. **85**(1-2): p. 1-6.
131. Wang, J., et al., *Hydrothermal synthesis of SBA-15 using sodium silicate derived from coal gangue*. Journal of Nanomaterials, 2013. **2013**: p. 6.
132. El Kady, F., S. Shaban, and A.A. El Naga, *Catalytic dehydrogenation of cyclohexene over MoO₃/Y-Al₂O₃ catalysts*. Transition Metal Chemistry, 2011. **36**(2): p. 237-244.
133. Li, Y., B. Yan, and H. Yang, *Construction, characterization, and photoluminescence of mesoporous hybrids containing europium (III) complexes covalently bonded to SBA-15 directly functionalized by modified β -diketone*. The Journal of Physical Chemistry C, 2008. **112**(10): p. 3959-3968.
134. Trujillo, J.E., *Negative Thermal Expansion and Ferroelectric Oxides in Electronic Device Composites*. 2017, University of California, Los Angeles.
135. Handzlik, J., et al., *Properties and metathesis activity of molybdena-alumina, molybdena-silica-alumina and molybdena-silica catalysts-a comparative study*. Applied Catalysis A: General, 2006. **312**: p. 213-219.
136. Zhang, X., et al., *Comparison of four catalysts in the catalytic dehydration of ethanol to ethylene*. Microporous and Mesoporous Materials, 2008. **116**(1-3): p. 210-215.
137. Hidalgo, J., et al., *(V)/Hydrotalcite, (V)/Al₂O₃, (V)/TiO₂ and (V)/SBA-15 catalysts for the partial oxidation of ethanol to acetaldehyde*. Journal of Molecular Catalysis A: Chemical, 2016. **420**: p. 178-189.
138. Čičmanec, P., et al., *Conversion of ethanol to acetaldehyde over VOX-SiO₂ catalysts: the effects of support texture and vanadium speciation*. Reaction Kinetics, Mechanisms and Catalysis, 2017. **121**(1): p. 353-369.

139. Newalkar, B.L., J. Olanrewaju, and S. Komarneni, *Microwave-hydrothermal synthesis and characterization of zirconium substituted SBA-15 mesoporous silica*. The Journal of Physical Chemistry B, 2001. **105**(35): p. 8356-8360.
140. Gao, F., et al., *The states of vanadium species in V-SBA-15 synthesized under different pH values*. Microporous and Mesoporous Materials, 2008. **110**(2): p. 508-516.
141. Piumetti, M., et al., *Effect of vanadium dispersion and of support properties on the catalytic activity of V-containing silicas*. Catalysis today, 2012. **179**(1): p. 140-148.
142. Nagaraju, P., et al., *Preparation, characterization and catalytic properties of promoted vanadium phosphate catalysts*. Catalysis Communications, 2008. **9**(14): p. 2449-2454.
143. Van Der Voort, P., et al., *The effect of water on the structure of supported vanadium oxide structures. An FT-RAMAN, in situ DRIFT and in situ UV-VIS diffuse reflectance study*. Spectrochimica Acta Part A: Molecular and Biomolecular Spectroscopy, 1997. **53**(12): p. 2181-2187.
144. Piumetti, M., et al., *Effect of vanadium dispersion and support properties on the catalytic activity of V-SBA-15 and V-MCF mesoporous materials prepared by direct synthesis*. Catalysis today, 2011. **176**(1): p. 458-464.
145. Van der Houwen, J.A., et al., *The effect of organic ligands on the crystallinity of calcium phosphate*. Journal of Crystal Growth, 2003. **249**(3): p. 572-583.
146. Weckhuysen, B.M., J.-M. Jehng, and I.E. Wachs, *In Situ Raman Spectroscopy of Supported Transition Metal Oxide Catalysts: $^{18}\text{O}_2$ - $^{16}\text{O}_2$ Isotopic Labeling Studies*. The Journal of Physical Chemistry B, 2000. **104**(31): p. 7382-7387.
147. Busca, G., *Differentiation of mono-oxo and polyoxo and of monomeric and polymeric vanadate, molybdate and tungstate species in metal oxide catalysts by IR and Raman spectroscopy*. Journal of Raman Spectroscopy, 2002. **33**(5): p. 348-358.
148. Piumetti, M., et al., *Vanadium-containing SBA-15 systems prepared by direct synthesis: physico-chemical and catalytic properties in the decomposition of*

- dichloromethane*. *Microporous and Mesoporous Materials*, 2010. **133**(1): p. 36-44.
149. Nashim, A., S. Martha, and K. Parida, *Heterojunction conception of n-La₂Ti₂O₇/p-CuO in the limelight of photocatalytic formation of hydrogen under visible light*. *RSC Advances*, 2014. **4**(28): p. 14633-14643.
150. Zhao, W., et al., *Systematic effects of S-doping on the activity of V₂O₅/TiO₂ catalyst for low-temperature NH₃-SCR*. *Chemical Engineering Journal*, 2013. **228**: p. 815-823.
151. Enger, B.C., R. Lødeng, and A. Holmen, *A review of catalytic partial oxidation of methane to synthesis gas with emphasis on reaction mechanisms over transition metal catalysts*. *Applied Catalysis A: General*, 2008. **346**(1): p. 1-27.
152. Zhang, W., et al., *Interplay between zirconium addition and morphology/catalytic performance of HPW/PEHA/SBA-15 composites towards selective oxidation of benzyl alcohol*. *Journal of Porous Materials*, 2015. **22**(4): p. 997-1008.
153. Ding, M., et al., *XPS studies on the electronic structure of bonding between solid and solutes: adsorption of arsenate, chromate, phosphate, Pb²⁺, and Zn²⁺ ions on amorphous black ferric oxyhydroxide*. *Geochimica et Cosmochimica Acta*, 2000. **64**(7): p. 1209-1219.
154. Jalabert, D., I. Vickridge, and A. Chabli, *Swift Ion Beam Analysis in Nanosciences*. 2017: John Wiley & Sons.
155. Popa, A., et al., *AFM and SEM-EDS examination of highly dispersed heteropolyacids supported on MCM 41 and SBA 15 mesoporous materials*. *Journal of Optoelectronics and Advanced Materials*, 2009. **11**(8): p. 1185.
156. Prutton, M. and M.M. El Gomati, *Scanning Auger electron microscopy*. 2006: John Wiley & Sons.
157. Wenk, H.-R. and A. Bulakh, *Minerals: their constitution and origin*. 2016: Cambridge University Press.
158. Zhang, J., et al., *Facile synthesis of well-dispersed CeO₂-CuO x composite hollow spheres with superior catalytic activity for CO oxidation*. *RSC Advances*, 2015. **5**(115): p. 95133-95139.

159. Shi, R., et al., *MgO-supported Cu nanoparticles for efficient transfer dehydrogenation of primary aliphatic alcohols*. *Catalysis Communications*, 2009. **11**(4): p. 306-309.
160. Di Cosimo, J., et al., *Structure and surface and catalytic properties of Mg-Al basic oxides*. *Journal of Catalysis*, 1998. **178**(2): p. 499-510.
161. Zhang, L., Y. Zhang, and S. Chen, *Effect of promoter SiO₂, TiO₂ or SiO₂-TiO₂ on the performance of CuO-ZnO-Al₂O₃ catalyst for methanol synthesis from CO₂ hydrogenation*. *Applied Catalysis A: General*, 2012. **415**: p. 118-123.
162. Ren, H., et al., *Methanol synthesis from CO₂ hydrogenation over Cu/V-Al₂O₃ catalysts modified by ZnO, ZrO₂ and MgO*. *Journal of Industrial and Engineering Chemistry*, 2015. **28**: p. 261-267.
163. Sujeerakulkai, S. and S. Jitkarnka, *Bio-based hydrocarbons and oxygenates from catalytic bio-ethanol dehydration: comparison between gallium and germanium oxides as promoters on HBeta zeolites with various silica to alumina ratios*. *Journal of Cleaner Production*, 2016. **111**: p. 51-61.
164. Mamontov, G., et al., *Ethanol dehydrogenation over Ag-CeO₂/SiO₂ catalyst: Role of Ag-CeO₂ interface*. *Applied Catalysis A: General*, 2016. **528**: p. 161-167.
165. Yao, S., et al., *A kinetic study of methanol oxidation over SiO₂*. *Applied Catalysis A: General*, 2000. **198**(1): p. 43-50.
166. Vining, W.C., *Understanding the effect of modifying elements in supported vanadia bilayered catalysts for methanol oxidation to formaldehyde*. 2011: University of California, Berkeley.
167. Zhang, H., et al., *Effective silica supported Sb-V mixed oxide catalyst for selective oxidation of methanol to formaldehyde*. *Journal of Catalysis*, 2008. **260**(2): p. 295-304.
168. Nalwa, H.S., *Handbook of Surfaces and Interfaces of Materials: Surface and interface phenomena*. Vol. 1. 2001: Academic Press.
169. Rahmanian, A. and H. Ghaziaskar, *Continuous dehydration of ethanol to diethyl ether over aluminum phosphate-hydroxyapatite catalyst under sub and supercritical condition*. *The Journal of Supercritical Fluids*, 2013. **78**: p. 34-41.

170. Guisnet, M. and P. Magnoux, *Organic chemistry of coke formation*. Applied Catalysis A: General, 2001. **212**(1): p. 83-96.
171. Fung, S., *Regenerating a reforming catalyst*. CHEMTECH;(United States), 1994. **24**(1).
172. Baidya, T. and R.J. Cattolica, *Fe and CaO promoted Ni catalyst on gasifier bed material for tar removal from producer gas*. Applied Catalysis A: General, 2015. **503**: p. 43-50.





APPENDIX

จุฬาลงกรณ์มหาวิทยาลัย
CHULALONGKORN UNIVERSITY

APPANDIX A

CALCULATION FOR CATALYST PREPARATION

Calculation of vanadium loading

The vanadium oxide were deposited onto all different SBA-15, Zr/SBA-15 and Zr-La/SBA-15 supports by the incipient wetness impregnation method by adding vanadyl acetylacetonate (NH_4VO_3) ethanolic solutions (nominal vanadium content of 2 wt%). The preparation catalyst was calculated based on 1g of catalyst used.

V/SBA-15 was prepared as follow:

Reagent : - Vanadyl acetylacetonate (NH_4VO_3)
 Molecular weight = 265.16 g/mol
 Vanadium (V), atomic weight = 50.9415 g/mol
 - Support: SBA/15

Based on 1g of catalyst used, the V/SBA-15 catalyst contain 2wt.% of Vanadium (V).

So the catalyst composition would be as follow:

Vanadium	=	0.02	g.
SBA-15	=	1.00 – 0.02	g.
	=	0.98	g.

Vanadyl acetylacetonate is consisted of 1 V atom, so weigh of V in Vanadyl acetylacetonate is 50.9415 g

50.9415 g of V in Vanadyl acetylacetonate 265.16 g

0.02 g of V in Vanadyl acetylacetonate $265.16 \times 0.02/50.9415$ g

= 0.1041 g



APPANDIX B

The amount of each element near the surface of different VOx/SBA-15 catalysts can be determined quantitatively. The results are summarized in **Table B.1** (EDX by SEM) and **Table B.2** (EDX by TEM).

Table B.1 The amount of each element near the surface of different VOx/SBA-15 catalysts granule obtained from EDX by SEM.

Catalysts	Amount of weight on surface (wt %)				
	Si	O	Zr	La	V
V/SBA-15-SG	57.5	40.8	0	0	1.7
V-Zr/SBA-15-SG	45.6	32.6	19.9	0	1.9
V-Zr-La/SBA-15-SG	40.9	36.6	18.7	1.6	2.2
V/SBA-15-HT	61.5	36.6	0	0	1.9
V-Zr/SBA-15-HT	16.2	32.2	49.1	0	2.5
V-Zr-La/SBA-15-HT	16.9	21.1	53.1	6.0	2.9

Table B.2 The amount of each element near the surface of different VOx/SBA-15 catalysts granule obtained from EDX by TEM.

Catalysts	Amount of weight on surface (wt %)						
	Si	O	Zr	La	V	C	Cu
V/SBA-15-SG	39.4	42.8	0	0	0.2	9.2	8.4
V-Zr/SBA-15-SG	45.8	23.6	8.5	0	2.0	3.6	16.7
V-Zr-La/SBA-15-SG	38.4	37.2	7.9	1.7	1.3	7.5	6.0
V/SBA-15-HT	39.8	30.5	0	0	0.7	20.5	8.5
V-Zr/SBA-15-HT	18.6	17.8	29.7	0	1.1	23.5	9.3
V-Zr-La/SBA-15-HT	12.5	26.0	33.5	3.3	3.9	11.0	9.8

Condition; (C and Cu are associated with the grid and the dispersion medium, respectively)

APPENDIX C

CALIBRATION CURVES

To ensure the analysis of products, prior to the measurement, the calibration of GC was performed by calibrating the GC-FID and GC-TCD with certified pure gas of ethanol, ethylene, diethyl ether, acetaldehyde, carbon monoxide (CO) and carbon dioxide (CO₂) of the desired concentrations using an internal standard technique. Duplicate injections of each standard were made and the average value was used for the calibration graph of each reactant and product. Then, the ethanol conversion and the selectivity of ethylene, diethyl ether, acetaldehyde, carbon monoxide (CO) and carbon dioxide (CO₂) were calculated.

The retention time of the each component in the chromatogram that showed in **Table C.1.**

Table C.1. The retention time of the each component in the chromatogram.

Reactant/Products	Retention time (min)
Ethanol	4.6
Ethylene	4.1
Diethyl ether	4.9
Acetaldehyde	4.4
CO	2.0 (TCD)
CO ₂	4.8 (TCD)

The calibration curves of the main reagent including ethanol, diethyl ether, ethylene and acetaldehyde are illustrated in **Figure C.1-C.6** as follows;

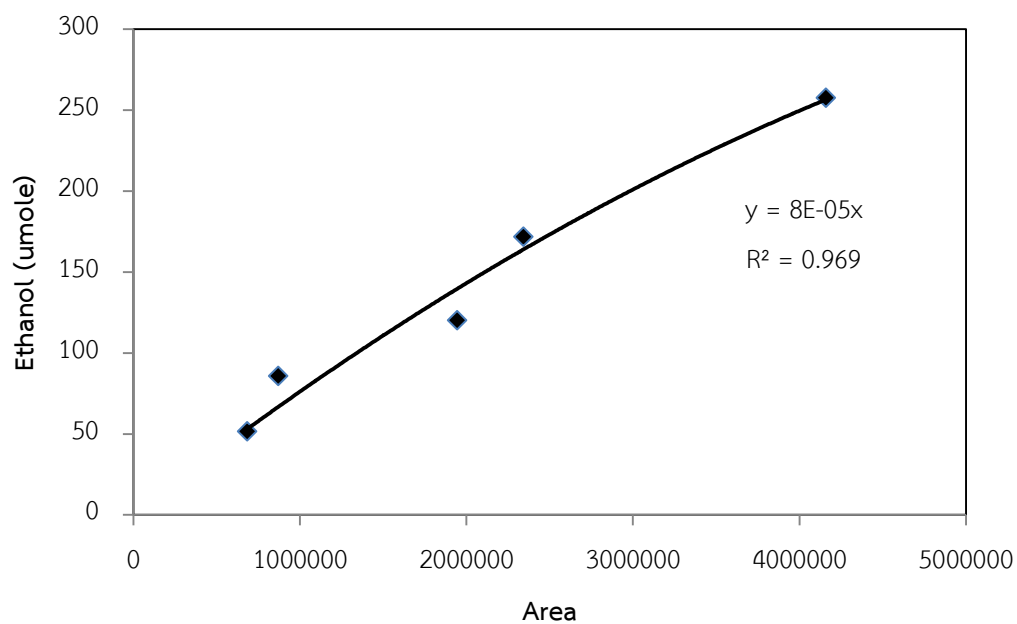


Figure C.1 The calibration curve of ethanol

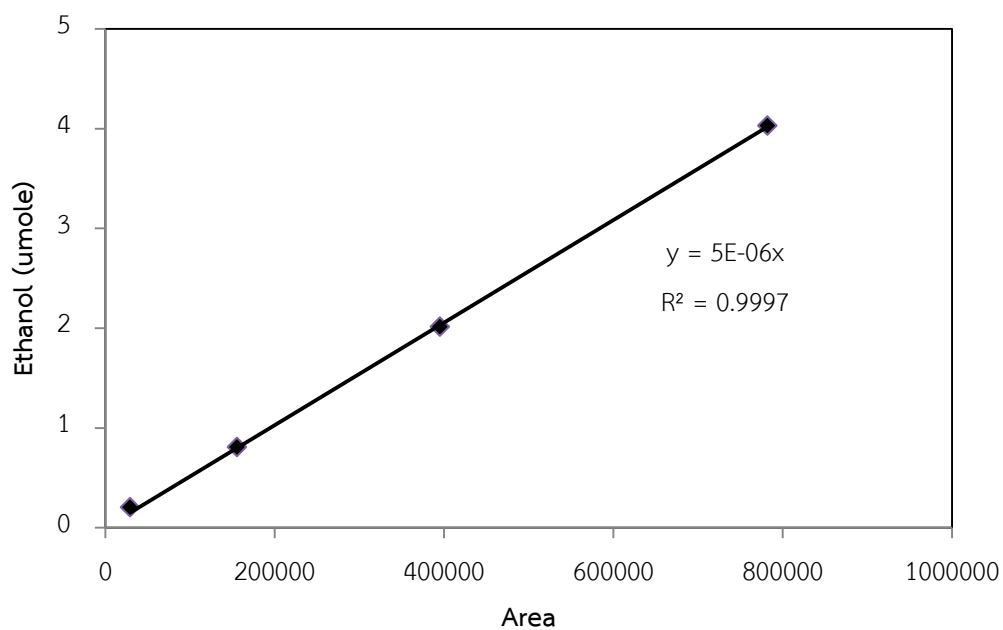


Figure C.2 The calibration curve of ethylene

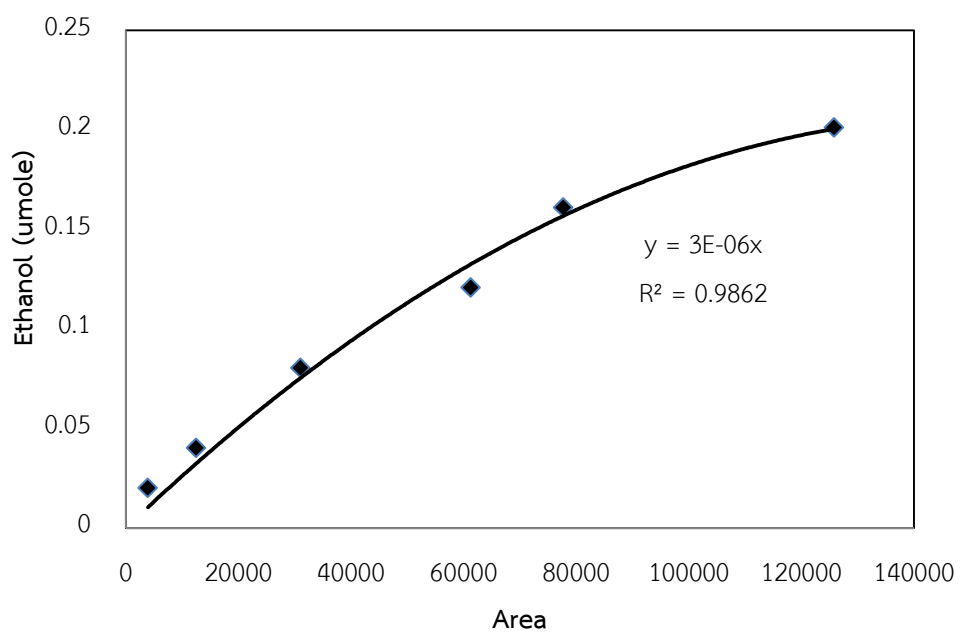


Figure C.3 The calibration curve of diethyl ether

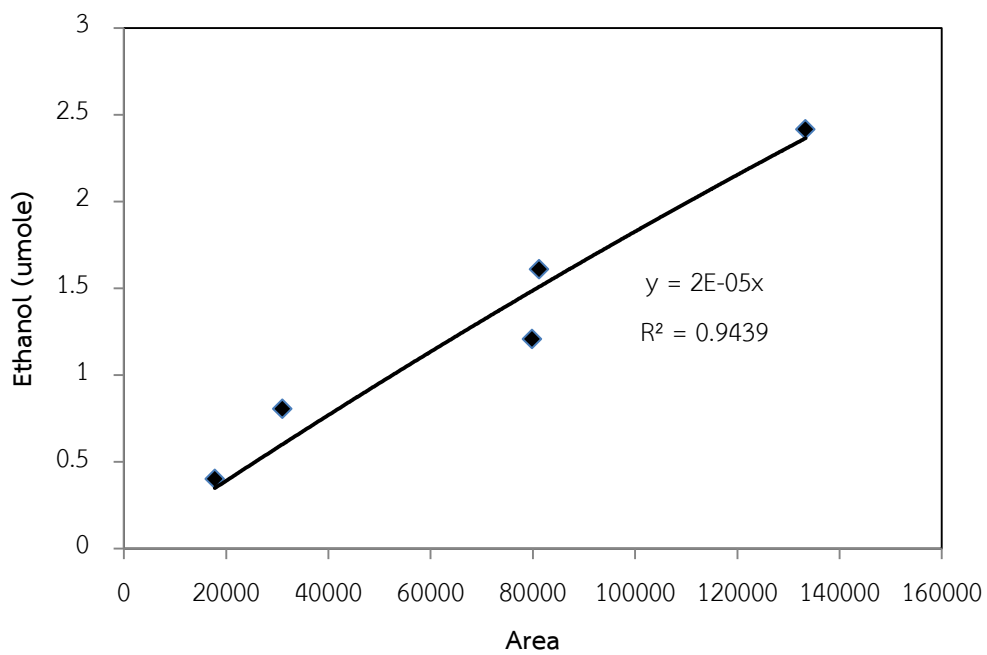


Figure C.4 The calibration curve of acetaldehyde

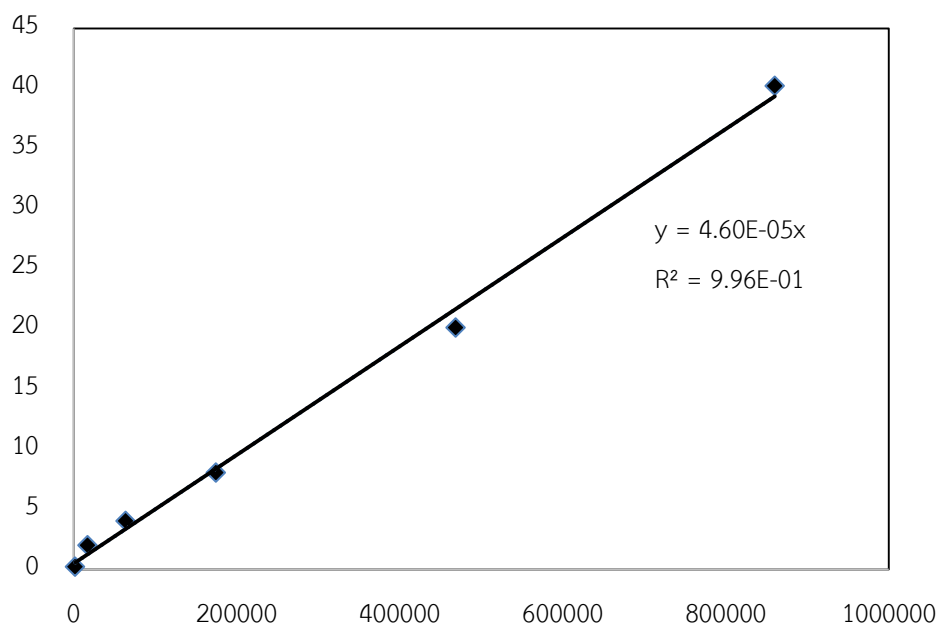


Figure C.5 The calibration curve of carbon monoxide (CO)

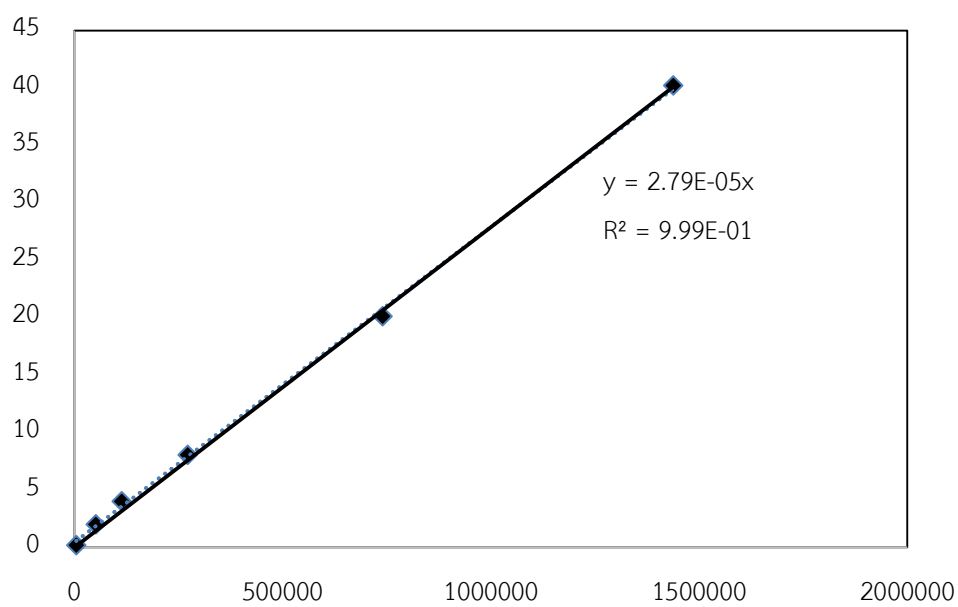


Figure C.6 The calibration curve of carbon dioxide (CO₂)

APPENDIX D

CALCULATION OF REACTANT CONVERSION, PRODUCT SELECTIVITY

AND PRODUCT YIELD

The conversion of reactant and selectivity of products exhibited the performance of catalyst. Then, there were used demonstrated the catalytic activity for dehydration, non-oxidative dehydrogenation and oxidative dehydrogenation of ethanol.

Ethanol conversion (Reactant)

The conversion of ethanol is defined as mole of ethanol converted with respect to ethanol in feed;

$$\text{Ethanol conversion (\%)} = \frac{[\text{mole of ethanol in feed} - \text{mole of ethanol in product}]}{\text{mole of ethanol in feed}} \times 100$$

Product selectivity

The selectivity towards each product is defined as moles of product formed with respect to total moles of products;

$$\text{Product selectivity (\%)} = \frac{\text{Moles of each product}}{\text{Total moles of product}} \times 100$$

Product yield

$$\text{Product yield (\%)} = \text{Reactant conversion} \times \text{Selectivity of each product}$$

APPANDIX E
LIST OF PUBLICATIONS

1. Chaowat Autthanit and Bunjerd Jongsomjit, Differences in characteristics of Zr/SBA-15 and bimetallic Zr-La/SBA-15 prepared by sol-gel and hydrothermal methods, Journal of Porous Materials, 24 (2017) 1383-1394.

(Impact factor = 1.624, Q2 by JCR (ISI) and SJR)

2. Chaowat Autthanit and Bunjerd Jongsomjit, Production of Ethylene through Ethanol Dehydration on SBA-15 Catalysts Synthesized by Sol-gel and One-step Hydrothermal Methods, Journal of Oleo Science, 67 (2018) 235-243.

(Impact factor = 1.076, Q3 by JCR (ISI) and Q2 by SJR)

3. Chaowat Autthanit, Piyasan Praserttham and Bunjerd Jongsomjit, Oxidative and non-oxidative dehydrogenation of ethanol to acetaldehyde over different VO_x/SBA-15 catalysts.

(Submitted to Renewable Energy)

(Impact factor = 4.357, Q1 by JCR (ISI) and Q1 by SJR)

VITA

Chaowat Autthanit was born on September 23, 1988 in Bangkok, Thailand. In 2010, he completed the Bachelor's Degree of Industrial Chemistry from the Department of Chemistry, Faculty of Science, King Mongkut's Institute of Technology Ladkrabang. He has further studied in Master's degree of Chemical Technology from the Department of Chemical Technology, Faculty of Science, Chulalongkorn University in 2011. Thereafter, he continued studying Doctoral Degree of Chemical Engineering at Chulalongkorn University and joined center of excellence on catalysis and catalytic reaction engineering research group under the supervision of Prof. Dr. Bunjerd Jongsomjit since August 2014.

